Natural Resources Canada | Ressources naturelles Canada

GEOLOGICAL SURVEY OF CANADA
OPEN FILE 8620

Targeted Geoscience Initiative 5 Grant Program interim reports 2018–2019

D. Benn, J.M. Brenan, K. Fuller, C. Grondahl, D. Layton-Matthews, M.I. Leybourne, R. Linnen, T. Martins, D. Milidragovic, D.P. Moynihan, J.E. Mungall, G.T. Nixon, C.D.W. Padget, D.R.M. Pattison, K.U. Rempel, E.J. Scanlan, J.S. Scoates, A. Tsay, A. Voinot, N.A. Van Wagoner, R. Weston, A.E. Williams-Jones, K. Woods, and Z. Zajacz

2019

Canada

GEOLOGICAL SURVEY OF CANADA
OPEN FILE 8620

Targeted Geoscience Initiative 5
Grant Program interim reports 2018–2019

D. Benn[1], J.M. Brenan[2], K. Fuller[3], C.Grondahl[4], D. Layton-Matthews[5], M.I. Leybourne[5], R. Linnen[1], T. Martins[6], D. Milidragovic[7], D.P. Moynihan[8], J.E. Mungall[9], G.T. Nixon[7], C.D.W. Padget[10], D.R.M. Pattison[10], K.U. Rempel[3], E.J. Scanlan[5], J.S. Scoates[11], A. Tsay[4], A. Voinot[5], N.A. Van Wagoner[12], R. Weston[13], A.E. Williams-Jones[3], K. Woods[2], and Z. Zajacz[4]

[1]Department of Earth Sciences, Western University, 1151 Richmond Street N., London, Ontario N6A 5B7
[2]Department of Earth Sciences, Dalhousie University, 1355 Oxford Street, Life Sciences Centre, Halifax, Nova Scotia B3H 4R2
[3]Department of Earth and Planetary Sciences, McGill University, 3450 University Street, Montréal, Quebec H3A 0E8
[4]Department of Earth Sciences, University of Toronto, 22 Russell Street, Toronto, Ontario M5S 3B1
[5]Department of Geological Sciences and Geological Engineering, Queen's University, 32 Union Street, Kingston, Ontario K7L 3N6
[6]Manitoba Geological Survey, 1395 Ellice Avenue, Winnipeg, Manitoba R3G 3P2
[7]British Columbia Geological Survey, 1810 Blanshard Street, Victoria, British Columbia V8W 9N3
[8]Yukon Geological Survey, 91807 Alaska Hwy, Whitehorse, Yukon Y1A 0R3
[9]Department of Earth Sciences, Carleton University, 1125 Colonel By Drive, Ottawa, Ontario K1S 5B6
[10]Department of Earth Sciences, University of Calgary, 2500 University Drive NW, Calgary, Alberta T2N 1N4
[11]Pacific Centre for Isotopic and Geochemical Research (PCIGR), Department of Earth, Ocean and Atmospheric Sciences, 2020 – 2207 Main Mall, University of British Columbia, Vancouver, British Columbia V6T 1Z4
[12]Department of Physical Sciences, Thompson Rivers University, 900 McGill Road, Kamloops, British Columbia V2C 0C8
[13]Noront Resources, 886A Alloy Place, Thunder Bay, Ontario P7B 6E6

2019

Permanent link: https://doi.org/10.4095/314997

This publication is available for free download through GEOSCAN (https://geoscan.nrcan.gc.ca/).

Recommended citation

Benn, D., Brenan, J.M., Fuller, K., Grondahl, C., Layton-Matthews, D., Leybourne, M.I., Linnen, R., Martins, T., Milidragovic, D., Moynihan, D.P., Mungall, J.E., Nixon, G.T., Padget, C.D.W., Pattison, D.R.M., Rempel, K.U., Scanlan, E.J., Scoates, J.S., Tsay, A., Voinot, A., Van Wagoner, N.A., Weston, R., Williams-Jones, A.E., Woods, K., and Zajacz, Z., 2019. Targeted Geoscience Initiative 5 Grant Program interim reports 2018–2019; Geological Survey of Canada, Open File 8620, 82 p. https://doi.org/10.4095/314997

Publications in this series have not been edited; they are released as submitted by the author.

CONTENTS

Figures

Table

Figures

Origin of Chromitites in the Ring of Fire Part II: Trace element fi ngerprinting of contaminants

J.M. Brenan[1], K. Woods[1], J.E. Mungall[2], R. Weston[3]

Abstract: To expand on the existing database documenting the trace element composition of ROFIS chromites, and to constrain models of their origin, a total of 45 chromite-bearing samples from the Black Thor, Big Daddy, Blackbird, Black Label chromite deposits have been analysed for major and trace elements. The samples represent three textural groups, as defined by the relative abundance of cumulate silicate phases and chromite. A search of the element partitioning literature has shown that of the elements that are readily detectable in the chromites, Ga, Zn and V show contrasting behaviour in their olivine- and chromite-melt partitioning. Specifically, these elements are ambivalent (D ~ 1, Zn) to moderately incompatible in olivine (V, Ga), but moderately compatible in chromite (D~3-6), and hence their behaviour in magmas will depend on the relative proportions of the two phases that are crystallizing. Simple fractional crystallization models are developed that monitor the change in element behaviour based on the relative proportions of olivine to chromite in the crystallizing assemblage; from "normal" cotectic proportions involving predominantly olivine, to chromite-only crystallization. Comparison of models to the natural chromite V-Ga array suggests that the overall positive correlation between these two elements is consistent with chromite formed from komatiite magma crystallizing olivine and chromite in normal cotectic proportion, and no evidence of the strong depletion in these elements expected for chromite-only crystallization. The spread in the Ga-V data can be explained if the magma responsible for chromite formation has assimilated up to ~10% of wall-rock banded iron formation, or granodiorite, or up to 50% of metasediment. The Zn-Ga variation amongst the RoFIS chromitites shows large variation, well outside that expected for the extent of crystallization or assimilation that can reproduce the V-Ga array. This is interpreted to be the consequence of both the availability and mobility of zinc at subsolidus conditions. A filter applied to the data to exclude the most silicate-rich, and hence "zinc exchangeable" samples, as well as those with visible alteration, results in a small subset of samples whose zinc contents are consistent with BIF assimilation, excluding granodiorite or metasediment as important contaminants, at least for the samples considered. Despite the evidence for contamination, results suggest that the RoFIS chromitites crystallized from normal cotectic proportions of olivine to chromite, and therefore no specific causative link between contamination and chromitite formation. The specific fluid dynamic regime during magma emplacement may therefore be resposible for crystal sorting and chromite accumulation. Ongoing work will be to conduct laboratory experiments to better constrain the partitioning of Ga, V and Zn between olivine, chromite and komatiite at conditions relevant to genesis of the RoFIS to further refine the crystallization models developed thus far.

INTRODUCTION AND MOTIVATION

Chromite is a nearly ubiquitous accessory mineral in primitive basaltic and komatiitic magmas, yet economically significant accumulations of chromite are so rare that none were known in North America until the discovery of the Ring of Fire Intrusive Suite (RoFIS) deposits less than fifteen years ago. Questions about the ore-forming process responsible for producing ore-grade, high-tonnage accumulations of chromite can be distilled into a choice between two competing hypotheses: 1) chromitite deposits formed predominantly due to fluid dynamical process involving crystal sorting from otherwise unremarkable komatiite magmas in exceptionally large and long-lived conduits (Eales, 2000; Mondal and Mathez, 2007; Voordouw et al., 2009; Marques, et al., 2017), or 2) the rarity of chromitite deposits results from a need for komatiitic magmas to have interacted with a highly specific and unusual combination of contaminants, or more evolved magma compositions during transit through the crust (Irvine, 1975, 1977; Spandler et al., 2005; Lesher et al., 2019). As in many scientific controversies, successful resolution may require some degree of synthesis of the two end-member viewpoints. In Phase 1 of this project, it was proposed that the predictions stemming from these two hypotheses could be tested by conducting a series of experiments under controlled conditions of temperature (T), pressure (P), and oxygen fugacity (fO_2), in which a primitive komatiitic melt of the type presumed to have been parental to the RoFIS deposits was combined with a variety of contaminants (e.g., granodiorite, iron-rich metasediment, banded iron formation) and compared with a base case in which no contamination occurs. Results of that work (Keltie, 2018; manuscript in preparation) have provided additional insights into the chromite-forming process with the important discovery being that iron is the essential additive that reduces the chromite solubility, and a scenario was developed showing that chromite-only precipitation was possible under certain

[1]Department of Earth Sciences, Dalhousie University, 1355 Oxford Street, Life Sciences Centre, Halifax, Nova Scotia B3H 4R2
[2]Department of Earth Sciences, Carleton University, 1125 Colonel By Drive, Ottawa, Ontario K1S 5B6
[3]Noront Resources, 886A Alloy Place, Thunder Bay, Ontario P7B 6E6

circumstances. Results from Phase 1 also indicate that the major element composition of contaminants may not be sufficiently different to be reflected in the chromite composition. However, by virtue of the different geochemical processes by which they form, the trace element signature of different contaminants may impart a unique chemical fingerprint on any resulting chromite. Therefore, the goals of Phase 2 of this project are two-fold: 1) to expand on the existing database documenting the trace element composition of ROFIS chromites and 2) to perform laboratory experiments to measure chromite-melt partition coefficients involving various komatiite-contaminant mixtures which have been doped with a suite of trace elements reflecting their distinct compositional types. Results of the partitioning experiments can then be used to calculate accurately the composition of chromite produced by different contaminant types, and more fully interpret the natural data. An additional outcome of this work will be a better assessment of whether the RoFIS chromitites from by "normal" cotectic crystallization of olivine and chromite, or chromite as the sole crystallizing phase.

In this report, the major and trace element composition of chromites from 45 samples taken from the Black Thor, Black Label, Big Daddy, and Blackbird deposits is presented, augmenting the dataset of Laarman (2014). Along with this data, the existing literature on olivine- and spinel-melt partitioning was surveyed in order to identify certain trace elements that are 1) readily detectable in the RoFIS chromites and 2) highly compatible in chromite, but incompatible in olivine, and hence sensitive to the proportions of these phases during crystallization. The survey revealed that gallium (Ga), vanadium (V), and zinc (Zn) all share these desirable properties. With this information simple models have been developed to predict the effect of differences in the olivine/chromite crystallization proportions, as well as various contamination scenarios, on the resulting covariation of these elements in chromite.

GEOLOGICAL SETTING

The Ring of Fire Intrusive Suite (RoFIS) comprises a series of mafic to ultramafic dikes, sills and layered intrusive bodies of komatiite origin emplaced into the McFaulds Lake Greenstone Belt (MLGB), with the entire succession located within the James Bay Lowlands of Northern Ontario (Figure 1). Age constraints on the RoFIS are derived from zircon U-Pb measurements on the tonalite host rock to the associated Eagle's Nest magmatic sulfide deposit and ferrograbbro emplaced within the RoFIS, yielding dates of 2773.4 +/- 0.9 and 2734.5 +/- 1 Ma, respectively (Mungall et al., 2010). The RoFIS contains five known chromitite deposits: Black Thor, Big Daddy, Blackbird, Black Label, and Black Creek (Figure 1). Together these deposits comprise ~201.3 million tonnes of measured and indicated chromite resources (Aubut, 2015). The deposits are hosted by serpentinised and talc-altered ultramafic rocks, and consist of disseminated to massive chromitite occurring as lenses and conformable continuous layers, in some cases reaching several meters in thickness, and up to km-scale in lateral extent. Detailed studies of the RoFIS chromitites have been done for Blackbird (Azar, 2010), Black Thor, Black Label and Big Daddy (Laarman, 2014) and the Black Thor Intrusive complex, which hosts the Black Label and Black Thor deposits (Carson et al., 2015). Of these studies, only Laarman (2014) has measured the trace element content of individual chromites, reporting on the abundances of 23 trace elements, with the notable exception of vanadium, which may be a useful element to unravelling chromitite genesis, as described below.

SELECTED SAMPLES

A total of 50 samples were selected for major and trace element analysis (45 of the 50 have now been measured). Chromite is generally fresh, although some magnetite rims were developed, and carefully avoided during analysis. Chromites are euhedral, exhibiting a remarkably uniform grain size, typically in the range of 50-200 microns. Some samples also contain chromite with spherical inclusions (see Figure 8 of Azar, 2010), hosting various combinations of albite, enstatite, chlorite, tremolite, phlogopite and amphibole, similar to reported at other localities (e.g. Muskox, Stillwater and Bushveld; Irvine, 1977; Spandler et al.,2005; Li et al., 2005). Although relict olivine is present in a few samples, the primary silicate mineralogy has been largely replaced by serpentine, talc, a fine dusting of magnetite and in some cases chlorite and carbonate. Samples can be broadly classified into three textural types based on the abundance of the interpreted primary silicate mineralogy, with all exhibiting a cumulate texture. The first, termed chromite-bearing dunite (Figure 2a) contains < 10 modal % chromite, and consists of mm-sized olivine pseudomorphs surrounded by chromite grains in a "necklace-like" texture, with altered silicate material interstitial to the chromite. The second, termed "porphyritic" chromitite (Figure 2b) is similar to the first type, but contains significantly more chromite (>50 modal %), surrounding mm-sized former olivine crystals. Note that former olivine in both of these textural types contain few or no chromite inclusions, suggesting olivine was the primary liquidus phase, followed by chromite. The third textural type is termed cumulate chromitite (Figure 2c), and contains >90 modal % chromite, in a fine grained matrix of altered silicate material. For each sample, at least 10 analyses were done on the cores of chromite crystals that were selected based on size (at least > 25 microns, which was the minimum useful laser spot size) and lack of silicate inclusions or magnetite rims.

ANALYTICAL PROCEDURE

Major element analysis: The major element composition of chromites was determined using the JEOL JXA-8200 Electron Probe Micro-Analyzer (EP eved for ^{115}In, ^{238}U/^{232}Th

signal ratio of ~1, and $^{232}Th^{16}O/^{232}Th$ <0.005. Chromites were analyzed using a laser repetition rate of 10-20 Hz, spot size of 25-75 µm, and laser output of ~8 J/cm^2. Factory supplied time resolved software was utilized for the acquisition of individual analyses. A typical analysis involved 20 seconds of background acquisition with the ablation cell being flushed with He, followed by laser ablation for 60 seconds, then 60 seconds of cell washout. Analyses were collected in a sequence in which two analyses were done on a standard reference material (NIST610) at the start of the acquisition cycle, then after every 20 analyses on the unknowns. When possible, 10 analyses were done on each sample. Data reduction was done off-line using the Iolite version 3.6 software package. Trace element concentrations were quantified using the NIST610 silicate glass, which contains 69.7 wt% SiO_2, 11.4±0.2 wt% CaO, 413±46 µg/g P, 455±10 µg/m Sc, 452±10 µg/g Ti, 450±9 µg/g V, 458±9 µg/g Fe, 410±10 µg/g Co, 458.7±4 µg/g Ni, 441±15 µg/g Cu, 460±18 µg/g Zn, 433±13 µg/g Ga, 447±78 µg/g Ge, 325±18 µg/m As, 515.5±1 µg/g Sr, 462±11 µg/g Y, 448±9 µg/m Zr, 417±21 µg/g Mo, 270±16 µg/g Cd, 434±19 µg/g In, 430±29 µg/g Sn, 396±19 µg/g Sb, 435±12 µg/g Hf, 446±33 µg/g Ta, 444±29 µg/g W, 426±1 µg/g Pb, 384±26 µg/g Bi, 457.2±1 µg/g Th, and 461.5±1 µg/g U (Jochum et al., 2005). Ablation yields were corrected by referencing to the known concentration of Mn as determined by EPMA. The following isotopes were measured (italized species used for quantification when multiple isotopes measured): ^{29}Si, ^{31}P, $^{43}\mathit{Ca}$, ^{44}Ca, ^{45}Sc, $^{47}\mathit{Ti}$, ^{48}Ti, ^{51}V, ^{57}Fe, ^{59}Co, ^{60}Ni, $^{63}\mathit{Cu}$, ^{65}Cu, $^{66}\mathit{Zn}$, ^{67}Zn, $^{69}\mathit{Ga}$, ^{71}Ga, ^{72}Ge, ^{75}As, ^{88}Sr, ^{89}Y, ^{90}Zr, ^{95}Mo, ^{111}Cd, ^{115}In, $^{118}\mathit{Sn}$, ^{119}Sn, ^{120}Sn, ^{121}Sb, ^{178}Hf, ^{181}Ta, ^{182}W, ^{208}Pb, ^{209}Bi, ^{232}Th, ^{238}U. Agreement within error was obtained for concentrations of Ga and Zn determined for all the isotopes measured, indicating negligible interference from higher concentration transition metal oxides (i.e., $^{53}Cr^{16}O$ on ^{69}Ga, etc). Table A2 provides a summary of the trace element composition of the RoFIS chromites.

External Standards: Two basalts from a suite of USGS reference materials, BHVO-1 and BIR-1, were used to test the accuracy of the LA-ICPMS glass analyses. Glasses were prepared by fusing powders at 1400°C and 1 GPa for 30 minutes in high purity graphite. Analyses of the BHVO-1 and BIR-1 glasses were done in the same analytical sessions to measure glass unknowns. Included in Table A2 are the results of these measurements and indicates that most measured values agree within 1 standard deviation of the preferred values from Jochum et al. (2005).

RESULTS AND DISCUSSION

Approach to modelling: The experimental results of Keltie (2018) indicate that the effect of increased iron in a melt is to lower the solubility of chromite, suppress the olivine crystallization temperature, and reduce the amount of olivine that will form. Therefore, given sufficient chromium in the initial magma, it is possible, through contamination by an Fe-rich component, to reverse the normal order of olivine-first crystallization, and induce chromite to form as the sole liquidus phase over a limited temperature interval. Although these experimental results suggest the plausibility of this process as a mechanism to form monomineralic layers of chromite, the question arises as to the evidence for this process in natural samples. As determined from the variation in Cr with MgO in komatiite suites (Barnes, 1998) the approximate cotectic proportion of olivine/chromite is 50, corresponding to 2 wt% chromite in the crystallizing assemblage. This is also consistent with the experimental results of Murck and Campbell (1986). Therefore, in order to identify chromitites that have formed by segregation from magmas crystallizing the normal olivine/chromite cotectic proportions, from those produced by chromite-only crystallization, evidence should be sought using the covariation of elements with significantly different olivine- and chromite-melt partition coefficients. A survey of the experimental literature has revealed that the elements V, Zn and Ga share these characteristics, with each being moderately compatible in chromite (with chromite/melt, D^{Chr} >1), and weakly to strongly incompatible in olivine (D^{ol} < 1; Table 1). Moreover, all three elements are readily detectable in the RoFIS chromitites, with no significant analytical issues in their measurement. However, some complications arise when considering which partition coefficients to apply to modelling the natural dataset, as the D values for V vary as a function of fO_2, and there also appears to be some mineral compositional effect, with V more compatible in Cr-spinel than Al-spinel, with the opposite true for Zn and Ga. In terms of the fO_2 dependence on the D for V, as mentioned above, Keltie (2018) has estimated the fO_2 for the Black Thor deposit of near FMQ, with resulting D^{Chr} for V in the range of 4-9 (Table 1). Clearly, a single set of partition coefficients for both olivine and chromite involving the same melt composition and at identical conditions would be highly useful, and is the focus of ongoing experiments. For the purpose of this report, values of partition coefficients are chosen to be consistent with the current database, and also provide a reasonable match to the composition of the presumed least differentiated chromitites, and are summarized in Table 2.

3 portrays the variation in the liquid concentration (CL) relative to the initial concentration (Co) as a function of the fraction of liquid remaining (F) for fractional crystallization models involving V, Zn and Ga and different proportions of crystallizing olivine and chromite. Curves are presented for different values of the bulk partition coefficient, defined as the sum of the individual partition coefficients multiplied by their mass fraction in the crystallizing assemblage. These models simulate the change in element behaviour as the crystallizing assemblage transitions from the normal cotectic proportion of 2% chromite (bulk D for V and Ga <1, Zn is ~1), to the "crossover" point for V and Ga, at ~ 10-19% chromite (bulk D for V and Ga ~1), to chromite-dominated crystallization (bulk D for V, Ga and Zn >1).

Application of these models for individual elements is hampered by the lack of information on the fraction of liquid represented by a specific chromite composition. Instead, model curves are provided for the co-variation of element pairs, representing the 0-50% crystallization interval, and are portrayed in Figures 3-6. In the models shown, the initial liquid composition is assumed to be equivalent to a primitive Munro Township komatiite (Table 2), using the compositional data of Sossi et al. (2016). Chromite compositions are calculated from model liquid compositions by multiplying by the chromite/melt partition coefficient for that element (Table 2). In terms of the V-Ga variation, data portrayed in Figure 4a show a broad positive correlation between V and Ga, which is consistent with the variation expected for crystallization of the normal cotectic proportions. Higher proportions of chromite in the crystallizing assemblage would shift the model curves to encompass more of the compositional array, but this amounts to an ad hoc increase in the modal amount of chromite without any experimental justification. Importantly, the V-Ga array is completely inconsistent with the crystallization of a chromite-dominated assemblage in which the bulk D is >1. In terms of the co-variation of Zn with Ga (Figure 4b), the predicted crystallization path is horizontal, with unchanging Zn and increasing Ga for the normal cotectic proportions (D Zn ~ 1, D Ga <1), then progressively decreasing Zn with Ga as the modal proportion of chromite increases, until both Zn and Ga decrease with increasing F for chromite-dominated crystallization. Although the range of model Ga abundances partially reproduces the observed array, model Zn contents are significantly below the measured values.

An alternative to closed system crystallization models is that the composition of the chromite-forming parental komatiite has been altered by contamination, thus shifting the point of origin for the model crystallization trajectories. Both Azar (2010) and Carson et al. (2015) show that the whole-rock lithophile trace element content of chromitite from the Blackbird deposit and from the Black Thor Intrusive Complex are consistent with assimilation of some combination of local country rocks (granodiorite, banded iron formation and metasediments). Physical evidence for contamination by banded iron formation comes from the occurrence of partially digested xenoliths in the magmatic host rocks to the Blackbird deposit (Azar, 2010). The effect of contamination has been modelled here by calculating mixtures of Munro Township komatiite with the granodiorite, metasediment and banded iron formation compositions reported in Mungall et al (2010) and Azar (2010; Table 2), and the resulting fractional crystallization trajectories. Figure 5 portrays the results for Ga and V, and that in all cases, the locus of the starting point is moved to higher Ga concentrations, with modest to significant decrease in V, depending on the specific contaminant type. All three contaminant types shift the model trajectories in a manner consistent with the natural compositional array, although the low Ga content of the metasediment requires up to 50 wt% addition of that component, but this seems a geologically unreasonable amount. Figure 6 portrays the Zn-Ga model results, and shows that, by virtue of the relatively low Zn content of the metasediment and granodiorite, model curves shift to trajectories that are below the uncontaminated case, clearly excluding those materials as significant additives. In contrast, the elevated Zn content of banded iron formation modifies the contaminated trajectories to be more consistent with the natural compositions, but the amount of this material required to reproduce the Ga-V array (10%) is too low to account for Zn concentrations above ~600 ppm. Unlike the more highly charged, and therefore more slowly diffusing Ga^{4+} and $V^{3+,4+}$, Zn^{2+} is likely to be prone to more efficient subsolidus exchange between chromite and other coexisting phases, such as olivine, or its alteration products. This is supported by clear evidence for Fe-Mg exchange between chromite and olivine to temperatures < 700°C, as reflected by olivine-chromite thermometry in samples from Black Thor reported in Keltie (2018). Also, olivine and other silicates are likely to provide a very limited amount of Ga or V for low temperature exchange, given their incompatibility in those phases. In contrast, the olivine-melt D for Zn is close to one. Indeed, amongst the samples measured for this report, those displaying the chromite-bearing dunite textural type, and hence highest in Zn-exchangeable silicate material, yield the most elevated Zn concentrations in the chromite. To minimize the influence of subsolidus disturbance on the chromite Zn-Ga array, the dataset was filtered to consider only the chromitite textural type. Unfortunately, there may also be an influence of external sources to the Zn budgets of even the most silicate-poor samples, as after filtering the data in this manner, several Zn-enriched samples were still identified, and all display obvious cross-cutting veins (Figure 7). The resulting Zn-Ga array after excluding those samples (Figure 8) as well is signficantly reduced in number, but the levels of Zn now appear to be within the range that could be achieved by modest levels of banded iron formation contamination, suggesting this is a more likely contaminant, at least for the least altered samples for which this test can be made.

As a final point to this section, it should be emphasized that although there is evidence for contamination in the RoFIS, as reflected both texturally, and in the trace element chemistry of the chromites, that on its own does not either support or deny a causative link between contamination and chromitite formation. In this context, the link between BIF assimilation, and magnetite "upgrading" as proposed by Lesher et al (2019) is unlikely in the context of the work by Keltie (2018), who showed that komatiites have an extraordinary capacity to dissolve FeO. For example, at 1390°C, and the FMQ buffer, a komatiite can dissolve around 66 wt% FeO before saturating in magnetite, so it is difficult to envisage how this mineral would survive contact with a komatiite host, even if the host were already saturated in chromite. Importantly, however, the chromite Ga-V compositional arrays suggest "normal" crystallization of olivine-chromite cotectic proportions, despite contamination. It therefore seems plausible that instead of being the result of chemical influences, the RoFIS chromite segregations could form because of the specific fluid dynamic

regime of the magma emplacement process, and subsequent crystal sorting, as proposed by Azar (2010).

SUMMARY

The essential results of this research can be summarized as follows:

1. A total of 45 chromite-bearing samples from the Black Thor, Big Daddy, Blackbird, Black Label chromite deposits have been analysed for major and trace elements. The sample suite represents three textural groups largely defined by the silicate/chromite ratio.
2. Ga, Zn and V are elements that are both readily detectable in the RoFIS chromitites, and show contrasting behaviour in their olivine- and chromite-melt partitioning (Table 1), each being moderately compatible in chromite, and ambivalent to moderately incompatible in olivine. These partitioning data are used to develop simple fractional crystallization models in which the bulk partition coefficient is varied from "normal" cotectic proportions involving predominantly olivine, to chromite-only crystallization.
3. The RoFIS chromite V-Ga array is consistent with chromite formed from komatiite magma crystallizing olivine and chromite in normal cotectic proportion, and the spread in the Ga-V data is consistent with crystallization from a magma that has assimilated up to ~10% of wall-rock banded iron formation, or granodiorite, or up to 50% of metasediment.
5. The RoFIS Zn-Ga array shows large variation, well outside that expected for the extent of crystallization or assimilation that can reproduce the V-Ga array. A filter applied to the data to exclude the most silicate-rich, and hence "zinc exchangeable" samples, as well as those with visible alteration, results in a small subset of samples whose zinc contents are consistent with BIF assimilation, excluding granodiorite or metasediment as important contaminants, at least for the samples considered.
6. Despite the evidence for contamination, results suggest that the RoFIS chromitites crystallized from normal cotectic proportions of olivine to chromite, and therefore no specific causative link between contamination and chromitite formation. The specific fluid dynamic regime during magma emplacement may therefore be resposible for crystal sorting and chromite accumulation.
7. The exisiting dataset for olivine and chromite-melt partitioning of Ga, V and Zn has shown that values depend on both mineral composition and fO^2, therefore imposing some limitation on their use to accurate modeling in the RoFIS context. Further work in this project will focus on the requisite laboratory partitioning measurements.

ACKNOWLEDGEMENTS

Funding for this research was generously provided by Targeted Geoscience Initiative grants from Natural Resources Canada and by student research grants from the Society of Economic Geologists. We thank Dan MacDonald for ably setting up the necessary analytical protocals for the EMP analysis of chromite.

REFERENCES

Aubut, A.
2015. Black Thor, Black Label, and Big Daddy chromite deposits, McFaulds lake Area, Ontario, Canada. National Instrument 43-101 Technical Report prepared for Noront Resources Ltd.

Azar, B.
2010: The Blackbird Chromite deposit, James Bay Lowlands of Ontario, Canada: Implications for chromitite genesis in ultramafic conduits and open magmatic systems. MSc thesis, University of Toronto.

Barnes, S. J.
1998: Chromite in Komatiites, 1. Magmatic Controls on Crystallization and Composition. Journal of Petrology 39(10), 1689-1720.

Canil, D.
2002: Vanadium in peridotites, mantle redox, and tectonic environments: Archean to present. Earth and Planetary Science Letters, 195: 75-90.

Canil, D.
1999: Vanadium partitioning between orthopyroxene, spinel and silicate melt and the redox states of mantle source regions for primary magmas. Geochimica et Cosmochimica Acta, 63(3): 557-572.

Canil, D., Fedortchouk, Y.
2001: Olivine-liquid partitioning of vanadium and other trace elements, with applications to modern and ancient picrites. The Canadian Mineralogist, 39: 319-330.

Carson, H.J.E., Lesher, C.M., and Houlé, M.G.
2015: Geochemistry and petrogenesis of the Black Thor intrusive complex and associated chromite mineralization, McFaulds Lake greenstone belt, Ontario In: Targeted Geoscience Initiative 4: Canadian Nickel-Copper-Platinum Group Elements-Chromium Ore Systems — Fertility, Pathfinders, New and Revised Models, (ed.) D.E. Ames and M.G. Houlé; Geological Survey of Canada, Open File 7856, p. 87–102.

Davis, F.A., Humayun, M., Hirschmann, M.M., Cooper, R.S.
2013: Experimentally determined mineral/melt partitioning of first-row transition elements (FRTE) during partial melting of peridotite at 3 GPa. Geochimica et Cosmochimica Acta, 104: 232-260.

Eggins S.M., Kinsley L.P.J., & Shelley J.M.M.
1998: Deposition and element fractionation processes during atmospheric pressure laser sampling for analysis by ICPMS. Appl. Surf. Sci, 127-129, 278-286.

Horn, I., Foley, S.F., Jackson, S.E., Jenner, G.A.
1994: Experimentally determined partitioning of high field strength and selected transition elements between spinel and basaltic melt. Chemical Geology, 117: 193-218.

Irvine, T.N.
1975: Crystallization sequences in the Muskox intrusion and other layered intrusions—II. Origin of chromitite layers and similar deposits of other magmatic ores: Geochimica et Cosmochimica Acta, v. 39, p. 991–1020

Irvine, T.N.
1977: Origin of chromite layers in the Muskox intrusion and other stratiform intrusions: A new interpretation: Geology, v. 5, p. 273–277

Jochum, K.P., Nohl, U., Herwig, K., Lammel, E., Stoll, B., and Hofmann, A.W.
2005: GeoReM: A New Geochemical Database for Reference Materials and Isotopic Standards. Geostandards and Geoanalytical Research, 29: 333-338.

Keltie, E.E.
2018: An Experimental Study of the Role of Contamination in the Formation of Chromitites in the Ring of Fire Intrusive Suite. M.Sc. thesis, Dalhousie University, 146 pp.

Laarman, J. E.
2014: A Detailed Metallogenic Study of the McFaulds Lake Chromite Deposits, Northern Ontario. Ph.D. thesis, Western University, 529 pp.

Lesher, C.M., Carson, H.J.E. and Houlé, M.G.
2019: Genesis of chromite deposits by dynamic upgrading of Fe + Ti oxide xenocrysts. Geology, vol 27, pp 207-210.

Li, C.S. Ripley, E.M., Sarkar, A., Shin, D.B., and Maier, W.D.
2005: Origin of phlogopite-orthopyroxene inclusions in chromites from the Merensky Reef of the Bushveld Complex, South Africa. Contrib. Mineral. Petrol. Vol 150, pp 119-130.

Mallmann,G., O'Neill, H.St-C.
2009: The crystal/melt partitioning of V during mantle melting as a function of oxygen fugacity compared with some other elements (Al, P, Ca, Sc, Ti, Cr, Fe, Ga, Y, Zr, and Nb). Journal of Petrology, 50(9): 1765-1794.

Metsaranta, R.T., Houle, M.G., McNicoll, V.J., and Kamo, S.L.
2015: Revised geological framework for the McFaulds Lake greenstone belt, Ontario. In Targested Geoscience Initiative 4: Canadian Nickel-Copper-Platinum Group Elements-Chromium Ore Systems – Fertility, Pathfinders, New and Revised Models, (ed.) D.E. Ames and M.G. Houle, Geological Survey of Canada, Open File 7856, 61-73. Rudnick, R.L. and Gao, S. (2004). Composition of the Continental Crust. In: Treatise on Geochemistry. Holland, H.D. and Turekian, K.K. (Editors), Elsevier, Amsterdam. 3: 1-64.

Spandler, C., Mavrogenes, J. and Arculus, R.
2005: Origin of chromitites in layered intrusions: Evidence from chromite-hosted melt inclusions from the Stillwater Complex. Geology, v. 33; no. 11; p. 893–896.

Sossi, P.A., Eggins, Nesbitt, R.W., Nebel, O., Hergt, J.M., Campbell, I.H., O'Neill, H.St.C., Van Kranendonk, M. and Davies, D.R.
2016: Petrogenesis and Geochemistry of Archean Komatiites. Journal of Petrology, vol 57, pp 147-184.

Voordoux, R., Gutzmer, J., and Beukes, N. J.
2009: Intrusive origin for Upper Group (UG1, UG2) stratiform chromitite seams in the Dwars River area, Bushveld Complex, South Africa. Mineralogy and Petrology 97(1-2), 79-94.

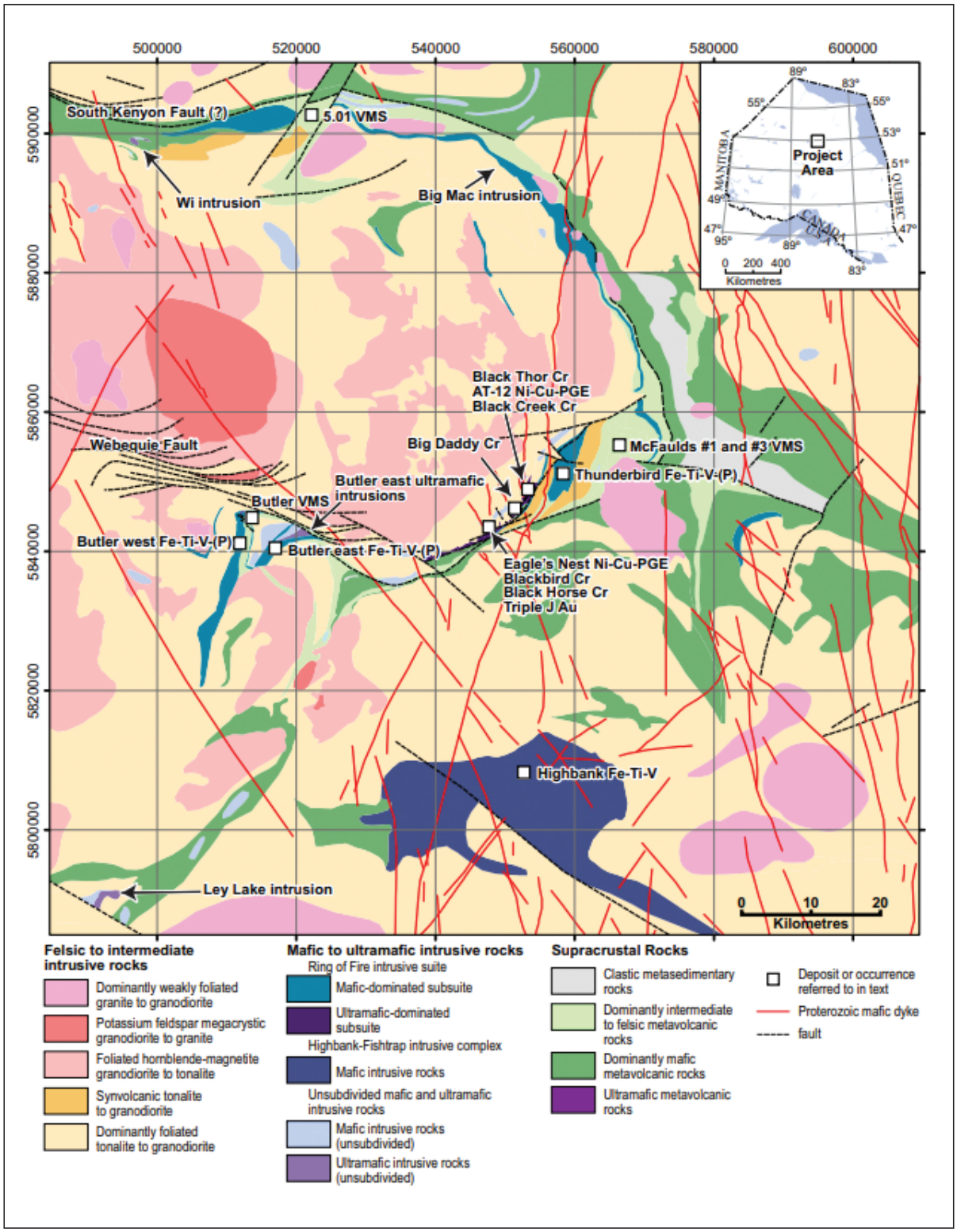

Figure 1. Geological map showing the spatial distribution of lithologies corresponding to the RoFIS, host rocks and chromite deposits. Colours and symbols are explained in the legend. From Metsaranta et al. (2015)

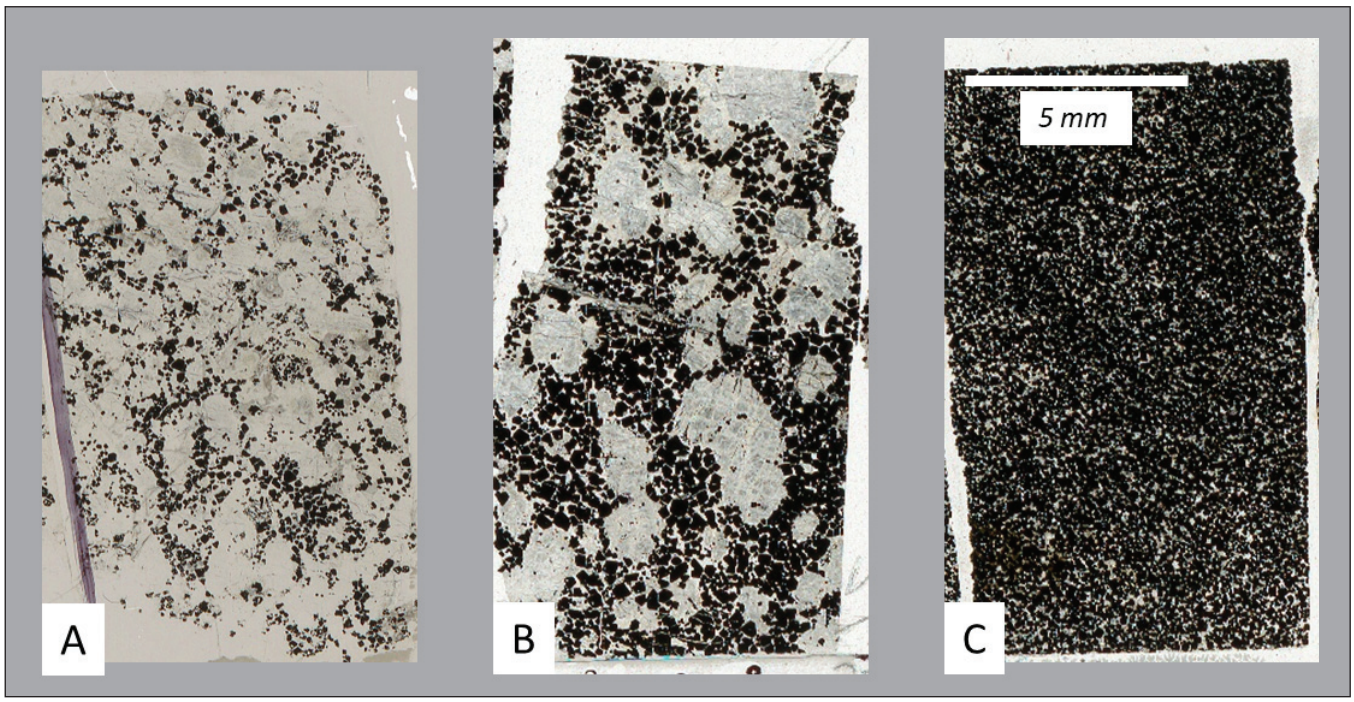

Figure 2. Images of polished thin sections showing examples of the the three textural types for chromite-bearing samples analysed in this study. A) Chromite-bearing dunite, comprised of < 10 modal % chromite, and dominated by cumulate-textured olivine. B) "Porphyritic" chromitite, comprised of > 50% chromite, with a bimodal grain size distribution involving larger olivine grains with a finer-grained chromite matrix. C) Cumulate chromitite, comprised of > 95% chromite, and minor interstitial silicates. The scale bar applies to all three images.

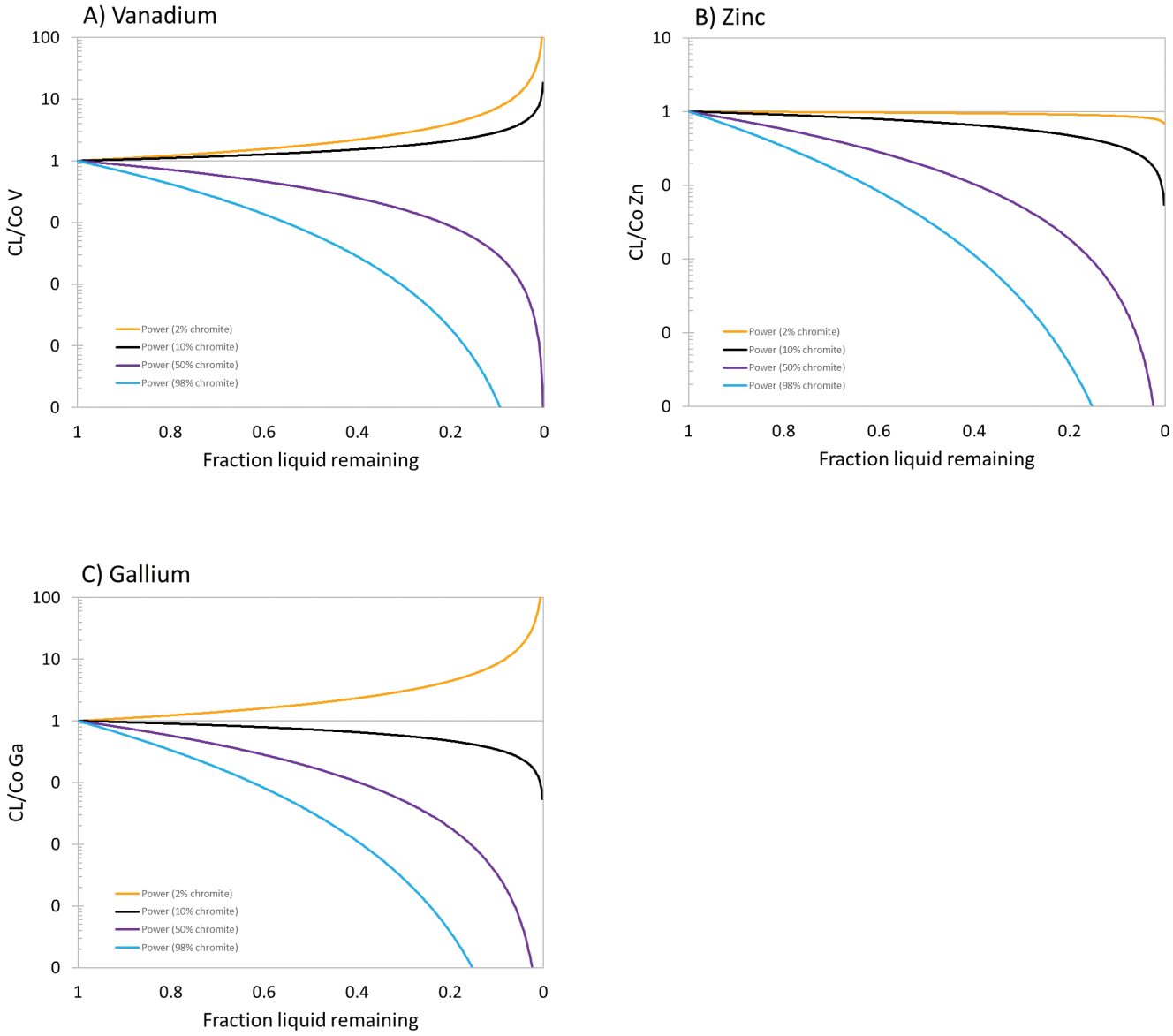

Figure 3. Concentration in the liquid (CL) relative to the initial concentration (Co) as a function of the fraction of liquid remaining (F) involving the fractionational crystallization of olivine:chromite mixtures, with proportions as indicated in the legend. The model for 2% chromite in the crystallization assemblage is consistent with olivine/chromite cotectic proportions inferred from the Cr-MgO variation in natural komatiites (Barnes, 1998) and from experiment (Murck and Campbell, 1986). A) The appoximate cross-over from V incompatible to compatible occurs when > 19 wt% chromite is present in the crystallizing assemblage. B) The appoximate cross-over from Zn incompatible to compatible occurs when > 2 wt% chromite is present in the crystallizing assemblage. C) The appoximate cross-over from Ga incompatible to compatible occurs when > 10 wt% chromite is present in the crystallizing assemblage.

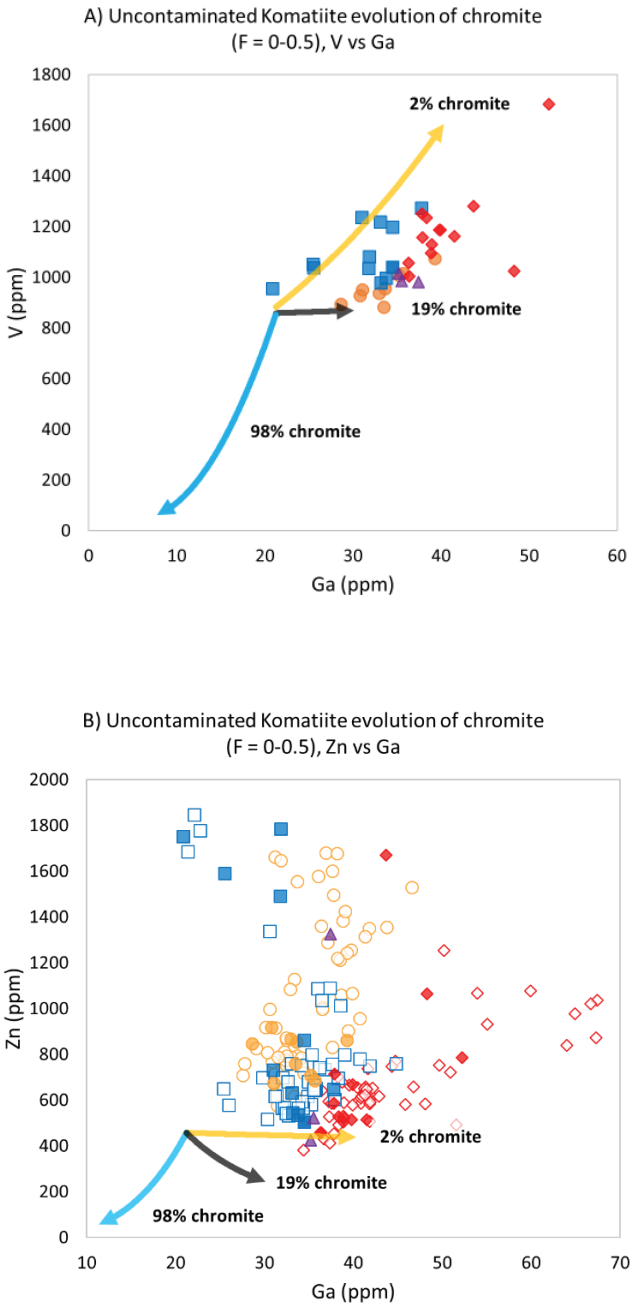

Figure 4. V vs Ga and Zn vs Ga covariation for samples from the RoFIS compared to model fractional crystallization curves involving different proportions of chromite in the olivine + chromite crystallizing assemblage. The initial liquid composition corresponds to a least differentiated Munro Township komatiite (Sossi, 2016). All filled symbols are from this study, open symbols from Laarman (2015): gold circles are Black Thor, blue squares are Black Label, red diamonds are Big Daddy, and violet triangles are Blackbird.

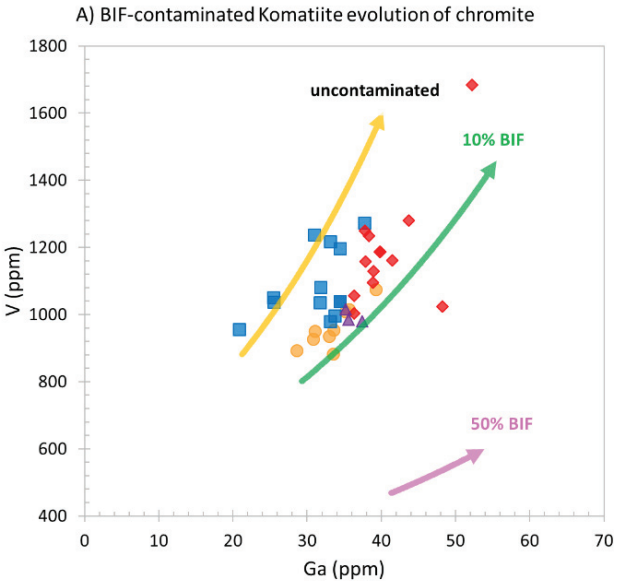

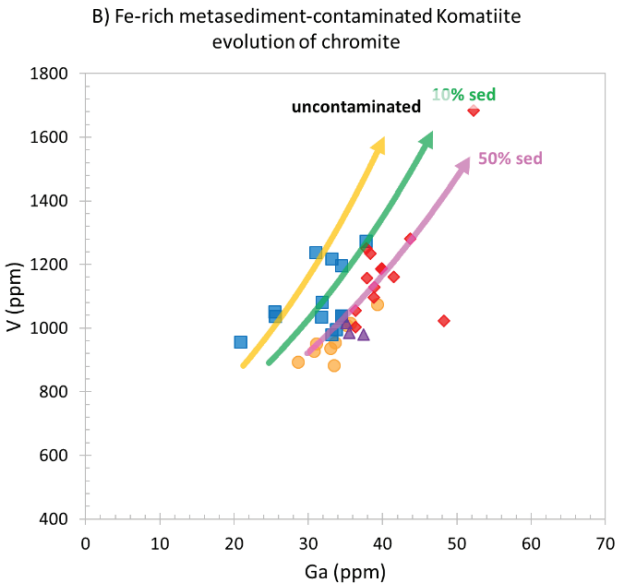

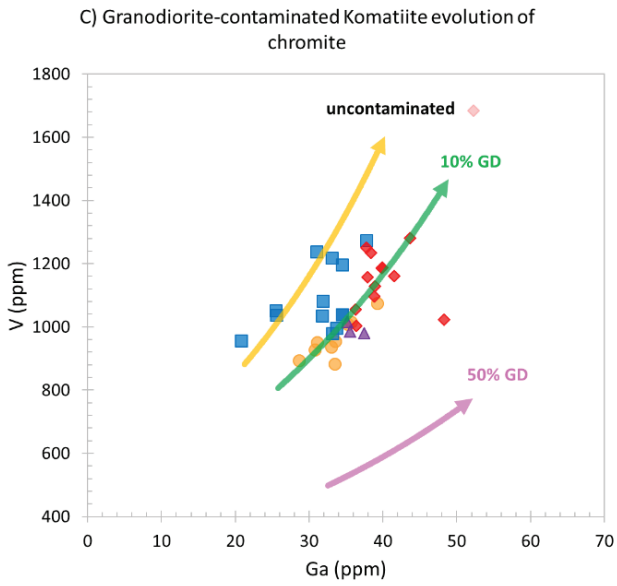

Figure 5. V vs Ga covariation with symbols as in Figure 6a and model fractional crystallization curves involving the normal olivine-chromite cotectic proportions for komatiite containing 0, 10 and 50 wt% of BIF, metasediment and granodiorite.

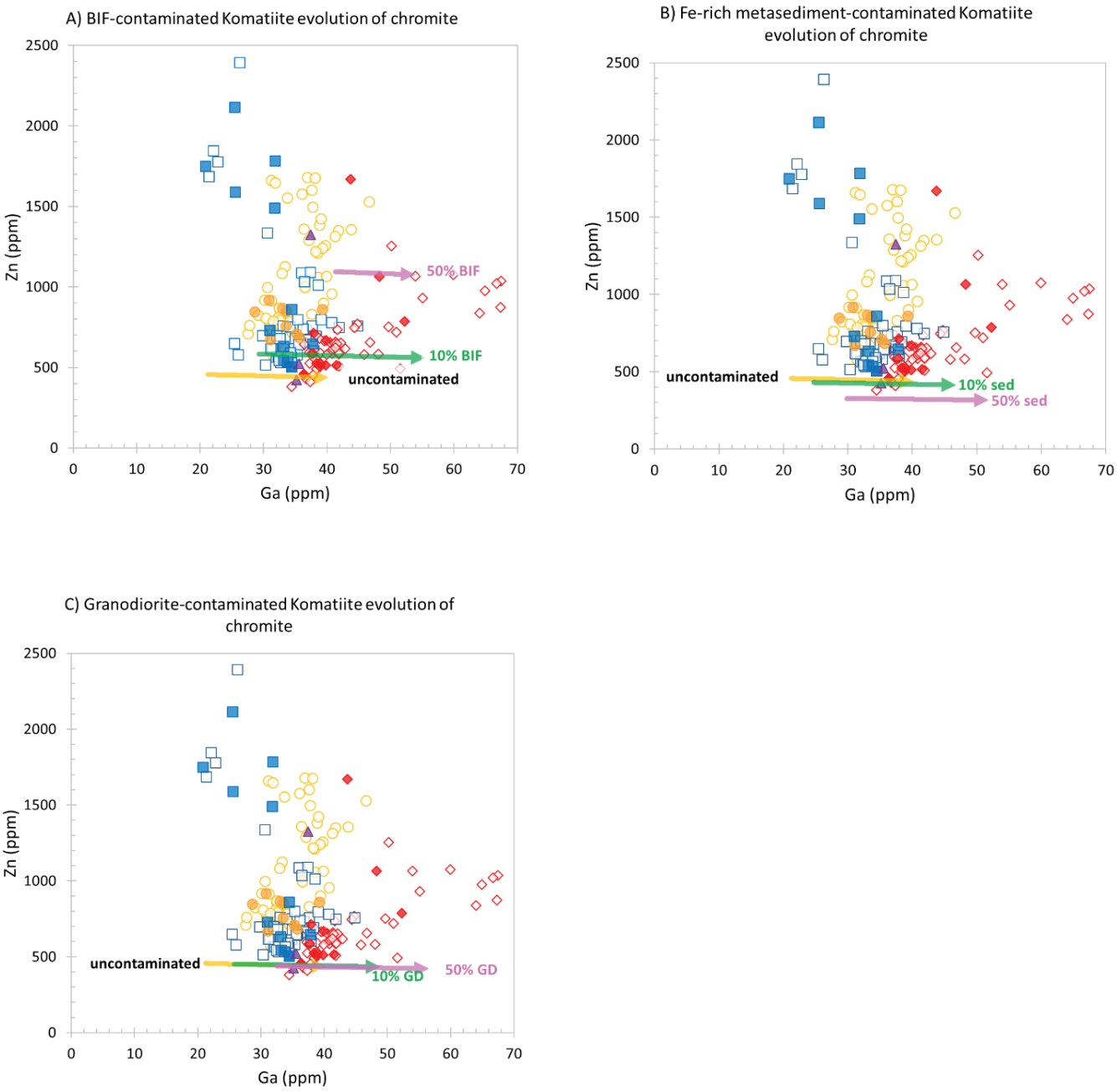

Figure 6. Zn vs Ga covariation, symbols as in Figure 6a with model fractional crystallization curves involving the normal olivine-chromite cotectic proportions for komatiite containing 0, 10 and 50 wt% of BIF, metasediment and granodiorite.

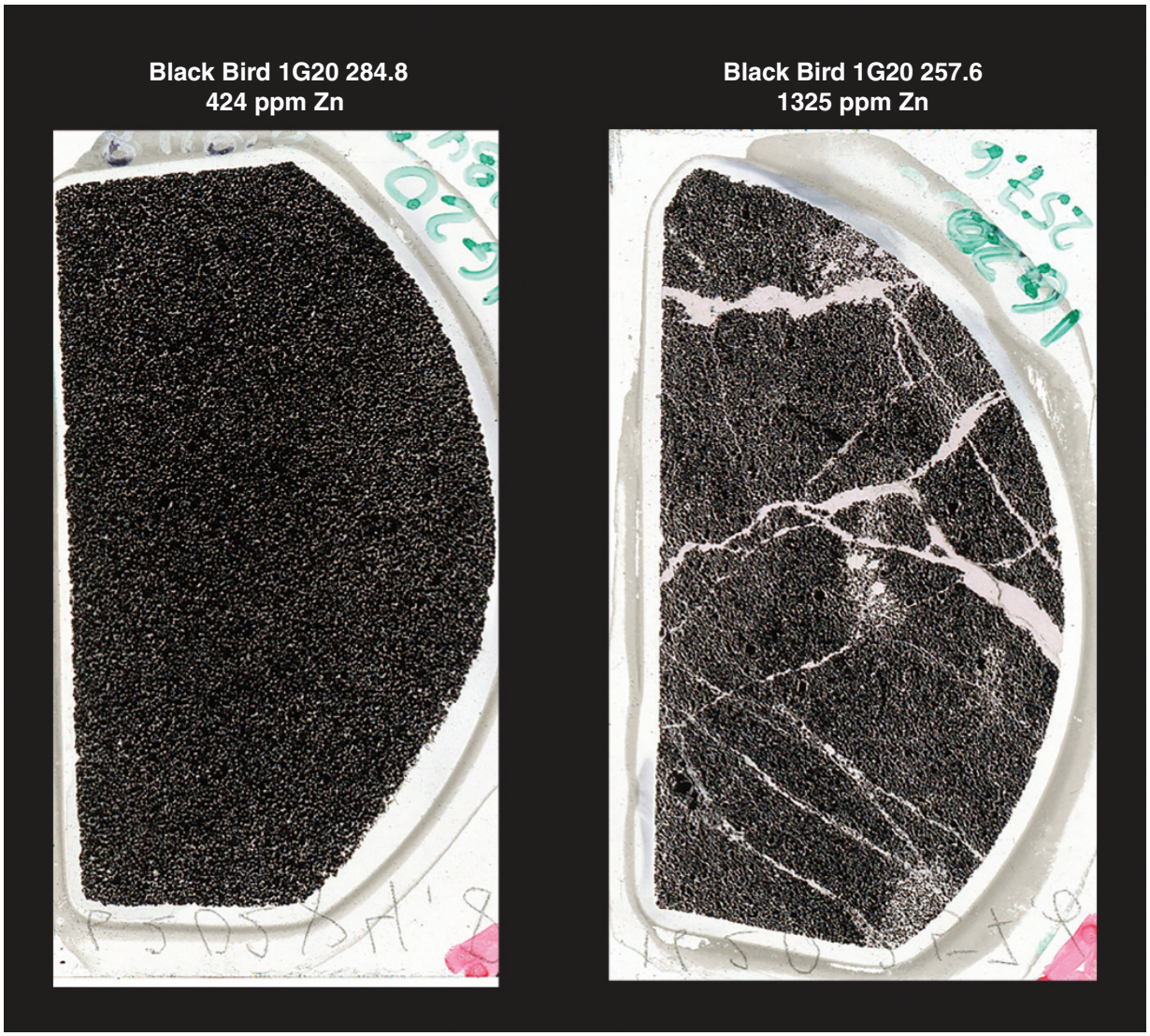

Figure 7. Images of polished thin sections showing examples of chromitites from the Black Bird deposit and the average Zn content of constituent chromites. Note the strong enrichment in Zn from the sample with visible veining.

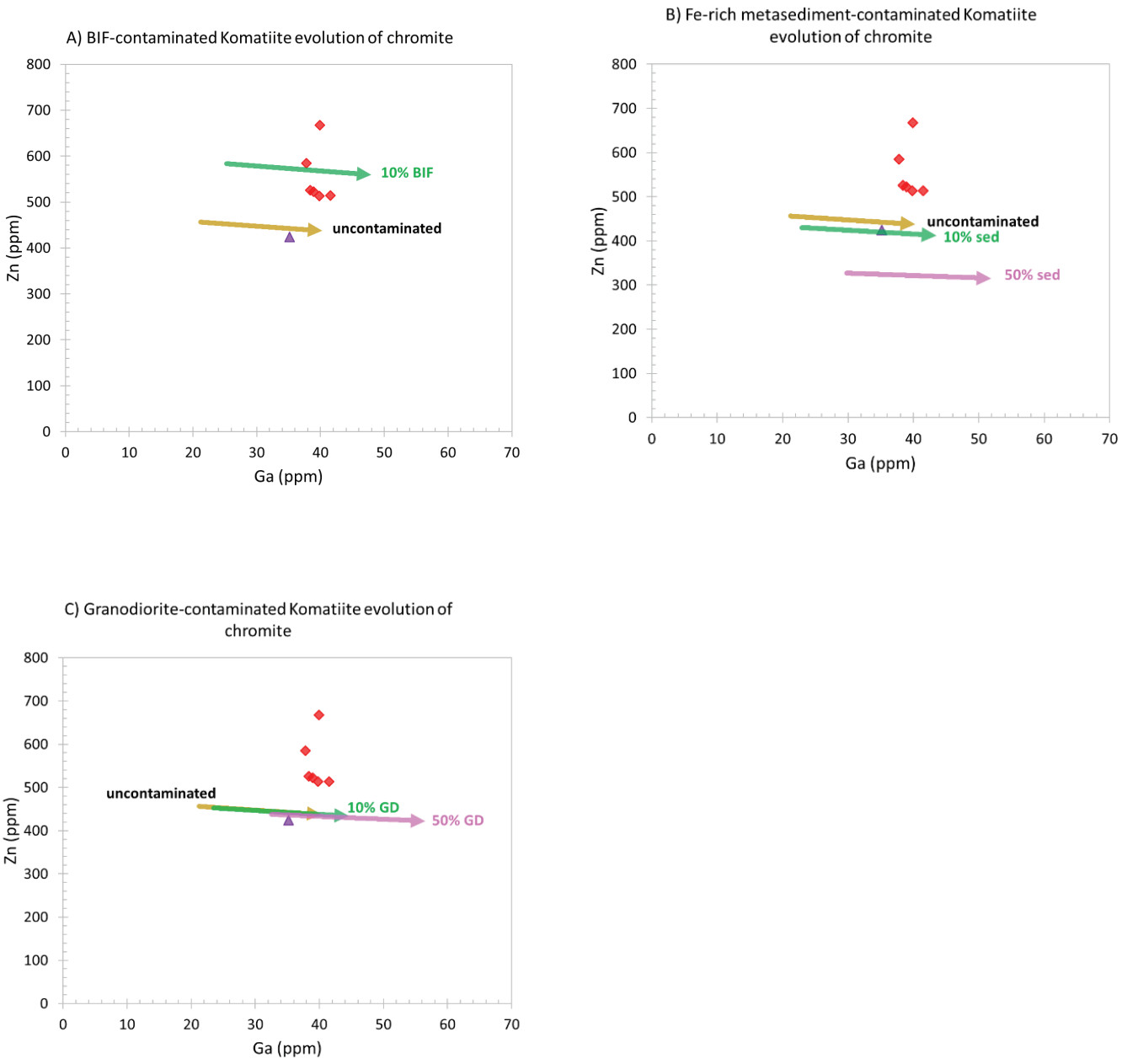

Figure 8. Zn vs Ga covariation, with symbols as in Figure 6a and model fractional crystallization curves involving the normal olivine-chromite cotectic proportions for komatiite containing 0, 10 and 50 wt% of BIF, metasediment and granodiorite. Samples shown are for only the chromitite textural type with no visible veining.

Textural, mineralogical, lithogeochemical and lead and thallium isotopic characterization of magmatic rocks in Selwyn Basin, Yukon: potential spatial and temporal linkages with lead-zinc mineralisation

E.J. Scanlan[1], M.I. Leybourne[1], D. Layton-Matthews[1], A. Voinot[1] and N.A. Van Wagoner[2]

Abstract: Alkaline to subalkaline magmatic rocks in the Selwyn Basin, Yukon may provide evidence of a genetic link to clastic sediment-hosted Pb-Zn deposits in the Anvil and MacMillan Pass districts. To examine if such a link is present, we document the petrography, lithogeochemical, and thallium isotopic compositions of magmatic rocks in these regions. Anvil District volcanic rocks are interpreted as basaltic effusive eruptions and phreatomagmatic surge and/or fall deposits, whereas samples from the MacMillan Pass district were emplaced by explosive eruptive activity. The MacMillan Pass samples contain large amounts of ankerite and calcite. Earn Group metavolcanic rocks from the Keno Hill area have few primary textures to identify eruption dynamics. This group is crosscut by a series of Triassic mafic dikes that exhibit little alteration or deformation. Samples of Marmot Volcanics from the Misty Creek Embayment are effusive basalts. Magmatism is alkaline in all regions except for Keno Hill, where both the Earn Group metavolcanic rocks and Triassic dikes are subalkaline. Six samples from the MacMillan Pass District have ε^{205}Tl values of -3.2 ± 1.8 to -14.2 ± 3.2. Five samples from the Anvil District have ε^{205}Tl values of 0.9 ± 1.9 to -6.4 ± 1.2. These preliminary data will be supplemented with additional analyses of mineralised horizons and host shales to investigate the link between high Ba and Tl contents in both the volcanic rocks and SEDEX deposits. Future work will constrain age relationships between mineralized samples and volcanism, use Pb, Sr and Nd to constrain magma sources and use Tl, Mo and potentially Ba isotopes to examine the link between mineralisation and magmatism.

INTRODUCTION

Clastic-sediment hosted deposits are one of the World's largest Pb-Zn reserves and producers. Our understanding of the formation and evolution of these deposits has changed from the historical ore genesis models of exhalation of metalliferous brines on the seafloor (e.g., Goodfellow and Lydon, 2007). Early models stated that clastic sediment-hosted deposits form as brines circulate in the sub-seafloor sediments, scavenge metals and are channelled along syn-sedimentary faults to then 'exhale' and deposit sulfides on the seafloor (Lydon, 1983; Leach et al., 2010). Following the generation of these ore genesis models, some sedimentary exhalative ('Sedex') deposits have been recognized as deviating from the classic exhalative model, with mineralisation forming through sub-seafloor mineral replacement processes as the metalliferous brines circulate (e.g. Red Dog, MacMillan Pass, Howard's Pass; Kelley et al., 2004, Magnall et al., 2016; Gadd et al., 2016). Sediment-hosted mineralisation has been considered by some to occur on a spectrum with volcanogenic massive-sulfide (VMS) deposits, with VMS deposits the magmatic-hydrothermal end member with sediment-hosted deposits as the purely hydrothermal end member (Large et al., 2001). There is, therefore, potential for large-scale, distal magmatism to provide heat and/or metals to sediment-hosted hydrothermal base metal sulfide systems (see Koski et al., 1985).

The Selwyn Basin in northwest Yukon, Canada contains several areas that host clastic sediment-hosted Pb-Zn deposits, including Howard's Pass, MacMillan Pass and the Anvil District (Fig. 1). Alkaline volcanic rocks are present in the Anvil and MacMillan Pass Districts, where they are both temporally and spatially associated with the mineral deposits. The aim of this project is to determine if there are any genetic linkages between magmatism and clastic sediment-hosted mineralisation in the region. To do this, several smaller research themes and questions are being investigated: 1) Characterisation of the petrogenesis of the volcanic rocks; 2) Determine the precise timing of volcanic rocks in the Selwyn Basin; 3) Do selected isotope systems show a correlation between the volcanic rocks and mineralisation?; and, 4) Are magmatic volatiles, metals and elements present in the sediment-hosted mineralisation? Herein, we focus on the geochemical and petrological characterisation of the products magmatism in the region, present preliminary thallium isotope results and detail future work.

[1]Department of Geological Sciences and Geological Engineering, Queen's University, 32 Union Street, Kingston, Ontario K7L 3N6
[2]Department of Physical Sciences, Thompson Rivers University, 900 McGill Road, Kamloops, British Columbia V2C 0C8

REGIONAL GEOLOGY

The sediments that comprise the Selwyn Basin, Yukon formed off the western margin of ancestral North America from the Late Proterozoic to Early Carboniferous (Nelson and Colpron, 2007) (Fig. 1). The Selwyn Basin is a series of rift-fill and marine facies deposited in an extensional basin (Fig. 2) surrounded by platformal carbonates (Nelson and Colpron, 2007). Cordilleran tectonics have deformed and metamorphosed parts of this region during terrane accretion (Dusel-Bacon et al., 2002; Mair et al., 2006). Alkalic rocks related to extensional tectonics are present throughout this region, ranging from the Cambrian to Late Devonian and interbedded with marine sedimentary facies (Goodfellow et al., 1995).

The geochemistry of alkaline volcanism in the Selwyn Basin has been documented by Goodfellow et al. (1995), who subdivided the volcanic rock into five groups based on their geochemical characteristics and geographic location. These groupings are related to partial melting of different mantle sources, with four groups from metasomatized lithospheric mantle and the other possessing an OIB signature that originates from partial melting of the asthenospheric mantle. For our study, samples from MacMillan Pass were collected from the MacMillan volcanics (as in Goodfellow et al., 1995) and Niddery volcanics (as in Goodfellow et al., 1995). In the Anvil District, we collected samples from the Menzie Creek volcanics (Jennings and Jilson, 1986). Within the Keno Hill district, volcanic rock samples were collected from the Earn Group, one of the sedimentary sequences that host Pb-Zn deposits in the region. Samples were also collected from a series of Triassic dikes in the Keno Hill district. Misty Creek Embayment samples represent the Marmot Formation (Cecile et al., 1982).

Within the Selwyn Basin are several clastic sediment-hosted Zn-Pb deposit districts. The Howard's Pass District has been well studied and contains fourteen Zn-Pb deposits with a [combined] grade of 400.7 Mt, 4.5 % Zn and 1.5 % Pb (Kirkham et al., 2012). The MacMillan Pass District contains several deposits (Tom, Jason, Boundary Creek) that are hosted in the shales and cherts of the Devonian Lower Earn Group (Goodfellow, 2004). There are five major Zn-Pb deposits in the Anvil District; Faro, Grum, Vangorda, DY and Swim (Shanks et al., 1987). These deposits occur within carbonaceous schist at the contact between the Mt. Mye and Vangorda Formations (Jennings and Jilson, 1986; Shanks et al., 1987).

METHODS

Lithogeochemistry and Pb Isotopes

A total of 140 samples were submitted to ALS Geochemistry in North Vancouver, B.C. for bulk lithogeochemical analysis and Pb isotopes. Whole rock samples were crushed and prepared by ALS in low-Cr-Mo mild steel ring mills. Major elements were measured using inductively coupled plasma-atomic emission spectrometry (ICP-AES) and trace elements and Pb isotopes were measured using inductively coupled plasma-mass spectrometry (ICP-MS). For description of the analytical methods used, see Leybourne et al. (2018).

Scanning Electron Microscopy

Selected samples were crushed, and heavy minerals separated by Overburden Drilling Management Ltd. (ODM). Samples were disaggregated using the SELFRAG at Queen's University and then the fraction that was > 1 mm milled using a BICO crusher to < 1 mm at ODM, with a quartz cleaner used between each sample. The < 1 mm fraction was micropanned for any zircons and the remaining material was refined using heavy liquid separation at a specific gravity of 3.3. For full methodology see McClenaghan (2011). Heavy mineral separates of selected samples were set in epoxy under a vacuum for five minutes to remove air bubbles before it was poured into the grain mount cast. Samples were then polished up to a 1 µm grit size for scanning electron microscopy (SEM). Polished thin sections for petrographic analysis were prepared at the Harquail School of Earth Sciences, Laurentian University.

Thin sections and epoxy mounts were analysed on a FEI Quanta 650® field emission gun environmental scanning electron microscope (FEG ESEM) under a low vacuum without a carbon coat at the Queen's Facility for Isotope Research (QFIR). A mineral liberation analysis (MLA) using extended backscattered electron (XBSE) liberation analysis (Fandrich et al., 2007) was completed to identify grains with a high brightness in backscattered electron signal corresponding to minerals with a high density e.g., sulfides and zircons. Mineral spectra were then matched to the QFIR MLA database, with each mineral spectrum manually confirmed.

Thallium Isotopes

Fifteen samples from the Anvil and MacMillan Pass Districts were analysed for thallium isotopes at the QFIR. Samples were digested, eluted and measured on a Thermo-Finnigan Neptune® multi-collector ICP-MS following the methods described in Peter et al. (2018).

Zircon dating

One sample was sent to Boise State University for Pb-Pb geochronology of zircons using chemical abrasion thermal ionisation mass spectrometry (CA-TIMS). Six other samples are currently being analysed using this method. Both sample preparation and analysis were completed at Boise State University. The one sample was measured on a GV Isoprobe-T multi collector-thermal ionisation mass spectrometer with an ion-counting Daly detector. For details on analytical methods see Wainman et al. (2018).

VOLCANIC TEXTURES AND ERUPTION STYLES

Volcanic samples from each area in the Selwyn Basin are distinctive in appearance. In particular, the samples from MacMillan Pass display a distinctive orange surface weathering (Fig. 3A) caused by ankerite alteration. In this region,

volcanism is Middle to Late Devonian, and volcanic rocks have been identified in the Boundary Creek Pb-Zn mineral deposit, which formed during or following basaltic magmatism (Turner and Rhodes, 1990). Magmatism is dominantly extrusive, represented by breccias, lapilli tuffs and tuffs. In many of these volcaniclastic samples, the original matrix has been completely replaced by coarse-grained ankerite and/or calcite. Samples from the Anvil District display less surface weathering and display the typical green colour indicative of the chloritic hydrothermal alteration commonly seen in basalts. Primary features are still evident in the samples (Fig. 3B). These volcanic rocks are represented by basaltic flows, pillow basalts, tuffs, lapilli tuffs and breccias. Samples from the Misty Creek Embayment are similar in appearance to those from the Anvil District. Earn Group samples from the Keno Hill area are metamorphosed up to lower greenschist facies (Fig. 3C). Several of these samples display relict primary features, with small clasts present in tuffaceous rocks; however, the primary features in other samples have been destroyed during metamorphism. In the latter samples the mineral assemblages and bulk geochemical compositions have been used to identify a mafic igneous protolith. Triassic mafic dikes in this area have minor alteration, suggesting that alteration of volcanic rocks in the Keno Hill region predates emplacement of the Triassic dikes. (Fig. 3D)

Anvil District

In the Anvil District volcanic rocks are part of the Menzie Creek Formation and can be separated into three sample suites: 1) ash-rich tuffs, lapilli-tuffs and breccias, 2) fine-grained basalts, and 3) coarse-grained mafic intrusive rocks. Fine-grained tuffs with no clasts were deposited as thick tuffaceous (pyroclastic) flows. Several of these samples display weak bedding demarcated by variations in grainsize and chlorite alteration of larger minerals/clasts. Lapilli tuffs contain relict glass shards with cuspate margins and pumice fragments, which are commonly flattened (Fig. 4A-C). Crystal-rich tuffs contain primary clinopyroxene, orthopyroxene and/or plagioclase phenocrysts.

Many samples are basaltic with phenocrysts of olivine, pyroxene, plagioclase and rare sanidine (Fig. 4D). Veins and lenses of coarse calcite or ankerite crosscut basalt in places. Other basalts are hydrothermally altered with phenocrysts replaced by chlorite, epidote and chalcedony and vesicles filled by chlorite, sericite, chalcedony and/or carbonate (typically ankerite or calcite) (Fig. 4E). Small (20-50 mm diameter) peridotite xenoliths with skeletal olivine and pyroxene are present within one of the breccia samples. Two samples were collected from a breccia pipe with rusty-appearing basalt clasts and a malachite (+ carbonate) matrix.

Coarse-grained mafic and ultramafic intrusive samples north of the Anvil Pluton vary in composition; one sample (MC-22) is a wehrlite with relatively fresh olivine and clinopyroxene and rare orthopyroxene. Sample MC-23 is rich in olivine altered to serpentine, chlorite and talc, whereas another sample (MC-24) is a clinopyroxene-rich gabbro with skeletal plagioclase and titanite (Fig. 4F). Seven gabbroic samples were collected, with primary minerals preserved in most samples. South of the Anvil Pluton, gabbroic samples MC-40 and MC-41 are altered with complete biotite and chlorite replacement of pyroxene. Plagioclase in these samples exhibits well-defined polysynthetic twinning and sieve textures. Sample MC-42 is olivine-rich with serpentine alteration of olivine and is most likely a peridotite.

The basaltic samples represent effusive volcanic eruptions. Many of these samples are from pillow basalt outcrops, formed through subaqueous volcanic eruptions. Lapilli tuffs containing angular glass shards likely represent phreatomagmatic eruptions.

MacMillan Pass District

Volcanic rock samples from MacMillan Pass District are almost all volcaniclastic. Ash-rich tuffs, pumice-rich and heterolithic lapilli tuffs are common (Fig. 5A-F). Intense calcite and ankerite alteration of the matrix is common, as is calcite and ankerite replacement of phenocrysts. One tuff contains ‘christmas tree’ dendritic morphologies of an unknown opaque mineral, similar to spinifex textures in komatiites. Heterolithic breccias contain clasts of chert, quartz, pumice, basalt and rare black shale in an ash or carbonate (typically calcite or ankerite) matrix (Fig. 5F). Basalt-like clasts contain a fine-grained groundmass with skeletal plagioclase phenocrysts. Pumice clasts are highly vesicular and show little to moderate flattening/welding (Fig. 5A). Undeformed vesicles are present in pumice clasts and have been filled by multiple generations of calcium or ankeritic carbonate, chalcedony and chlorite. Clasts in different samples vary from those that have irregular angular boundaries reflecting little reworking and those that exhibit sub-rounded boundaries. The majority of the breccias are poorly sorted with clasts varying from sub-mm to tens of cm in diameter. Calcite and ankerite occur in varying proportions in breccias. In some, either carbonate makes up part or all of the matrix and replaces phenocrysts within clasts. The carbonate matrix is commonly composed of coarse calcite or ankerite with prominent twinning (Fig. 5B, D). In several samples the carbonate alteration is so extensive that the clasts are difficult to distinguish from the matrix. One lapilli tuff (MP-13) contains xenocrysts of olivine partially altered to talc and carbonate. Lapilli tuffs tend to have rare to no lithic clasts. Glass shards in lapilli tuffs have cuspate margins (Fig. 5C). Sample MP-18 is a scoria with spherical skeletal olivine grains in a fine-grained groundmass, many of which have been replaced by carbonate.

Sample MP-34 differs from other MacMillan Pass samples in that the alteration is dominantly chlorite rather than ankerite or calcite. Sample MP-36 contains both chlorite and ankerite alteration, with a network of coarse calcite veins between clasts. These samples contain lithic clasts, dominantly chert. These samples represent a small sample suite from one of the MacMillan Pass field sites.

A small number of intrusive samples were collected from the MacMillan Pass region. Sample MP-15 is a coarsely crystalline sample with alteration of primary minerals by carbonate

and/or muscovite. Several primary minerals are still present (Fig. 5E) Euhedral biotite that appears to represent new mineral growth is common throughout the sample. MP-44 is a gabbro with primary olivine, clinopyroxene and plagioclase, and minor serpentine alteration of olivine.

The large size and angularity of volcaniclastic fragments and absence of effusive volcanic rocks indicates that volcanism in the MacMillan Pass area was explosive in nature. Ash-rich tuffs with little to no lapilli are indicative of air fall or surge deposits that are distal from the volcanic vent. The volcanic breccias may represent deposition closer to the site of eruption. More detailed study of the volcanic textures at a finer scale is required to fully understand the style of eruptive activity.

Keno Hill District

There are two igneous suites in the Keno Hill-Mayo region: metavolcanic rocks in the Devonian Earn Group and Triassic mafic dikes. The grade of metamorphism varies in collected samples from the Earn Group. Two lapilli tuffs still display original textures, with relict ash-rich and quartz clasts. There is minor recrystallisation of the ash-rich clasts and matrix, but no deformation. Welded pumice clasts are present in one of the samples with epidote and muscovite in the matrix. Metavolcanic sample EG-09 displays weak mineral alignment in the chlorite and epidote segregations (Fig. 6A). Quartz ± feldspar is also present. Sample EG-19 is also a metavolcanic sample that has undergone higher grade metamorphism than sample EG-09. Mineral layers are segregated and the minerals in the micaceous segregations (chlorite and muscovite with prehnite) are aligned in the same orientation as the mineral segregations (Fig. 6B). Well defined crenulation cleavages are present in these segregations (Fig. 6C). Quartz displays bulging recrystallisation, indicating temperatures of 250-400°C (Stipp et al. 2002). This temperature range is consistent with the mineral assemblage (chlorite, muscovite) that indicates lower greenschist facies metamorphism of this sample.

Triassic dikes crosscut the Earn Group samples. Samples of these dikes show minor chloritic alteration and little deformation. The dikes are composed of primary pyroxene, skeletal olivine, plagioclase and titanite. A weak alignment is present in several samples likely due to regional metamorphic overprinting. Generally, the dikes are basaltic to diabasic in composition (Fig. 6D). One sample is gabbroic with coarse clinopyroxene, olivine and plagioclase.

We are unable to ascertain eruptive styles in the Keno Hill area because metamorphism has obscured primary features of the volcanic rocks.

Misty Creek Embayment

Samples from the Misty Creek Embayment were obtained from the collections of Wayne Goodfellow and Christopher Dean Leslie's Master's thesis (Leslie, 2009) and reanalysed to provide a broader understanding of magmatism within the Selwyn Basin. Crystal-rich and -poor lapilli tuffs are present, with basaltic clasts and large polycrystalline calcite clasts or infilled vesicles. The majority of the samples are basalts with olivine, pyroxene and plagioclase phenocrysts. In some of these basalts the phenocrysts have been partially to completely altered by chlorite and/or chalcedony. One sample has a vein of sulfides (1501D). These samples represent mostly effusive eruptive activity.

LITHOGEOCHEMICAL COMPOSITIONS

Due to the pervasive hydrothermal alteration and surface weathering present in a large number of samples, typical volcanic classification diagrams, such as the TAS diagram (Le Maitre et al., 2002) are not suitable for sample classification in this study. The Zr/Ti vs. Nb/Y plot (Winchester and Floyd, 1977) provides a more robust identification of rock type due to the typically lower mobility of these elements during surface weathering, hydrothermal alteration and metamorphism. MacMillan Pass and Misty Creek samples show significant overlap, both plotting as mostly basanites and alkali basalts (Fig. 7A). Anvil District samples plot as alkali basalts and trachy-andesites whereas Keno Hill samples are less alkalic, plotting as subalkalic basalts and andesites (Fig. 7A). Samples from Anvil, MacMillan Pass and Misty Creek plot as alkaline, within-plate basalts on a Hf/3-Th-Ta diagram (Wood, 1980) (Fig. 7B). Keno Hill Triassic dikes plot as within-plate tholeiites whereas Earn Group samples plot as within-plate tholeiites and calc-alkaline basalts. Spidergram plots highlight the difference in the Keno Hill samples, with the Triassic dikes displaying a distinctly different geochemical signature compared to the metavolcanic samples from within the Earn Group, with no Ti or Sr depletion and a significantly smaller Pb enrichment (Fig. 8A-E). The majority of samples show positive peaks in Ba with depletions in K, Sr, Ti, and Rb (Fig. 8A-E). Pb is commonly depleted in all but the Earn Group samples. The elements Ba, K and Sr are all large ion lithophile elements (LILE) and so we would expect similar geochemical behaviour. The relative depletion and enrichment of these elements indicates the removal (and/or addition) of certain elements mostly likely due to hydrothermal alteration.

Harker diagrams of SiO_2 vs. TiO_2 and $Fe_2O_3^t$ both show an inflection from a positive to a negative slope that occurs at SiO^2 values of ~40 and 50 wt.%, respectively (Fig. 9A, F). This may be due to the addition of silica through quartz veining and chalcedony replacement in the silica-rich samples. The alkalis (Na_2O and K_2O) both do not display clear trends, particularly K_2O. This is likely due to depletion of alkalis during hydrothermal alteration. (Fig. 9B, D). Due to mass balance, CaO decreases as SiO_2 increases (Fig. 9C). Many of these samples contain high CaO abundances (20-40 wt.%) due to the carbonate alteration. MgO decreases as SiO_2 increases in all samples except for MacMillan Pass, where a subset of these samples displays positive trends between MgO and SiO_2 (Fig. 9E). This may be because of MgO in the carbonate or heterolithic clasts within the breccias. SiO_2 displays a positive trend with Al_2O_3, that then inflects for Misty Creek and MacMillan Pass samples as SiO_2 increases past 60 wt.% (Fig. 9G) This may occur due to the addition of silica through alteration such as described earlier.

TiO_2 shows a positive trend with Zr, with the Keno Hill samples containing low abundances of TiO_2. One outlier from MacMillan Pass displays high TiO2 abundances (Fig. 10A). This sample is a volcaniclastic breccia with scoria clasts. Four MacMillan Pass samples show high Zr contents. These samples are all breccias and the high Zr likely reflects the presence of chert and sandstone clasts. Aluminium oxide shows a similar trend when plotted against TiO_2 (Fig. 10B). Barium displays a positive trend with Tl (Fig. 11).

Lead isotopes were measured for all samples. Both $^{207}Pb/^{204}Pb$ and $^{208}Pb/^{204}Pb$ show strong positive correlations with $^{206}Pb/^{204}Pb$ (Fig. 12A-B). The linear function shows the ingrowth of radiogenic lead since the Paleozoic and the variation of U-Th/Pb ratios within the samples. These values will undergo further investigation and samples will be reanalysed using the multi-collector ICP-MS at Queen's University to collect more precise Pb isotope ratios. The Ishikawa alteration index plotted against chlorite-carbonate-pyrite index (CCPI) shows a large proportion of samples have been hydrothermally altered, particularly the Anvil District samples, with surface weathering dominant in many of the MacMillan Pass samples (Fig. 13). A large proportion of Anvil District samples occur within the least-altered basalt box, reflecting the minimal alteration evident in both hand sample and thin section.

AGE DATING

One sample (EG-18) from Keno Hill (Earn Group) was dated using chemical abrasion thermal ionisation mass spectrometry (TIMS) at Boise State University. Zircon grains give an age of 296.58 ± 0.11 Ma (MSWD = 1.5).

Initial scanning electron microscopy work has been utilised to identify minerals that can be age dated, in particular zircon, monazite and apatite. Epoxy mounts of heavy mineral fractions and polished thin sections were both analysed.

No zircons were identified in the grain mounts of Anvil District samples MC-15, MC-39 and MC-41. However, small (< 10 µm) zircons are abundant in Anvil District samples MC-11, MC-13 and MC-14. Apatite was identified in all the grain mounts from the Anvil District, occurring as polycrystalline mineral clusters where the grains were not fully separated upon crushing and separation at ODM (Fig. 14A). Apatite in these grain mounts are commonly 50-200 µm and suitable for LA-ICP-MS dating.

Zircon grains were identified within MacMillan Pass samples MP-03, MP-12, MP-14, MP-26, MP-27, and MP-33. Grainsize of zircons vary from < 5 µm to 50 µm. Zoned zircons were identified in sample MP-27 and MP-33, both of which also contain unzoned zircons (Fig. 14B-D).

All Keno Hill Earn Group samples analysed (EG-01, EG-09, EG-17 and EG-19) contain zircons ranging up to 50 µm (Fig. 14E). Monazite is present in sample EG-17 (Fig. 14F).

The one date from the Keno Hill Earn Group of 296.58 ± 0.11 Ma falls within the Early Permian, which is younger than expected as the Earn Group is Devonian-Mississippian (Abbott, 1982). This suggests that this sample is not from the Earn Group as initially considered and may represent either a younger unit or intrusion. Further geochronology is required to establish more precise age constraints of volcanism in the Selwyn Basin and whether these volcanic rocks could contribute to the formation of Pb-Zn sediment-hosted mineralisation.

THALLIUM ISOTOPES

Six samples from MacMillan Pass give a $\varepsilon^{205}Tl$ range of –3.2 ± 1.8 to –14.2 ± 3.2 (Table 1). The negative value of –14.2 is much lower than the next lowest value of –9.5 ± 2.5 and has a larger error, skewing the range of the MacMillan Pass samples. Five samples from the Anvil District have a $\varepsilon^{205}Tl$ range of –0.9 ± 1.9 to –6.4 ± 1.2. Even accounting for the anomalous sample from MacMillan Pass, the sample suite displays more negative values than that of the Anvil District. There is no apparent correlation of Tl isotopic composition and Tl abundance. This is likely due to the low Tl contents, which have large errors associated with those values (Fig. 15A). There is a negative correlation between $\varepsilon^{205}Tl$ and Ba content (Fig. 15B). The volcanic rocks from the Anvil District show overlap in $\varepsilon^{205}Tl$ with the mineralised rocks at Howard's Pass, a variety of volcanic rocks, black smoker fluids and altered oceanic crust (Fig. 16) (Kersten et al., 2014 and references therein; Peter et al., 2018). Values of volcanic rocks from MacMillan Pass show limited overlap, coinciding with unmineralised rocks at Howard's Pass and altered oceanic crust, which has a large $\varepsilon^{205}Tl$ range. All of the MacMillan Pass samples have lighter isotopic values than average continental crust, which has $\varepsilon^{205}Tl \sim -2$ (Nielsen et al., 2016). The MacMillan Pass samples typically show more hydrothermal alteration than the samples from the Anvil District, with complete replacement of the matrix in all volcaniclastic breccias. The lighter isotope values in the MacMillan Pass samples compared to the Anvil District may represent this pervasive alteration. It is unlikely that the lightest values represent clasts of country rock within the volcaniclastic breccias as the measured sedimentary rocks in the region have heavier $\varepsilon^{205}Tl$ isotopic values of ~ –8 to –4 (Peter et al., 2018). The light isotope signature is similar to volcanics from Central America (Nielsen et al., 2017). The lighter Tl signatures have been interpreted to reflect incorporation of altered oceanic crust into the melt (Nielsen et al., 2017). The abundances of Tl within the samples are low (< 2 ppm) and so any contamination of the Tl signature of the igneous rocks would be evident. Lower Tl contents may result from the removal of Tl during hydrothermal alteration. Thallium behaves like an alkali metal and depletion in K and Rb are evident (Fig. 8A-B), suggesting that the low Tl is due to alteration. This indicates that low temperature hydrothermal alteration has affected the Tl abundance and likely the Tl isotopic signature. Thus, our current hypothesis is that the lighter isotopic values from MacMillan Pass reflect low temperature alteration, and this premise will be further investigated using a larger sample set.

PRELIMINARY CONCLUSIONS

The eruptive styles and geochemistry of volcanism in the Selwyn Basin was variable throughout the Paleozoic. Samples from the four studied geographical areas are all distinct in either in their lithogeochemical composition or eruptive styles. Earn Group volcanics from the Keno Hill District are particularly distinct as the only studied samples that are of sub-alkaline affinity. The orange weathering of the MacMillan Pass volcanics is visually distinctive, due to the presence of ankeritic carbonate comprising up to 70 wt.% in several samples. Within the Anvil District, samples are less altered than samples from MacMillan Pass, and fall into two categories: 1) basaltic and pillow flows and 2) breccias and tuffs.

The volcaniclastic nature and petrographic textures of samples from MacMillan Pass suggest that volcanic eruptions in this area were explosive. Volcanic rocks from the Anvil District display either phreatomagmatic or subaqueous effusive eruptive characteristics.

Lithogeochemical analyses confirm the alkaline nature of magmatic rocks in MacMillan Pass, Anvil District and the Misty Creek Embayment. These samples all reflect within-plate volcanism. Keno Hill Triassic dikes are subalkaline within-plate tholeiites, whereas the Keno Hill Earn Group samples vary from within-plate tholeiites to calc-alkaline affinity. Samples are enriched in Ba and show depletion in K, Rb and Sr with variable enrichment or depletion in Pb and Ti, most likely reflecting hydrothermal alteration. Ba and Tl show a positive correlation and suggesting these elements are enriched in the volcanic rocks through a similar process.

Thallium isotope compositions of volcanic samples from MacMillan Pass and Anvil District show a wide range between and within the two sample sets from –0. 9 ± 1.9 and –14. 2 ± 3.2. MacMillan Pass samples tend to have more negative values, which may represent low temperature hydrothermal alteration. Compared to values from host rock and mineralised samples at Howard's Pass (Peter et al., 2018), the Anvil District samples completely overlap, whereas the MacMillan Pass samples partially overlap, suggesting that the Anvil District system shares isotopic similarities with the Howard's Pass region. Comparison with mineralised samples from each of the two areas and a larger sample size is required to provide meaningful interpretations.

FUTURE WORK

Tl and Mo Isotopes

A further 20-30 volcanic samples will be analysed for Tl and Mo isotopes to provide a robust sample set and investigate the observed range of isotopic values in the small sample set. Mineralised samples and background unmineralised shales from the Anvil District and MacMillan Pass will be analysed and compared to the volcanic samples.

Nd, Sr and Pb Isotopes

To provide an in-depth characterisation of magmatism in the Selwyn Basin, Nd, Sr and Pb isotopes will be used to identify magma sources and the style(s) of alteration. Sixty samples from across the Selwyn Basin will be analysed initially. Depending upon the results, 20 more samples will potentially be analysed. Sample digestions and initial chromatographic separations have been initiated.

Age dating

Six samples are currently being dated using thermal ionisation mass spectrometry (TIMS) U-Th-Pb dating of zircons at Boise State University. These samples are from Keno Hill (2), MacMillan Pass (3) and one sample from the Anvil District. Samples from all three areas will also be dated at Queen's University Facility for Isotope Research using LA-ICP-MS. These samples have already been characterised earlier in this report and are currently being prepared for laser ablation U-Th-Pb dating of zircon, monazite and apatite within epoxy mounts of these samples.

ACKNOWLEDGEMENTS

This report was prepared for the National Resources Canada Targeted Geoscience Initiative Program (TGI). Funding was provided under the project 'Volcanic- and Sedimentary-Hosted Base Metal Mineralization: Activity VS-2.2: Magmatism and Relationships to Sediment-Hosted Zn-Pb Deposits'. We would like to thank Agatha Dobosz for her assistance with MLA-SEM and Don Lougheed for help creating epoxy grain mounts. We thank Jan Peter for his thorough and extensive review and editing of this report.

REFERENCES

Abbott, G.
1982: Structure and stratigraphy of the MacMillan Fold Belt: evidence for Devonian faulting; Open File Report, Exploration and Geological Services Division, Department of Indian Affairs and Northern Development, Whitehorse, Yukon, 16 p.

Dusel-Bacon, C., Lanphere, M.A., Sharp, W.D., Layer, P.W. and Hansen, W.L.
2002: Mesozoic thermal history and timing of structural events for the Yukon-Tanana upland, east-central Alaska: 40Ar/39Ar data from metamorphic and plutonic rocks; Canadian Journal of Earth Sciences, v. 39, p. 1013–1051

Cecile, M.P., Fritz, W.H., Norford, B.S. and Tipnis, R.S.
1982: The Lower Paleozoic Misty Creek Embayment, Selwyn Basin, Yukon and Northwest Territories. Bulletin 335: Geological Survey of Canada, 78 p.

Fandrich, R., Gu, Y., Burrows, D. and Moeller, K.
2007: Modern SEM-based mineral liberation analysis; International Journal of Mineral Processing, 84(1-4), pp.310-320.

Gadd, M.G., Layton-Matthews, D., Peter, J.M. and Paradis, S.J.
2016: The world-class Howard's Pass SEDEX Zn-Pb district, Selwyn Basin, Yukon. Part I: trace element compositions of pyrite record input of hydrothermal, diagenetic, and metamorphic fluids to mineralization; Mineralium Deposita, v. 51, p. 319-342.

Goodfellow, W.D., Cecile, M.P. and Leybourne, M.I.
1995: Geochemistry, petrogenesis, and tectonic setting of lower Paleozoic alkalic and potassic volcanic rocks, northern Canadian Cordilleran Miogeocline; Canadian Journal of Earth Sciences, v. 32, p. 1236-1254.

Goodfellow, W.D.
2004: Geology, genesis and exploration of SEDEX deposits, with emphasis on the Selwyn Basin, Canada; in Sediment-Hosted Lead-Zinc Sulphide Deposits: Attributes and Models of Some Major Deposits in India, Australia and Canada, (ed.) Deb., M and Goodfellow, W.D; Narosa Publishing House, New Delhi, p.24-99.

Goodfellow, W.D. and Lydon, J.W.
2007: Sedimentary exhalative (SEDEX) deposits. in Mineral deposits of Canada: A synthesis of major deposit types, district metallogeny, the evolution of geological provinces, and exploration methods (ed.) Goodfellow, W.D.; Geological Association of Canada, Mineral Deposits Division, Special Publication, 5, pp.163-183.

Gordey, S.P., Abbott, J.G., and Orchard, M.J.
1982: Devono-Mississippian Earn Group and younger strata in east-central Yukon; Geological Survey of Canada Paper 82-IB, p. 93-100.

Jennings, D.S. and Jilson, G.A.
1986: Geology and sulphide deposits of the Anvil Range, Yukon; in Mineral Deposits of Northern Cordillera, (ed.) J.A. Morin, J.A.; Canadian Institute Mining and Metallurgy, p. 339-361.

Kelley, K.D., Leach, D.L., Johnson, C.A., Clark, J.L., Fayek, M., Slack, J.F., Anderson, V.M., Ayuso, R.A. and Ridley, W.I.
2004: Textural, compositional, and sulfur isotope variations of sulfide minerals in the Red Dog Zn-Pb-Ag deposits, Brooks Range, Alaska: Implications for ore formation; Economic Geology, v. 99, p. 1509-1532.

Kersten, M., Xiao, T., Kreissig, K., Brett, A., Coles, B.J. and Rehkämper, M.
2014: Tracing anthropogenic thallium in soil using stable isotope compositions; Environmental Science and Technology, v. 48, p. 9030-9036.

Kirkham, G., Dunning, J., and Schleiss, W.
2012: Update for Don deposit mineral resource estimate, Howard's Pass property, eastern Yukon; Selwyn Resources Ltd., NI 43-101 Technical Report, 145 p.

Koski, R.A., Lonsdale, P.F., Shanks, W.C., Berndt, M.E. and Howe, S.S.
1985: Mineralogy and geochemistry of a sediment-hosted hydrothermal sulfide deposit from the Southern Trough of Guaymas Basin, Gulf of California; Journal of Geophysical Research: B: Solid Earth, v. 90, p. 6695-6707.

Large, R.R., Gemmell, J.B., Paulick, H. and Huston, D.L.
2001: The alteration box plot: A simple approach to understanding the relationship between alteration mineralogy and lithogeochemistry associated with volcanic-hosted massive sulfide deposits; Economic Geology, v. 96, p. 957-971.

Large, R. R., McPhie, J., Gemmell, J. B., Herrmann, W., and Davidson, G. J.
2001: The spectrum of ore deposit types, volcanic environments, alteration halos, and related exploration vectors in submarine volcanic successions: Some examples from Australia; Economic Geology, v. 96, p. 913-938.

Leach, D.L., Bradley, D.C., Huston, D., Pisarevsky, S.A., Taylor, R.D., and Gardoll, S.J.
2010.: Sediment-hosted lead-zinc deposits in Earth history; Economic Geology, v. 105, p. 593-625.

Le Maitre, R.W., Streckeisen, A., Zanettin, B., Le Bas, M.J., Bonin, B. and Bateman, P. eds.
2005: Igneous rocks: a classification and glossary of terms: recommendations of the International Union of Geological Sciences Subcommission on the Systematics of Igneous Rocks. Cambridge University Press.

Leslie, C.D.
2009: Detrital zircon geochronology and rift-related magmatism: Central Mackenzie Mountains, Northwest Territories; PhD Thesis, University of British Columbia, Vancouver, British Columbia, 224 p.

Leybourne, M.I., Van Wagoner, N., Paradis, S., Layton-Matthews, D., and Moertle, J.A.
2018: Selwyn Basin magmatism and relationship to sediment-hosted Zn- Pb deposits. in Targeted Geoscience Initiative: 2017 report of activities, volume 2, (ed.) N. Rogers; Geological Survey of Canada, Open File 8373, p. 71–92.

Lydon, J.W.
1983: Chemical parameters controlling the origin and deposition of sediment-hosted stratiform lead-zinc deposits. in Short course in sediment-hosted stratiform lead-zinc deposits. (ed.) D.F. Sangster; Mineralogical Association of Canada, v. 9, p. 175-250

Magnall, J.M., Gleeson, S.A., Blamey, N.J.F., Paradis, S. and Luo, Y.
2016: The thermal and chemical evolution of hydrothermal vent fluids in shale hosted massive sulphide (SHMS) systems from the MacMillan Pass district (Yukon, Canada); Geochimica et Cosmochimica Acta, v. 193, p. 251-273.

Mair, J.L., Hart, C.J. and Stephens, J.R.
2006: Deformation history of the northwestern Selwyn Basin, Yukon, Canada: Implications for orogen evolution and mid-Cretaceous magmatism; Geological Society of America Bulletin, v. 118(3-4), pp.304-323.

McClenaghan, M.B.
2011: Overview of common processing methods for recovery of indicator minerals from sediment and bedrock in mineral exploration; Geochemistry: Exploration, Environment, Analysis, v. 11, p. 265-278.

Nelson, J.O. and Colpron, M.A.
2007: Tectonics and metallogeny of the British Columbia, Yukon and Alaskan Cordillera, 1.8 Ga to the present. in Mineral Deposits of Canada: A Synthesis of Major Deposit-Types, District Metallogeny, the Evolution of Geological Provinces, and Exploration Methods, (ed.) Goodfellow, W.D.; Geological Association of Canada, Mineral Deposits Division, Special Publication 5, p. 755-791.

Nielsen, S. G., Yogodzinski, G., Prytulak, J., Plank, T., Kay, S. M., Kay, R. W., Blusztajn, J., Owens, J. D., Auro, M., and Kading, T.
2016: Tracking along-arc sediment inputs to the Aleutian arc using thallium isotopes; Geochemica et Cosmochimica Acta, v. 181, p. 217-237.

Nielsen, S. G., Prytulak, J., Blusztajn, J., Shu, Y., Auro, M., Regelous, M., and Walker, J.
2017: Thallium isotopes as tracers of recycled materials in subduction zones: review and new data for lavas from Tonga-Kermadec and Central America; Journal of Volcanology and Geothermal Research, v. 339, p. 23-40.

Peter, J.M., Gadd, M.G., Layton-Matthews, D. and Voinot, A.
2017: Reconnaissance thallium isotope study of zinc-lead SEDEX mineralization and host rocks in the Howard's Pass district, Selwyn Basin, Yukon: Potential application to paleoredox determinations and fingerprinting of mineralization. in Targeted Geoscience Initiative: 2017 report of activities, volume 1, (ed.) N. Rogers; Geological Survey of Canada, Open File 8358, p. 179–191.

Shanks, W.C., Woodruff, L.G., Jilson, G.A., Jennings, D.S., Modene, J.S. and Ryan, B.D.
1987: Sulfur and lead isotope studies of stratiform Zn-Pb-Ag deposits, Anvil Range, Yukon; basinal brine exhalation and anoxic bottom-water mixing; Economic Geology, 82(3), pp.600-634.

Stipp, M., Stuènitz, H., Heilbronner, R. and Schmid, S.M.
2002: The eastern Tonale fault zone: a 'natural laboratory' for crystal plastic deformation of quartz over a temperature range from 250 to 700 C; Journal of Structural Geology, v. 24, p. 1861-1884.

Sun, S.S. and McDonough, W.F.
1989: Chemical and isotopic systematics of oceanic basalts: implications for mantle composition and processes. in Magmatism in the Ocean Basins. (ed.) Saunders, A.D., Norry, M.J.; Geological Society, London, Special Publications, v. 42, p. 313-345.

Turner, R. J. W. and Rhodes, D.
1990: Boundary Creek zinc deposit (Nidd property), MacMillan Pass, Yukon: sub-seafloor sediment-hosted mineralization associated with volcanism along a late Devonian syndepositional fault. in Current Research, Part E, Geological Survey of Canada, Paper 90-IE, p. 321-335.

Wainman, C.C., McCabe, P.J. and Crowley, J.L.
2018: Solving a tuff problem: Defining a chronostratigraphic framework for Middle to Upper Jurassic nonmarine strata in eastern Australia using uranium–lead chemical abrasion–thermal ionization mass spectrometry zircon dates; AAPG Bulletin, v. 102, p. 1141-1168.

Winchester, J.A. and Floyd, P.A.
1977: Geochemical discrimination of different magma series and their differentiation products using immobile elements; Chemical Geology, v. 20, p. 325-343.

Wood, D.A.
1980: The application of a Th-Hf-Ta diagram to problems of tectonomagmatic classification and to establishing the nature of crustal contamination of basaltic lavas of the British Tertiary Volcanic Province; Earth and Planetary Science Letters, v. 50, p. 11-30.

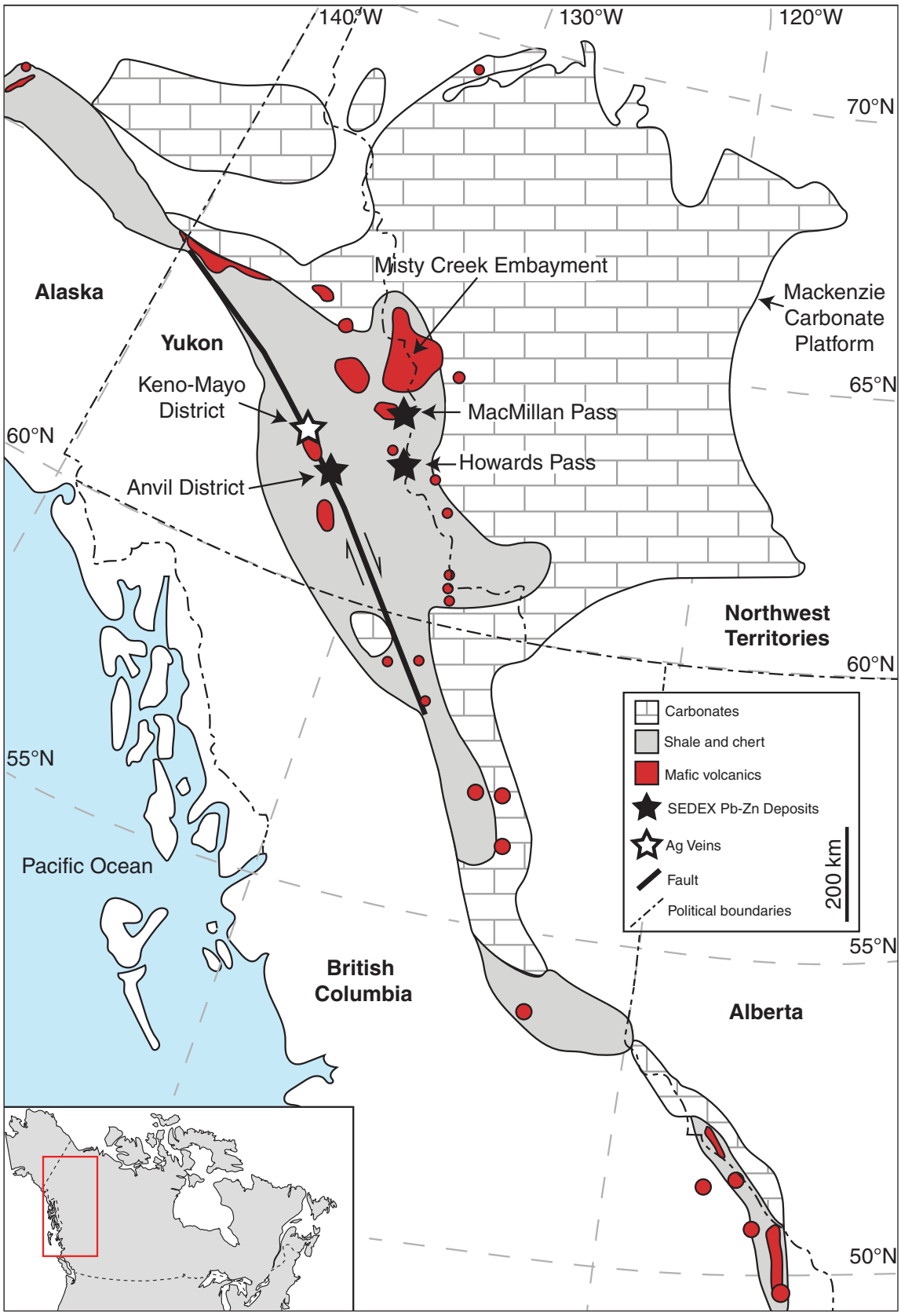

Figure 1. Distribution of mafic volcanic samples in the Selwyn Basin and location of discussed sample regions and Pb-Zn clastic sediment-hosted deposits. Modified from Goodfellow (1995).

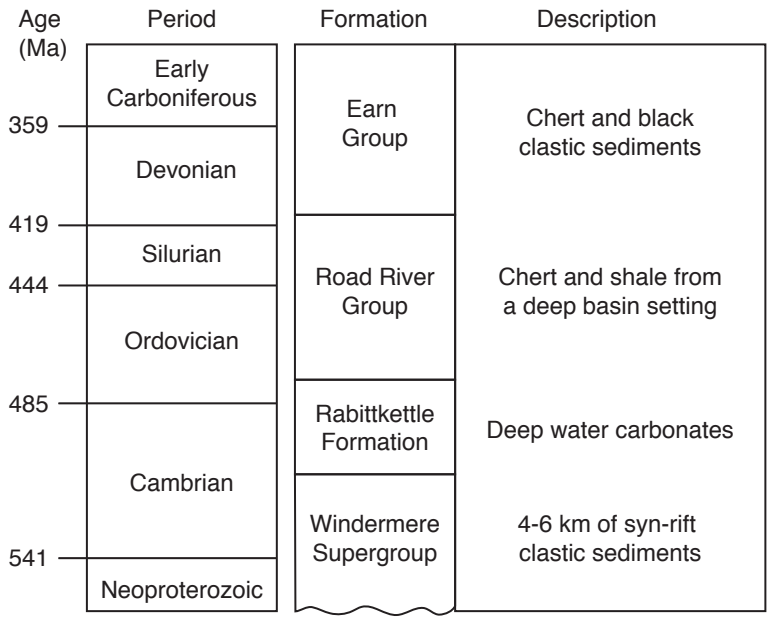

Figure 2. Generalised stratigraphic section of sedimentary units in the Selwyn Basin. Formation descriptions and ages from Gordey et al. (1982), and from Goodfellow (2004).

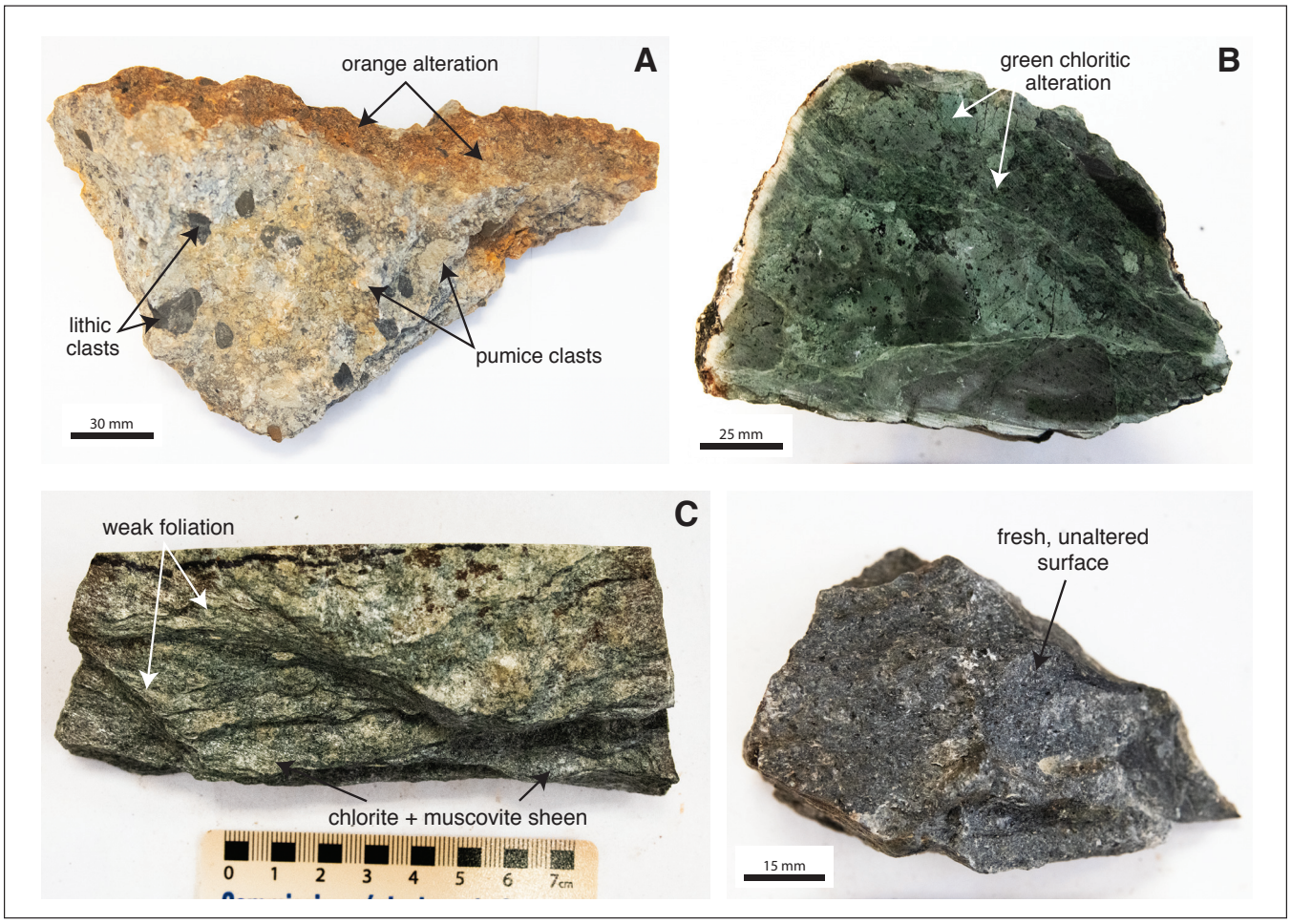

Figure 3. A. Volcaniclastic sample from MacMillan Pass displaying the characteristic orange ferroan carbonate weathering. B. Altered basalt from Anvil District. C. Metavolcanic Earn Group sample from Keno Hill. D. Unaltered Triassic mafic dike from Keno Hill District.

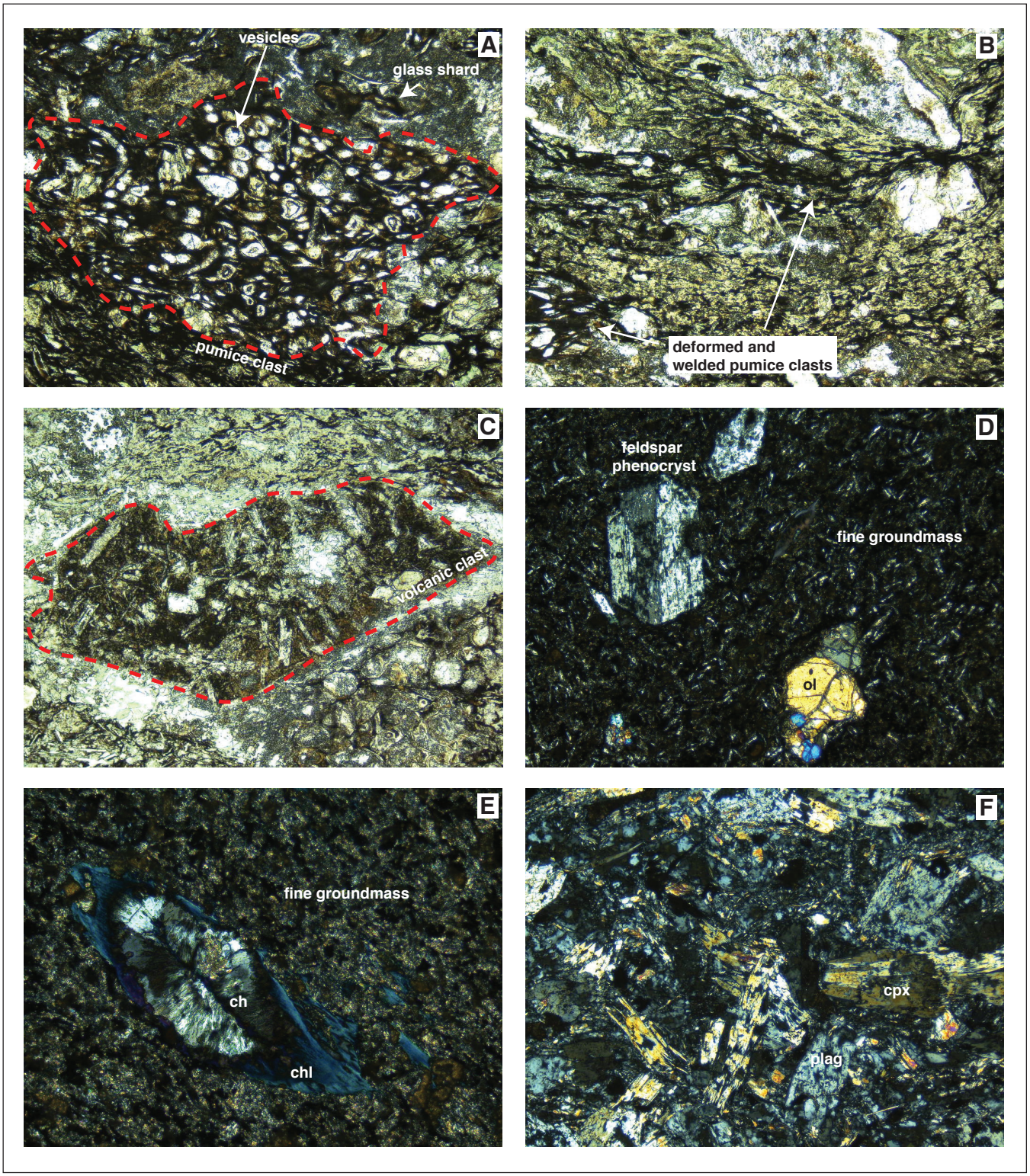

Figure 4. Photomicrographs of volcanic rock samples from the Anvil District. Field of view (FOV) = 3 mm. A. Undeformed pumice clast within lapilli tuff. B. Pumice clasts are variably welded, and more compacted where more competent clasts have contacted the pumice. C. Large volcanic clasts are present in many of the breccias and lapilli tuffs. This sample also has several glass shards present in the bottom right of the photomicrograph. D. Several basalts are relatively unaltered with relict primary phenocrysts. E. Other basalts have primary phenocrysts completely replaced by chlorite and chalcedony. F. Skeletal clinopyroxene and plagioclase occur in one of the gabbros. ol = olivine, ch = chalcedony, chl = chlorite, cpx = clinopyroxene, plag = plagioclase.

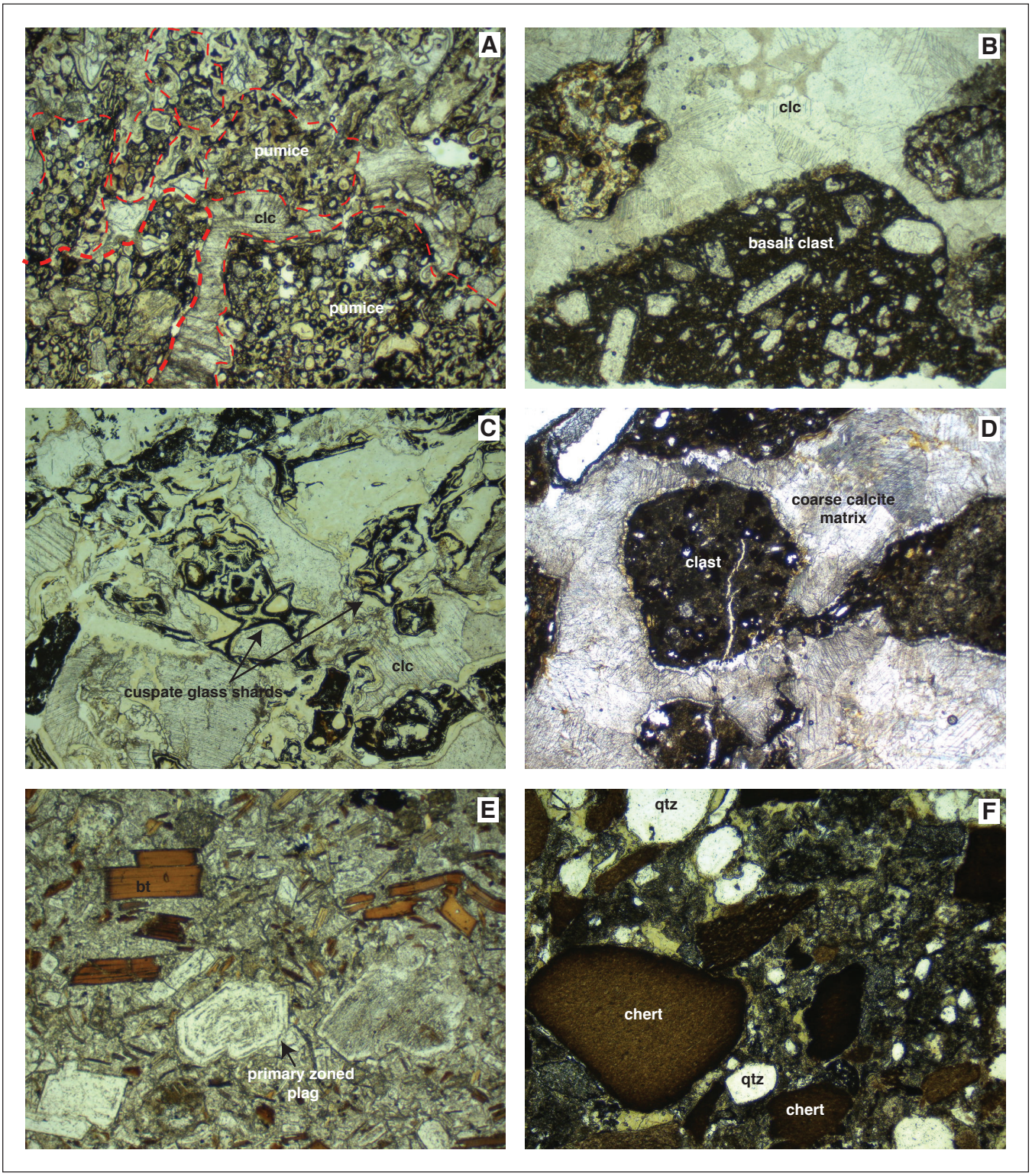

Figure 5. Photomicrographs of MacMillan Pass samples. FOV=3 mm. A. Undeformed pumice clasts in a calcite matrix. B. Basaltic clasts are present in several lapilli tuffs and breccias. C. Glass shards with cuspate margins and vesicles. D. Coarse grained calcite comprises the matrix in many samples. E. Intrusive gabbroic sample with primary grains that are altered or partially replaced by fine grained muscovite. Fresh biotite is present. F. Heterolithic breccia with chert and quartz clasts in a fine-grained matrix. clc = calcite, bt = biotite, plag = plagioclase, qtz = quartz.

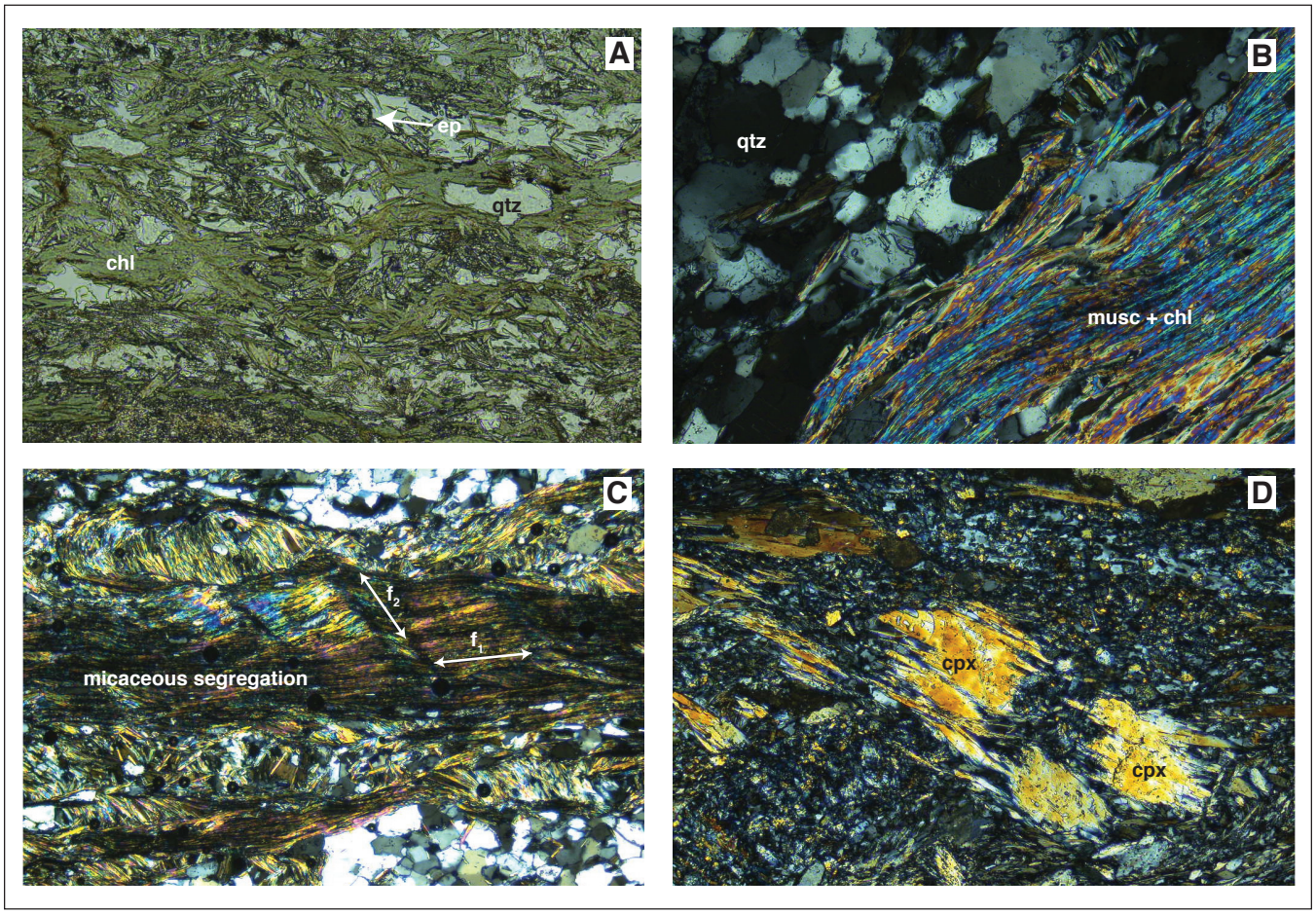

Figure 6. Photomicrographs of Earn Group and Triassic Dikes in Keno Hill region. FOV for A and D = 3 mm. FOV for B and C = 1.5 mm. A. Weakly metamorphosed metavolcanic (EG-09) with poorly segregated chlorite + epidote and quartz layers. B. Well defined micaceous and quartzose segregations in higher grade metavolcanic EG-19. C. Crenulation cleavage in sample EG-19. The first foliation formed in one stress direction (f1) has been overprinted by a second (f2). D. Large clinopyroxene in a dolerite Triassic dike.

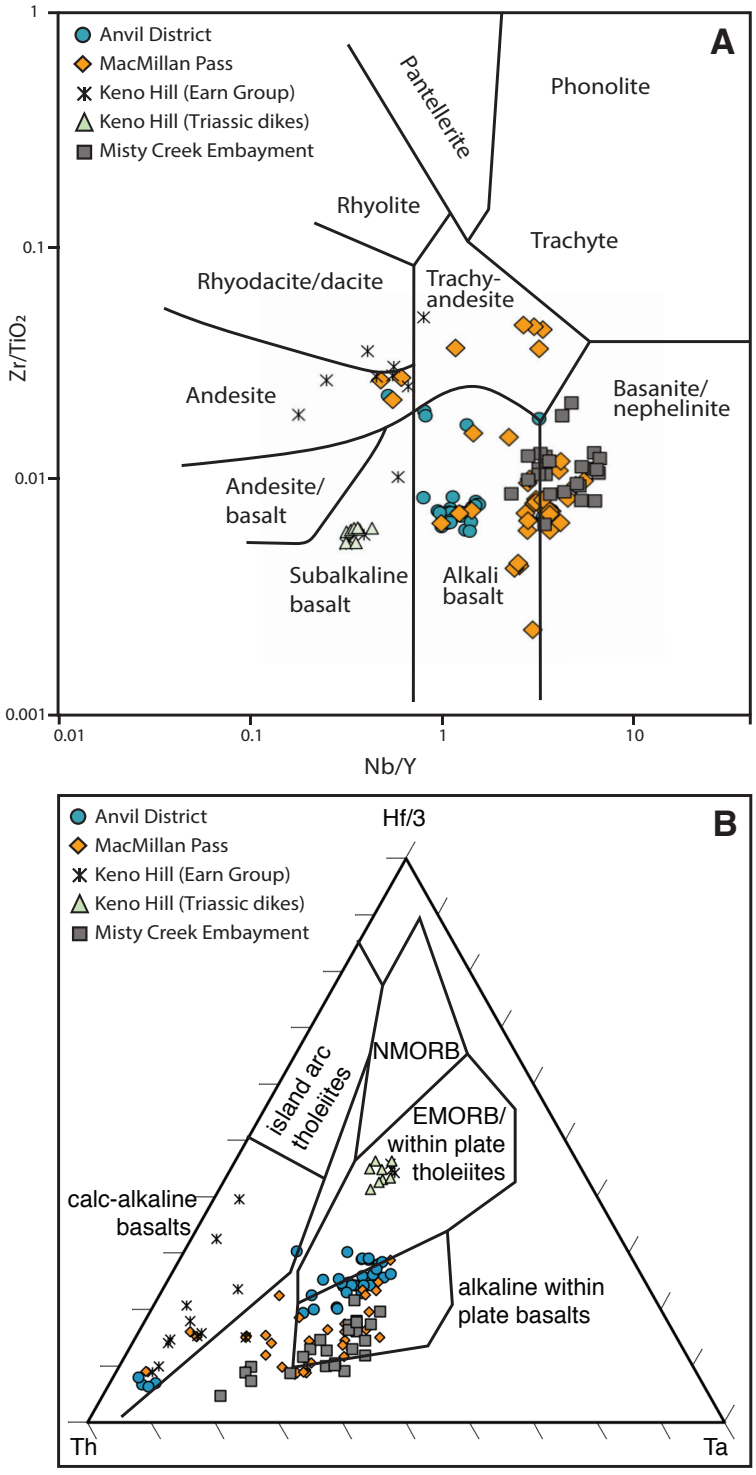

Figure 7. A. Zr/TiO_2 versus Nb/Y discrimination diagram of Winchester and Floyd (1977). Keno Hill and Anvil District samples show little overlap with the basanites of MacMillan Pass and Misty Creek Embayment. B. Ternary Hf/3-Th-Ta tectonic classification diagram of Wood (1980) highlighting the difference between the Keno Hill and other Selwyn Basin magmatic rocks. Nearly all other samples plot as alkaline within-plate basalts.

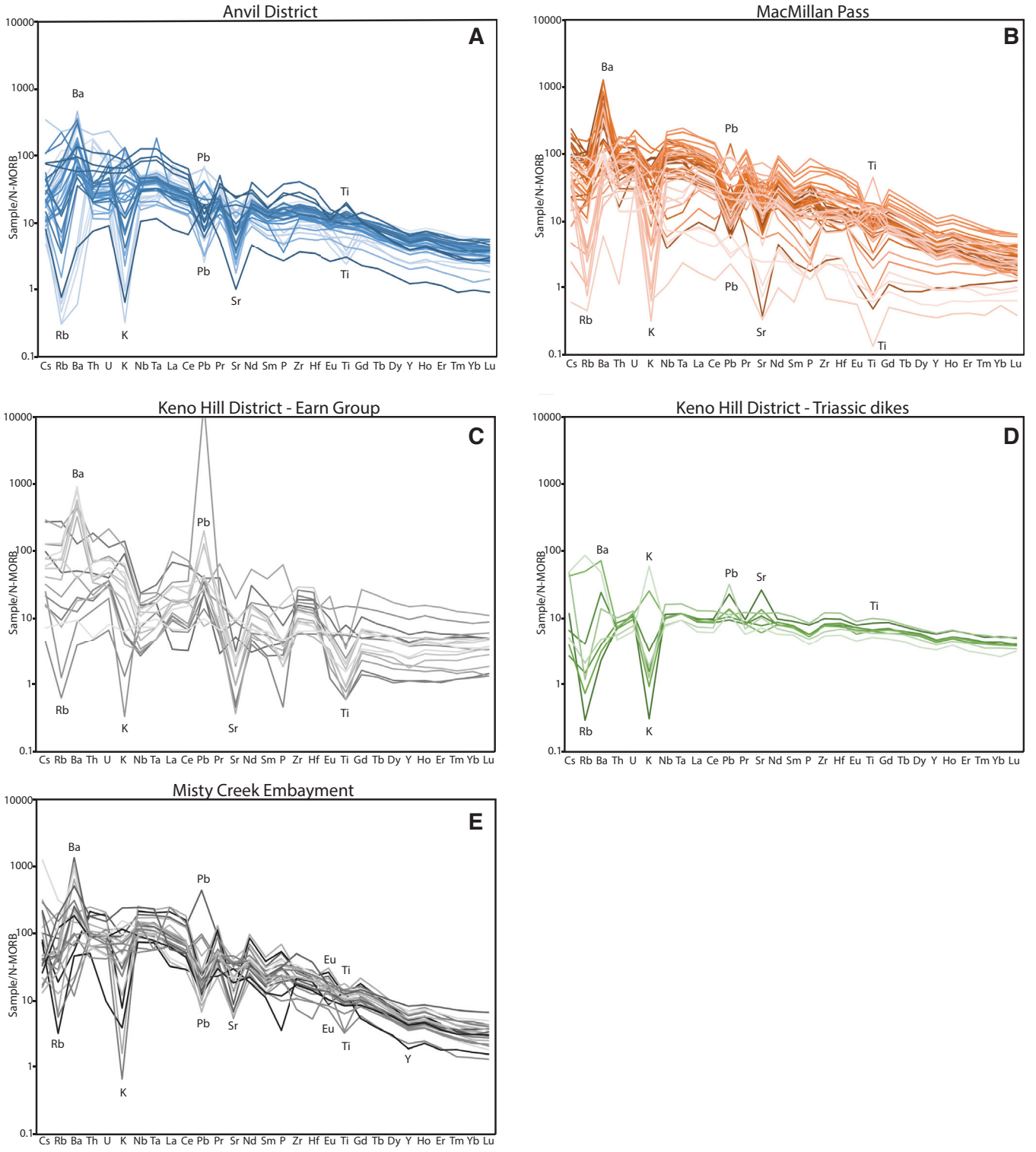

Figure 8. Spider diagrams for each of the five sample suites normalised to N-MORB values of Sun and McDonough (1989). A. Samples from the Anvil District display depletions in Rb and Sr, enrichment in Ba and have variable normalised K, Pb and Ti abundances. B. MacMillan Pass samples show similar trends with a stronger Ba enrichment and an absence of K enrichment. C. Earn Group samples from Keno Hill show prominent negative anomalies in Sr and Ti with one sample displaying a significant positive Pb anomaly. The normalised REE display a flatter pattern in comparison to the negative slopes in Anvil and MacMillan Pass samples. D. The Triassic dikes display Rb and K depletions and small enrichments in Pb and Sr. No Ti anomaly is present. E. Samples from the Misty Creek Embayment show similar trends to those from the Anvil District. However, these samples have small positive and negative anomalies in Eu and Y.

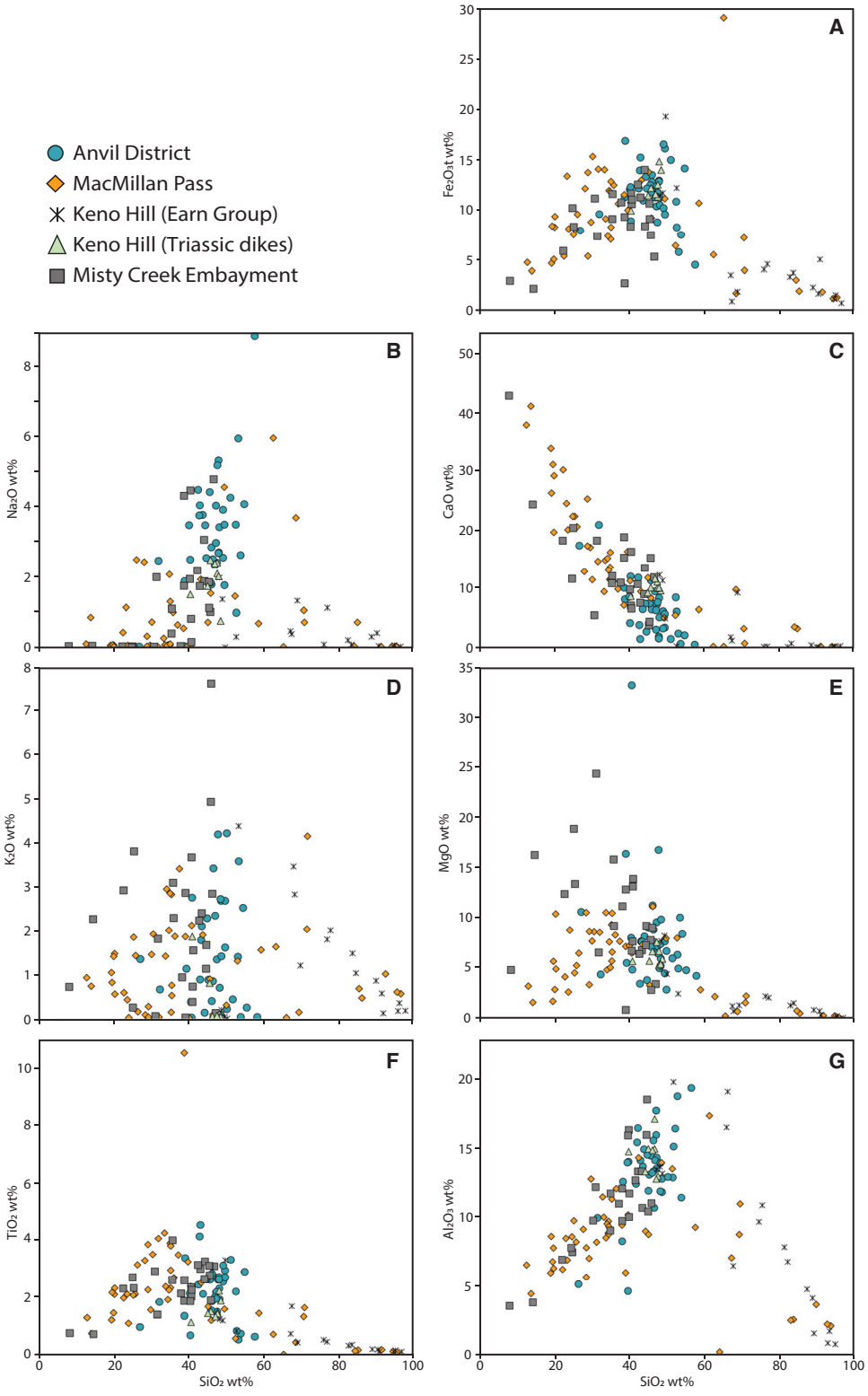

Figure 9. Harker diagrams for major elements of all regions in the Selwyn Basin. The samples with the highest and lowest abundances of SiO2 are intensely altered and/or chert-rich heterolithic breccias. A. Bivariate plot of SiO_2 versus Fe_2O_3 (total). Samples show a positive relationship that inverts at ~50 wt% SiO_2. B. Na_2O does not display a clear trend when plotted against SiO2. C. CaO decreases with increasing SiO_2. D. There is no trend when K_2O is plotted against SiO_2. E. MgO decreases with increasing SiO_2 except for the MacMillan Pass samples, which show a positive relationship between MgO and SiO_2. Several MacMillan Pass and Earn Group samples with SiO_2 values > 60 wt% have little MgO (< 5 wt%). F. TiO_2 increases with SiO_2 to values of approximately 40 wt% where TiO_2 values then decrease with increasing SiO_2. G. Al_2O_3 values increase with SiO_2. From ~60 wt% SiO_2, Al_2O_3 values decrease.

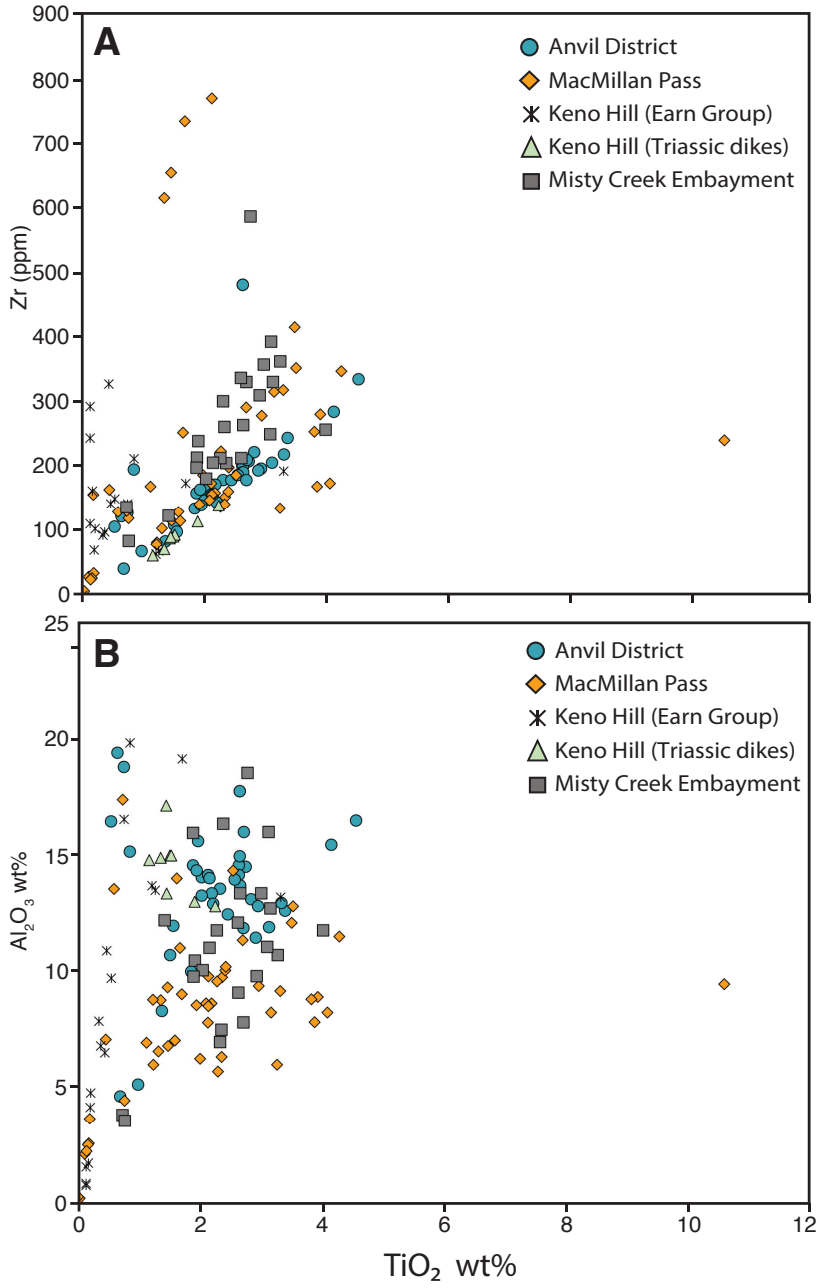

Figure 10. A. TiO_2 versus Zr plot. TiO_2 shows a positive trend against Zr, with the Keno Hill Earn Group samples showing a steep increase of Zr at low TiO_2 concentrations. B. TiO_2 versus Al_2O_3 plot. Al_2O_3 shows a weak positive correlation with TiO_2.

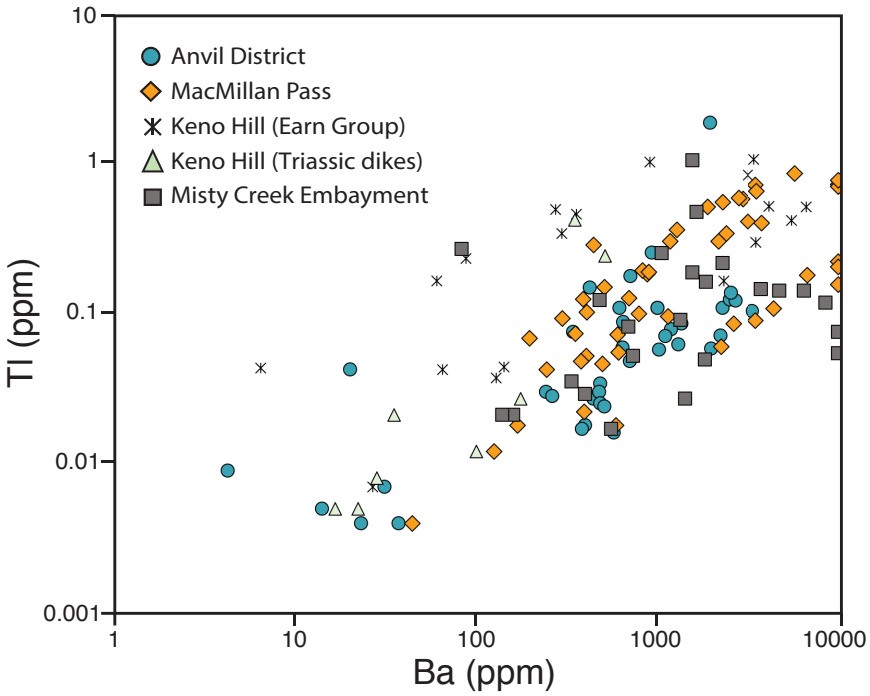

Figure 11. Bivariate plot of Ba versus Tl. Ba occurs in high abundances within the volcanic rocks, with some samples exceeding the upper detection limit of 10 000 ppm. Ba shows a positive correlation with Tl, which is present in very low abundances.

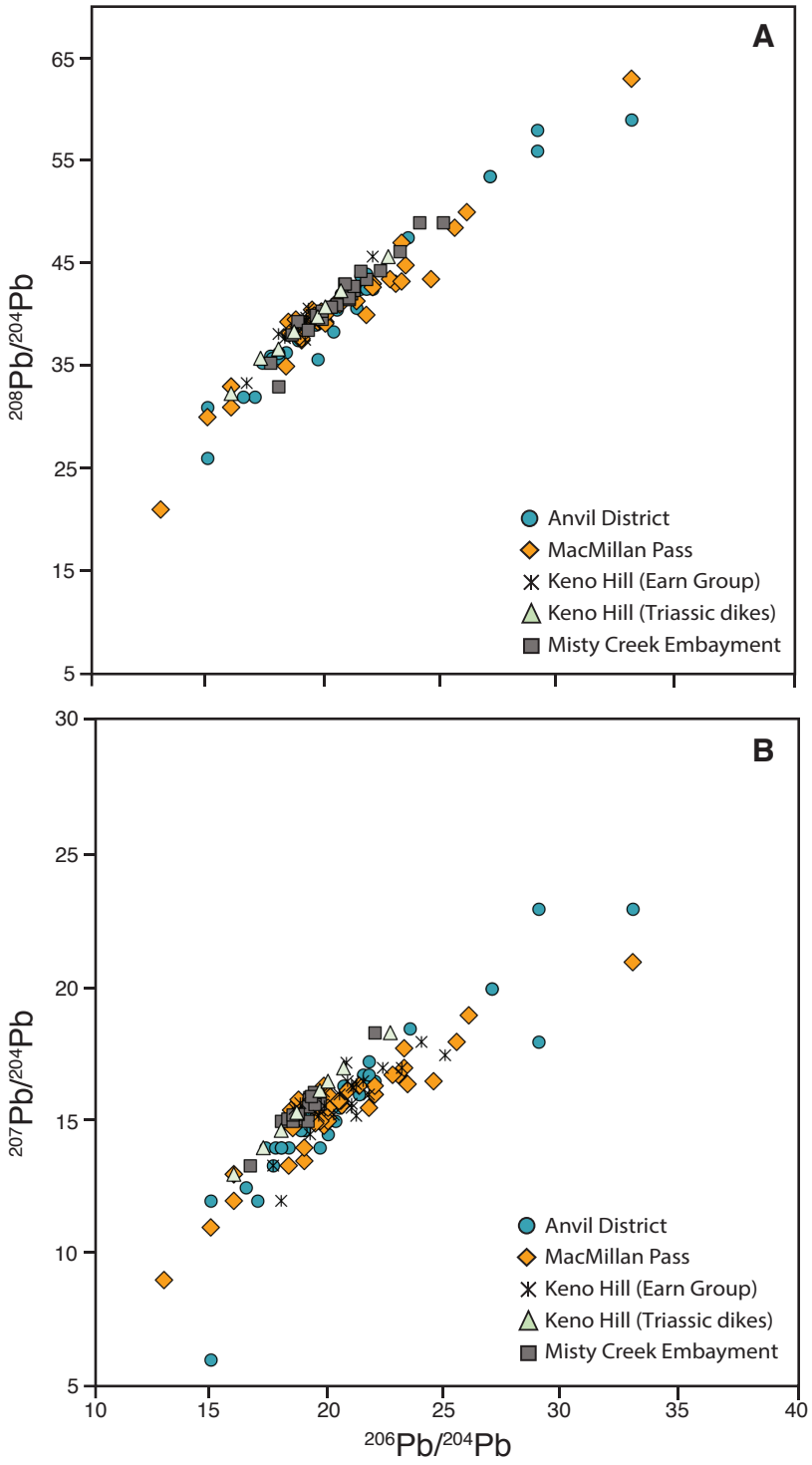

Figure 12. A. $^{206}Pb/^{204}Pb$ versus $^{208}Pb/^{204}Pb$ plot; B. $^{206}Pb/^{204}Pb$ versus $^{207}Pb/^{204}Pb$ plot. Both $^{207}Pb/^{204}Pb$ and $^{208}Pb/^{204}Pb$ show a strong positive correlation with $^{206}Pb/^{204}Pb$.

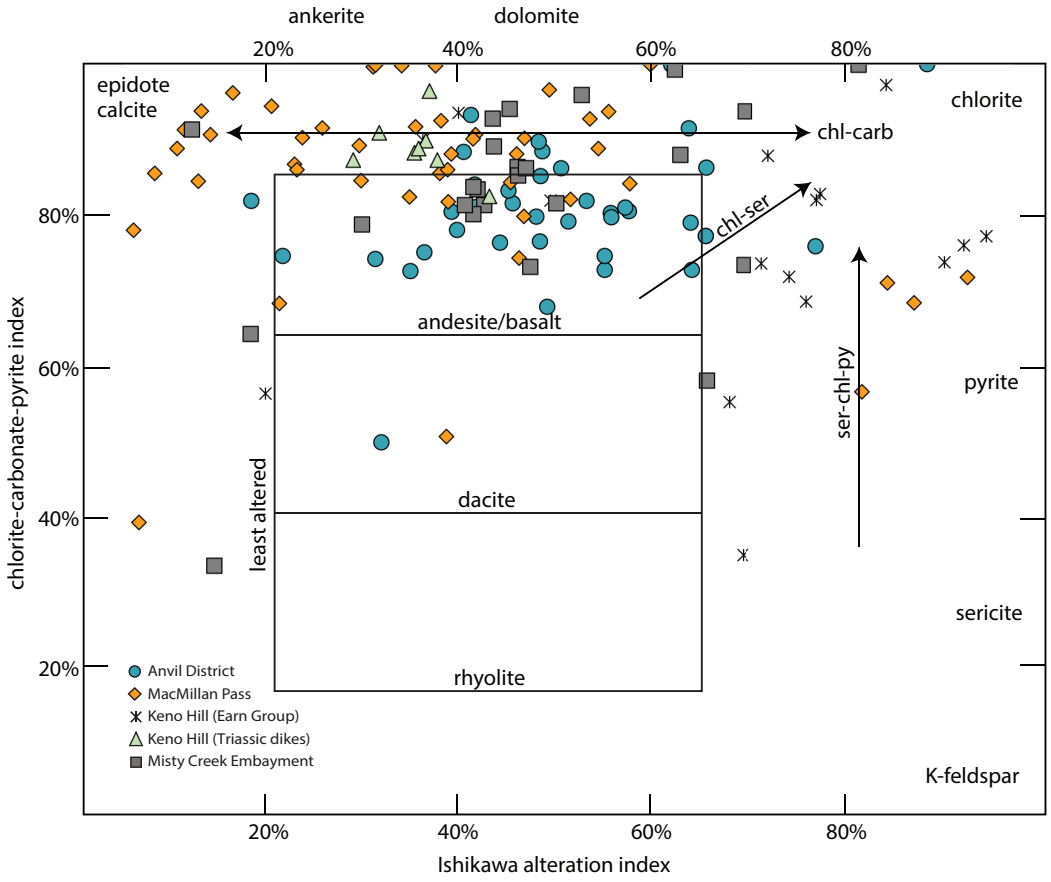

Figure 13. Chlorite-carbonate-pyrite index (CCPI) versus alteration index (AI) box plot of Large et al. (2001). Samples from MacMillan Pass are pervasively altered by ankerite, calcite and chlorite. Keno Hill dikes show more alteration on the box plot than what appears in thin section. Earn Group samples are metamorphic and so alteration indices could be overprinted by metamorphic fluids. CCPI = 100 x (MgO + FeOt) / (MgO + FeOt + Na_2O + K_2O). Ishikawa alteration index = 100 x (K_2O + MgO) / (K_2O + MgO + Na_2O + CaO).

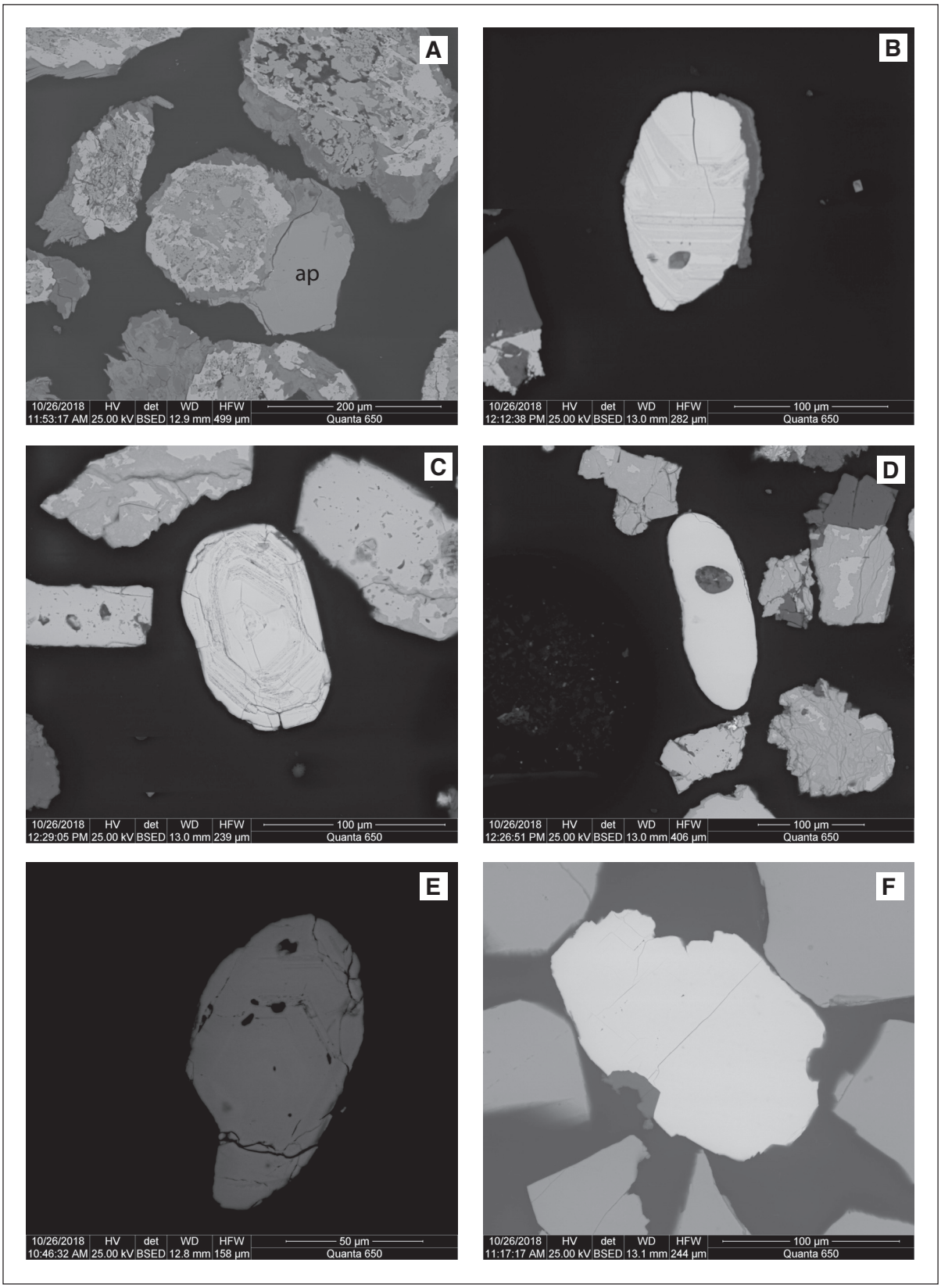

Figure 14. Backscatter electron (BSE) images of grain mounts. A. Polycrystalline cluster in sample MC-41, which most apatite (ap) grains occur in. B. Zoned zircon in sample MP-27. C. Zoned zircon in sample MP-33. D. Unzoned zircon with an inclusion in sample MP-33. E. Zoned zircon in sample EG-01. F. Monazite grain in sample EG-17.

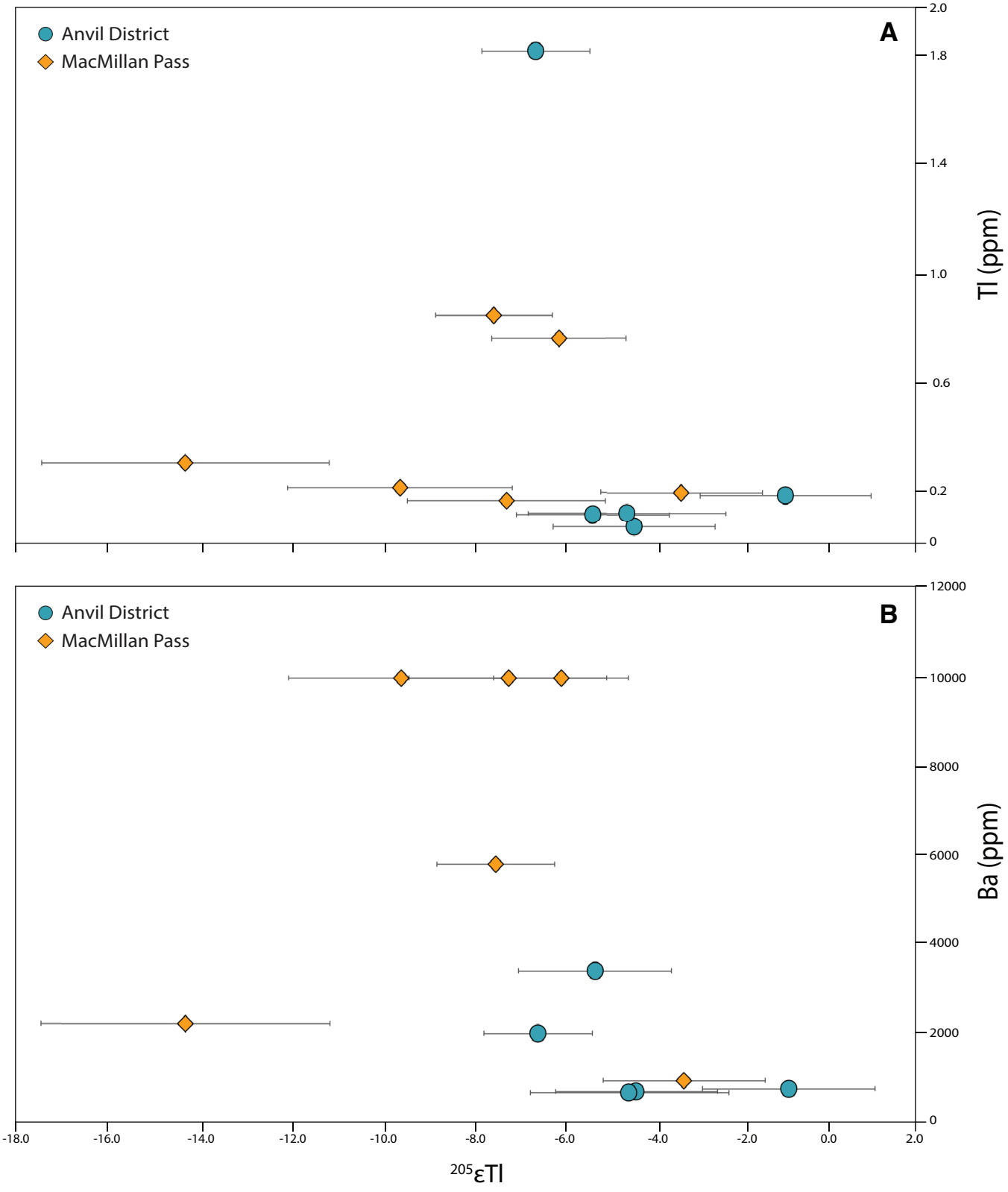

Figure 15. A. Bivariate plot of $^{205}\varepsilon$Tl versus Tl; B. Bivariate plot of $^{205}\varepsilon$Tl versus Ba. There is no apparent correlation with Tl abundance, whereas there is a negative correlation between $^{205}\varepsilon$Tl and Ba. One outlier is present in the MacMillan Pass samples, with the most negative $^{205}\varepsilon$Tl value.

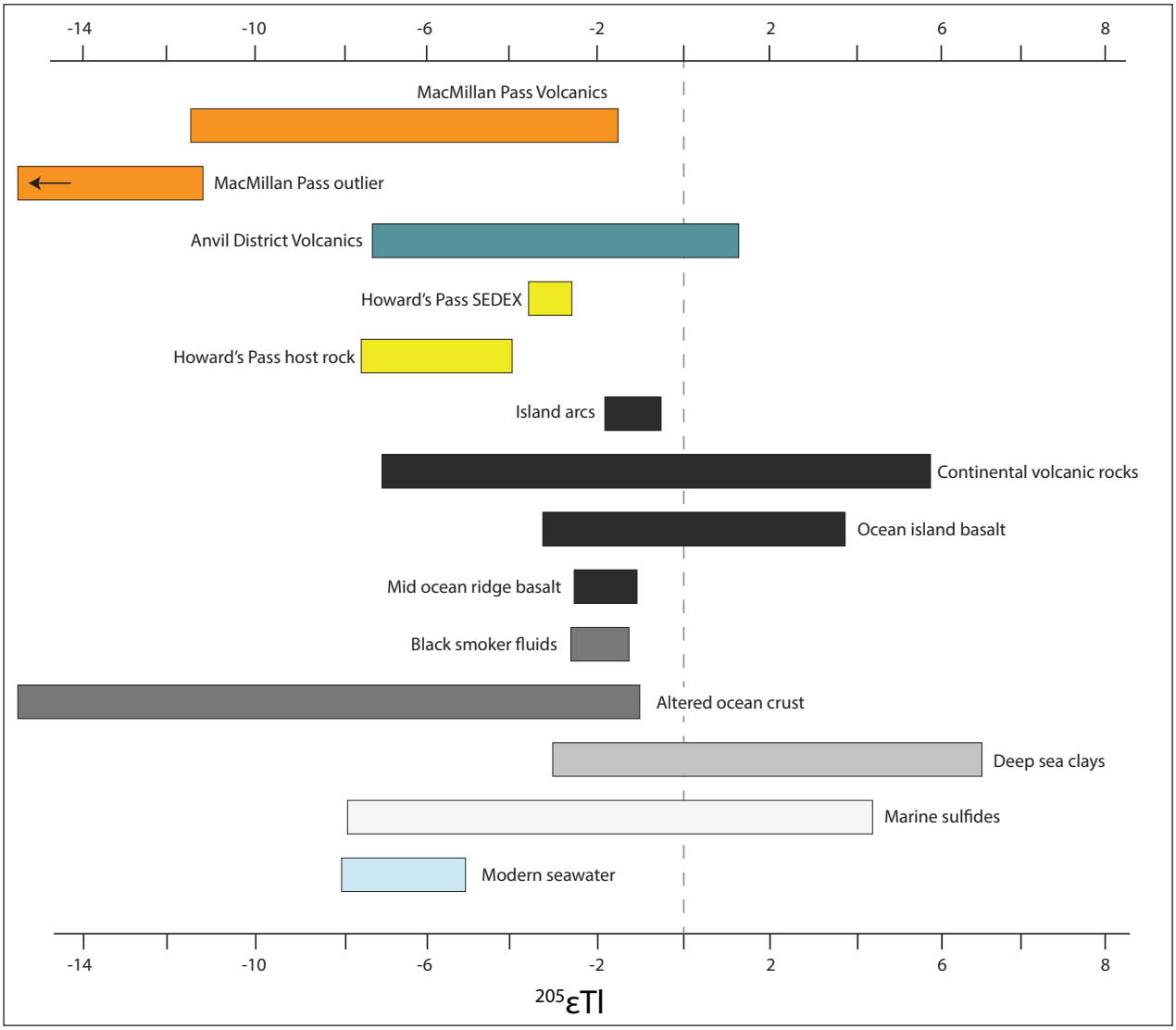

Figure 16. Figure 16: $^{205}\varepsilon Tl$ isotope ranges for measured samples (this paper), Howard's Pass (Peter et al., 2018) and a variety of environments (Kersten et al., 2014, and references therein).

Table 1: Results of $^{205}\varepsilon$Tl analysis.

Sample	$^{205}\varepsilon$Tl	2σ	Tl (ppm)	Ba (ppm)
MACMILLAN PASS				
MP-03	-5.9	1.5	0.762	10000
MP-11	-14.2	3.2	0.299	2190
MP-09	-7.4	1.3	0.848	5790
MP-47	-3.2	1.8	0.187	901
MP-18	-7.1	2.2	0.155	10000
MP-20	-9.5	2.5	0.202	10000
ANVIL DISTRICT				
MC-10	-6.4	1.2	1.83	1965
MC-41	-0.9	1.9	0.176	713
MC-13	-5.2	1.7	0.103	3380
MC-30	-4.2	1.8	0.059	648
MC-29	-4.4	2.2	0.108	623

Evaluating portable Raman spectrometers for use in exploration of pegmatite dikes, Wekusko Lake, Manitoba

D. Benn[1], R. Linnen[1], and T. Martins[2]

Abstract: Pegmatite deposits are an important source of lithium, which increasingly is used in battery technologies. The rare-metal pegmatite dikes of the Green Bay group from the Wekusko Lake pegmatite field in Manitoba offer an excellent opportunity to investigate new exploration techniques for lithium pegmatites. The dikes were mapped and sampled during the summer of 2018, and this work revealed that the pegmatite dikes are deformed and folded. The examination of drill core revealed that the pegmatite dikes exhibit five zones, defined by their minerology and grain size: a border zone, wall zone, intermediate zone, central zone and a core zone. The zones vary in width and all zones are not always present in each pegmatite. The crystal habit of muscovite, feldspar and spodumene vary based on the host zone and muscovite mineral chemistry is being examined as a potential vector for Li mineralization. Columbite-group (CGM) minerals are zoned with respect to Nb and Ta values and primary grains have been selected for U-Pb geochronological studies.

INTRODUCTION

The emergence of new technologies in electric cars and reThe emergence of new technologies in electric cars and renewable energies has led to an increase in the use of lithium (Li)-ion batteries. As a result, Li has become highly sought-after. Lithium is obtained primarily from two deposit types; pegmatites (e.g., Greenbush, Australia), where spodumene is the main ore mineral, or brines (e.g., Salar de Atacama, Chile). Of these deposits, pegmatites contain the highest lithium grades.

In Canada, the primary Li deposits are Li-Cs-Ta (LCT) pegmatites. This includes the Whabouchi pegmatite in Quebec, which is scheduled to come into production. However, one of the most well-known deposits is the Archean Tanco pegmatite, a former Li producer in southeast Manitoba. One of the active Li pegmatite exploration areas in Manitoba is the Wekusko Lake pegmatite field (FAR Resources Ltd., 2018; 2017), which contains Trans-Hudson aged LCT pegmatites (Černý et al., 1981; Martins et al., 2017). The Green Bay Group of pegmatite dikes in this field are the focus of this study.

Many of the main pegmatite minerals, such as albite, microcline, spodumene, petalite, pollucite, amblygonite, and beryl can be white (London, 2017). Thus, the colour of common pegmatite minerals can be a challenge for accurate field identification. Hematization also commonly complicates the identification of minerals in the field, particularly for the differentiation of feldspars. Of the common minerals, micas are of particular interest since they may contain significant quantities of Li, and thus may have potential as a vector for Li mineralization. However, in the field the Li concentrations of micas are not always possible to differentiate by visual inspection alone.

WEKUSKO LAKE PEGMATITE FIELD

The Wekusko Lake pegmatite field is located in the Flin Flon-Glennie complex (Connors et al., 2002) of the Paleoproterozoic Trans-Hudson Orogeny, an east-west trending belt approximately 140km wide and 240km long. The region has undergone five deformational and folding events (Kraus and Williams, 1999; Connors et al., 2002). Multiple mafic and felsic intrusions have occurred the Flin Flon belt (Černý et al., 1981; Kraus and Williams, 1999). The emplacement of the granitic pegmatites of the Wekusko Lake pegmatite field is thought to be the last intrusive event. However, deformation of muscovite and feldspar (Martins et al., 2017) indicates that the pegmatite were emplaced dikes prior to the final deformation event. Recent geological mapping (Benn et al., 2018a, b) revealed that the pegmatites are folded, corroborating the interpretations of Martins et al. (2017). The Green Bay Group of pegmatite dikes in the study area are dominantly hosted by a mafic volcanic assemblage. This assemblage is unconformably overlain by the Missi group metasedimentary rocks (Connor et al., 1999). These units make up the Roberts Lake fault block (Connor et al., 1999; 2002) and are bound to west by a north-northeast trending fault and to the south by an east-northeast trending fault. The two faults meet to form the southwest corner of the block.

Bedrock mapping of pegmatite dikes from the Green Bay group of the Wekusko Lake pegmatite field was undertaken as a scale of 1:4000 (Figure 1; Benn et al., 2018a, b). There are at least 13 dikes in the field area identified as part of the Green Bay group (FAR Resources Ltd., 2019), 8 of which were investigated in this study.

[1]Department of Earth Sciences, Western University, 1151 Richmond Street N., London, Ontario N6A 5B7
[2] Manitoba Geological Survey, 1395 Ellice Avenue, Winnipeg, Manitoba R3G 3P2

The primary unit in the mapping area is amphibolite derived from mafic volcanic rocks (Figure 1). Quartzofeldspathic gneiss and biotite garnet gneiss are also present in the mapped area. Detailed field descriptions of the rock units can be found in Benn et al. (2018a).

The mafic volcanic rocks show relatively flat chondrite-normalize rare earth element plots, typical of normal-type mid-ocean-ridge basalts (Benn et al., 2018a). Samarium-Nd isotopic analyses reveal a ε_{Nd} value between 2.8 and 3.8 at 1.86Ga. These results support previous interpretations (NATMAP Shield Margin Working Group, 1998; Syme et al., 1999).

Benn et al. (2018a) classified the pegmatites of this study as belonging to the rare-element (REL) class, REL-Li sub-class, complex type, spodumene subtype based on the classification of Černý and Ercit (2005). The pegmatite dikes consist of quartz, K-feldspar, albite, muscovite, spodumene, and tourmaline with accessory beryl, apatite, garnet, zircon and CGM (Benn et al., 2018a). The dikes vary in grain size with some quartz and feldspar crystals reaching up to 30cm in length and other zones displaying aplitic textures with fine (1mm) grain sizes.

PEGMATITE DIKES

Benn et al. (2018a) defined 5 zones within the pegmatite dikes, based on the mineralogy, grain size, crystal habit and colour: a border zone, wall zone (Figure 2a), intermediate zone (Figure 2b; c), central zone (Figure 2d), and a core zone. The different pegmatite zones are not always apparent in all the dikes and vary within the length and depth of the dike. Thin dikes, in particular, tend to lack central and core zones. Detailed descriptions of the zones can be found in Benn et al. (2018a).

The colour of the pegmatite dikes changes from brick red at near the walls to white in the center caused by a shift in the dominate feldspar from K-feldspar to albite (Benn et al., 2018a). This colour variation may also be a result of greater fluid interaction near the pegmatite contacts resulting in a higher degree of hematization (Gysi et al, 2016).

Spodumene has three textural varieties in the pegmatite dikes (Martins et al., 2017). The most common variety is primary, sub- to euhedral, pale green and coarse-grained (up to 30cm in length). The second variety, most common in the intermediate zone, is fine-grained, anhedral, and intergrown with quartz. The third variety is present as interstitial fine-grained masses, between larger, well-formed crystals, which suggests a later crystallization.

Muscovite occurs as two forms in the pegmatite dikes (Martins et al, 2017). The primary form is light brown, coarse-grained (<5cm) subhedral books. Locally, this type exhibits a comb texture, perpendicular to contacts within the wall zone. The second form is secondary, yellow muscovite that occurs as fine-grained masses that have replaced feldspars. This form is most commonly present within the wall zone. Benn et al. (2018a) identified at least two varieties of feldspar in the pegmatite dikes. The first variety occurs as large creamy white, sub- to euhedral crystals. This feldspar is interpreted as albite, however there are crystals which display perthitic textures, indicating that some of these crystals are K-feldspar. The second variety is pink, fine-grained and forms interstitial masses around other sub- to euhedral crystals.

Fe-Mn phosphate minerals are present as dark red to brown, medium-grained (1cm) crystals that form subhedral masses. They are primarily present in the central zone. These phosphates have been identified as part of the triphylite (Fe) to lithiophilite (Mn) series based on Fe, Mn, and P peaks from SEM-EDS analyses.

Columbite- group minerals form needle- and pear-like grains up to 1mm in length, but most are 25-50µm long (Figure 3a-d). The grains are generally situated around larger (>1mm) tourmaline grains and locally are associated with zircon. The GCM are most common in the central zone, but can be present in other zones as well. The CGM display minor Nb-Ta zonation (Figure 3a) and where zonation is present, the GCM typically have a Nb-enriched core with a Ta-enriched rim (Figure 3b-d). Selected CGM grains will be dated by U-Pb geochronology to better understand the pegmatite emplacement, and deformation history of the area.

FUTURE WORK

Handheld field portable Raman spectrometers can be used to identify Li-bearing minerals, in contrast to portable XRF units that determine chemical compositions but cannot determine light elements such as Li. Raman spectroscopy is also non-destructive and performed in-situ with minimal sample preparation (e.g., creating powders), another advantage to portable XRF units. Raman spectroscopy is based on molecular structure and consequently mineral polymorphs can be distinguished by this technique. Most of the common LCT pegmatite minerals have well documented databases of Raman spectra. Consequently, one of the objectives is to evaluate whether Raman spectroscopy, particularly the use of field-portable Raman spectrometers is useful for Li pegmatite exploration. This work is currently in progress.

Lithium substitutes into the octahedral site of muscovite (Brigatti et al, 2001). This substitution creates stresses on the molecular bonds of the muscovite, which should be reflected in the Raman spectra. As a result, Li content within muscovite may be tracked using Raman spectroscopy. Lithium contents will be calibrated through the use of Laser Ablation Induction Coupled Plasma Mass Spectroscopy (LA-ICP-MS) and Secondary Ion Mass Spectroscopy (SIMS).

ACKNOWLEDGEMENTS

FAR Resources Ltd. is thanked for access to drill core, field and helicopter support. This project could have not happened without the support of the late K. Anderson, who is missed. Strider Resources Ltd. is acknowledged for access to light detection and ranging (LiDAR) imagery. Field and logistical support as well as the lithogeochemical, age-dating and Sm-Nd isotopic analyses from the Manitoba Geological Survey are also gratefully acknowledged. Discussions with M. Fedikow, J. Singh, D. Ziehlke and J. Ziehlke greatly benefited this project. Marc Beauchamp at The University of Western Ontario is thanked for support while operating the EMPA. This study is supported by a Targeted Geoscience Initiative Phase 5 Program grant from Natural Resources Canada to R. Linnen.

REFERENCES

Benn, D., Linnen, R.L. and Martins, T.
2018a: Geology and bedrock mapping of the Wekusko Lake pegmatite field (northeastern block), central Manitoba (part of NTS 63J13); in Report of Activities 2018, Manitoba Growth, Enterprise and Trade, Manitoba Geological Survey, p. 79–88.

Benn, D., Martins, T., Linnen, R.L., Ziehlke, J. and Singh, J.
2018b: Bedrock geology of the Wekusko Lake pegmatite field (northeastern block), central Manitoba (part of NTS 63J13); Manitoba Growth Enterprise and Trade, Preliminary Map PMAP2018-2, scale 1:4000.

Brigatti, M.F., Kile, D.E. and Poppi, M.
2001: Crystal structure and crystal chemistry of lithium-bearing muscovite-2m1; The Canadian Mineralogist, v. 39, no. 4, p. 1171–1180.

Černý, P. and Ercit, T.S.
2005: The classification of granitic pegmatites revisited; The Canadian Mineralogist, v. 43, no. 6, p. 2005–2026.

Černý, P., Trueman, D.L., Zeihlke, D.V., Goad, B.E. and Paul, B.J.
1981: The Cat Lake–Winnipeg River and the Wekusko Lake pegmatite fields, Manitoba; Manitoba, Department of Energy and Mines, Mineral Resources Division, Economic Geology Report ER80-1, 216 p. plus 5 maps.

Connors, K.A., Ansdell, K.M. and Lucas, S.B.
1999: Coeval sedimentation, magmatism, and fold-thrust development in the Trans-Hudson Orogen: propagation of deformation into an active continental arc setting, Wekusko Lake area, Manitoba; Canadian Journal of Earth Sciences, v. 36, no. 2, p. 275–291.

Connors, K., Ansdell, K. and Lucas, S.
2002: Development of a transverse to orogen parallel extension lineation in a complex collisional setting, Trans-Hudson Orogen, Manitoba, Canada; Journal of Structural Geology, v. 24, no. 1, p. 89–106.

Gysi, A.P., Williams-Jones, A.E. and Collins, P.
2016: Lithogeochemical vectors for hydrothermal processes in the Strange Lake peralkaline granitic REE-Zr-Nb deposit; Economic Geology, v. 111, no. 5, p. 1241–1276.

FAR Resources Ltd.
2017: Phase 3 drilling; FAR Resources Ltd., URL <https://www.far-resources.com/phase-3-drill¬ing/> [August 2018].

FAR Resources Ltd.
2018: Phase 4 drilling; FAR Resources Ltd., URL <https://www.far-resources.com/phase-4-drill¬ing/> [August 2018].

FAR Resources Ltd.
2019: Far Resources discovers five new pegmatite dykes and significantly expands pegmatite field at the Zoro Lithium Project, Manitoba.; FAR Resources Ltd., URL <https://farresources.com/news/2019/2/18/far-resources-discovers-five-new-pegmatite-dykes-and-significantly-expands-pegmatite-field-at-the-zoro-lithium-project-manitoba/> [March 2019].

Kraus, J. and Williams, P.F.
1999: Structural development of the Snow Lake allochthon and its role in the evolution of the southeastern Trans-Hudson Orogen in Manitoba, central Canada; Canadian Journal of Earth Sciences, v. 36, no. 11, p. 1881–1899.

London, D.
2017: Reading pegmatites: part 3—what lithium minerals say; Rocks & Minerals, v. 92, no. 2, p. 144–157.

Martins, T., Linnen, R.L., Fedikow, M.A.F. and Singh, J.
2017: Whole-rock and mineral geochemistry as exploration tools for rare-element pegmatite in Manitoba: examples from the Cat Lake–Winnipeg River and Wekusko Lake pegma¬tite fields (parts of NTS 52L6, 63J13); in Report of Activities 2017, Manitoba Growth, Enterprise and Trade, Manitoba Geological Survey, p. 42–51.

NATMAP Shield Margin Project Working Group
1998: Geology, NATMAP shield margin project area (Flin Flon Belt), Manitoba/Saskatchewan; Geological Survey of Canada, Map 1968A, scale 1:100 000.

Syme, E. C., Lucas, S. B., Bailes, A. H. and Stern, R. A.
1999: Contrasting arc and MORB-like assemblages in the Paleoproterozoic Flin Flon belt, Manitoba, and the role of intra-arc extension in localizing volcanic-hosted massive sulphide deposits; Canadian Journal of Earth Sciences, v. 36, no. 11, p. 1767–1788.

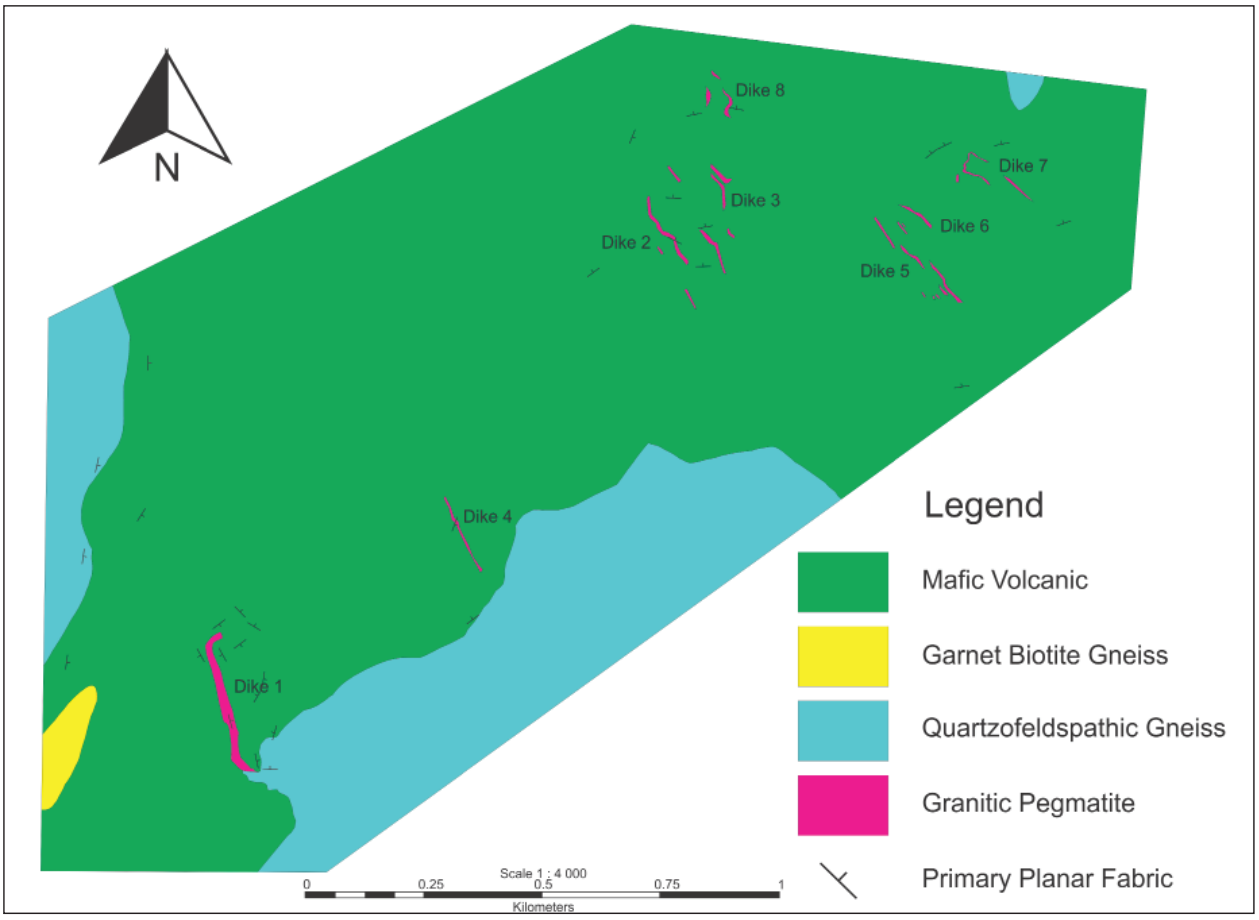

Figure 1. Simplified bedrock geological map of Wekusko Lake pegmatite field (northeastern block), central Manitoba, modified from Benn et al. (2018b).

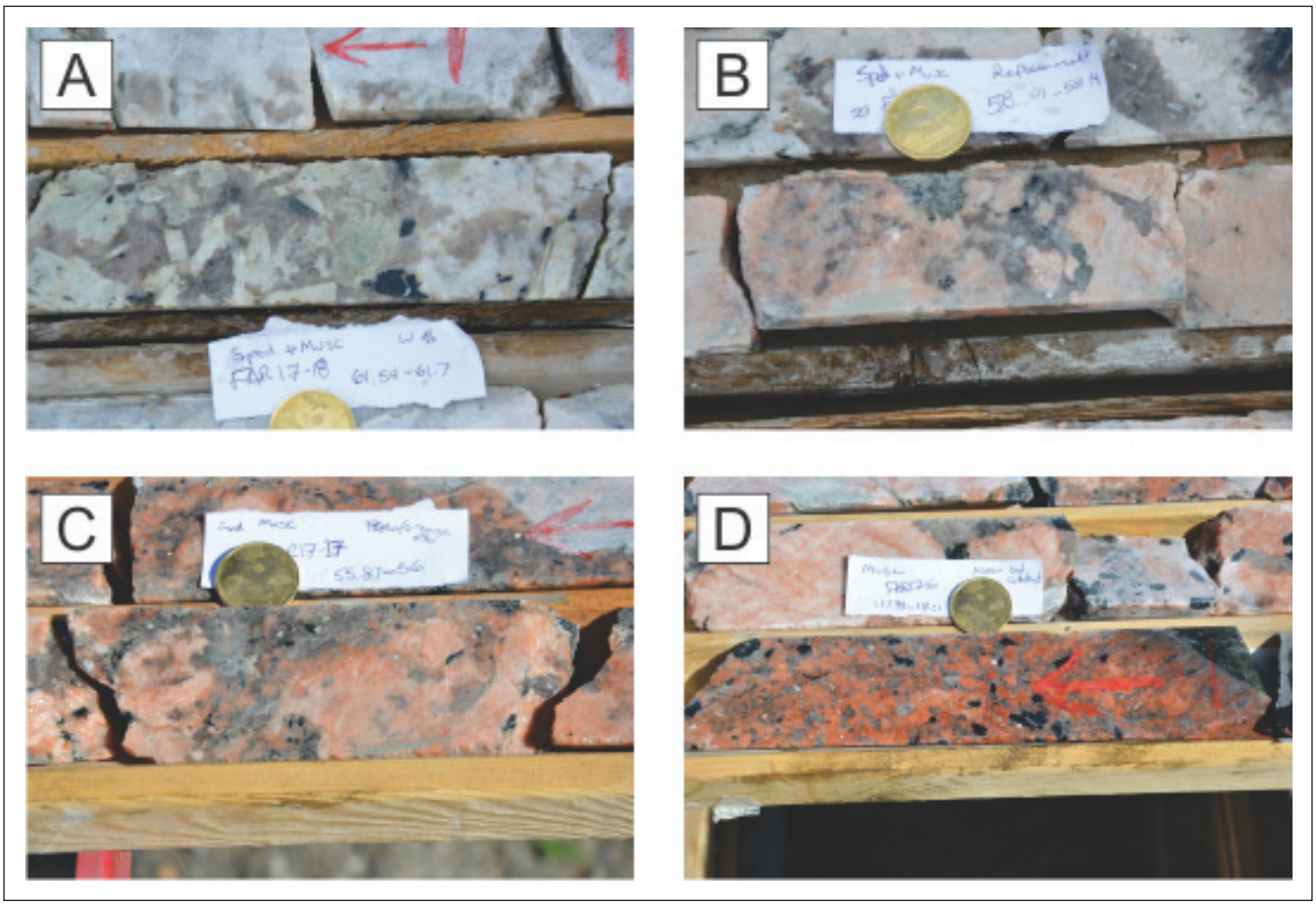

Figure 2. Drill core photographs displaying the transition from a) the brick red wall zone to b), c) the salmon pink intermediate zone to d) the white central zone. Coins for scale (after Benn et al., 2018a).

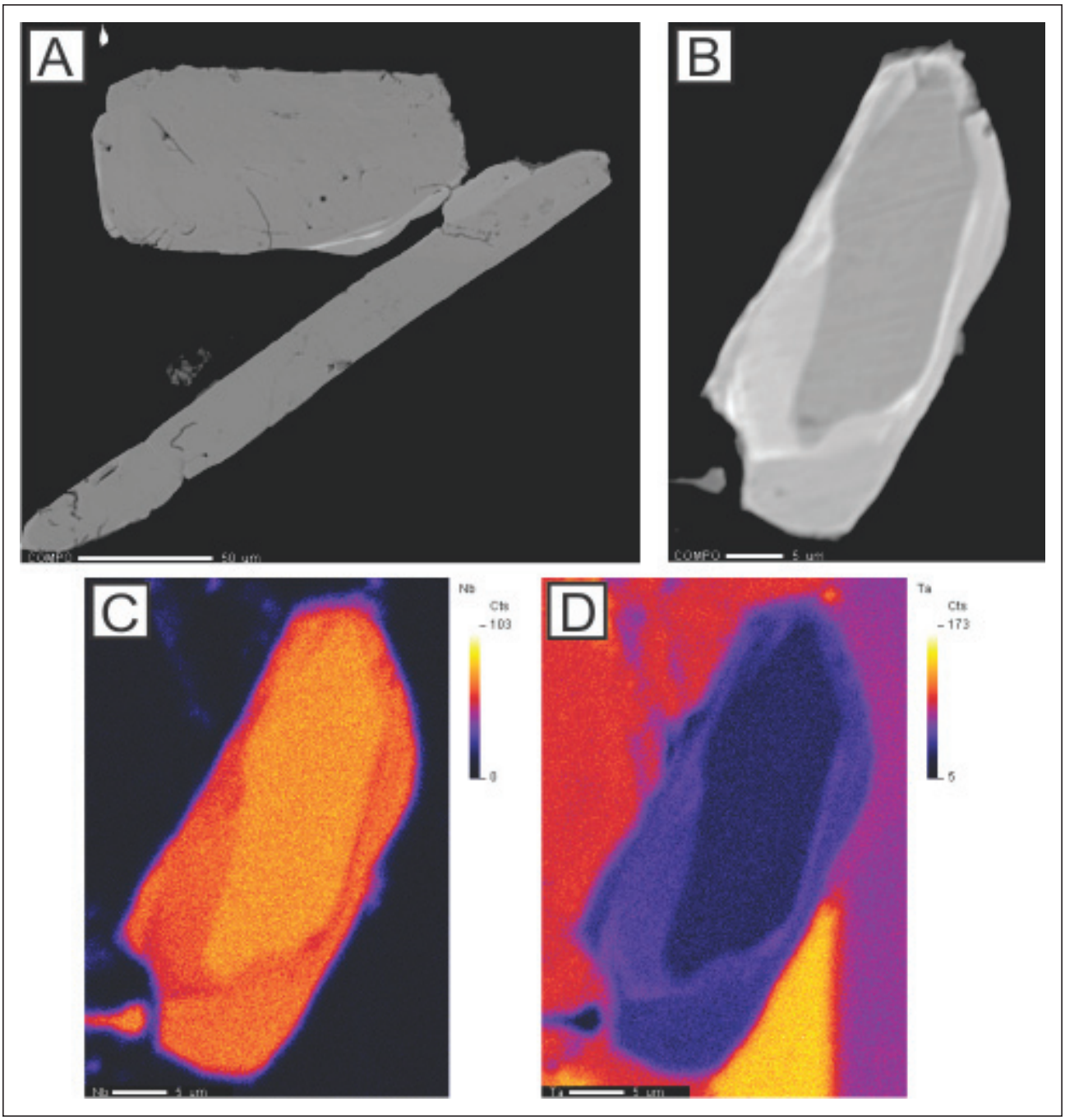

Figure 3. Backscattered electron images and false coloured element maps for CGM: a) unzoned CGM; b) zoned CGM; c) Nb concentration of zoned CGM; d) Ta concentrations of zoned CGM.

Convergent margin Ni-Cu-PGE-Cr ore systems: temporal and magmatic evolution

Graham T. Nixon[1], Déjan Milidragovic[1] and James S. Scoates[2]

Abstract: Ultramafic-mafic intrusions at convergent margins contain some of the world's significant Ni-Cu-PGE sulphide deposits and are becoming an increasingly important exploration target. This class of intrusions is well-represented in the accreted arc terranes of the northern Cordillera, particularly the Alaskan-type subclass. In this report, we describe current research on three Alaskan-type intrusions in British Columbia that are variably endowed in magmatic Ni-Cu-PGE mineralization. The goal of this project is to determine the timing of mineralization in relation to the temporal and magmatic evolution of the intrusion and to develop new mineral deposit models as guides for exploration. U-Pb and $^{40}Ar/^{39}Ar$ geochronological results for the Turnagain intrusion indicate multi-stage assembly of a composite body in the Early Jurassic (ca. 189-185 Ma) during initial accretion of arc terranes to the ancient North American continental margin. Ni(-Co) and Cu-PGE sulphide mineralization is partitioned within separate sub-intrusions that were emplaced during active accretion. A newly investigated zone of Cu-Pd-Pt sulphide mineralization in the Tulameen intrusion bears a strong resemblance to certain "reef-style" deposits in layered intrusions. Preliminary geochronology results indicate emplacement of the Tulameen intrusive suite in the latest Triassic (ca. 204-206 Ma), coincident with the most prolific Cu-Au porphyry epoch in British Columbia. Investigation of magmatic sulphide occurrences at the Polaris Alaskan-type intrusion was initiated last summer and samples collected during the field season are currently being processed and examined.

INTRODUCTION

The majority of the world's magmatic Ni-Cu-PGE resources are hosted by ultramafic-mafic intrusions and volcanic rocks in various rift-related tectonic settings (e.g. Naldrett, 2010). Traditionally, convergent margins have been regarded as unfavourable environments for nickel exploration due to the dearth of economically exploitable magmatic Ni-Cu-PGE sulphide deposits. However, recent discoveries of significant Ni-sulphide deposits have established ultramafic-mafic intrusions in convergent margin settings as an increasingly important economic resource. Notable examples include Xiarihamu, host to the second largest Ni deposit in China (Li et al., 2015; Song et al., 2016) and the Aguablanca mine in Spain, Europe's only nickel mine (Piña, 2019).

The ultramafic-mafic intrusions at convergent margins belong to a global class of such bodies emplaced during active or post-subduction tectonic regimes where subduction-modified mantle source regions have imparted arc geochemical signatures to the intrusive rock suites. Two principal mineralogical subtypes of convergent margin intrusion may be recognized: Alaskan-type intrusions, which characteristically lack orthopyroxene as a crystallizing phase; and "Giant Mascot(GM)-type" intrusions, which contain abundant cumulus or post-cumulus orthopyroxene (Nixon et al., 2015; Manor et al., 2016, 2017) (Fig. 1). Both subtypes may exhibit a zonal arrangement of lithologies extending from dunite in the core of the intrusive body through orthopyroxene-bearing (harzburgite/lherzolite) or orthopyroxene-free (wehrlite) peridotite to hornblende-bearing pyroxenite and hornblendite ± gabbro at the margin. In contrast to GM-type intrusions, which are host to a growing number of economically significant Ni-sulphide deposits (Nixon et al., 2015), Alaskan-type intrusive suites are commonly perceived to evolve in sulphide deficient environments and are primarily known for their chromitite-PGE mineralization in the dunite core and derivative, economically important platinum placers (e.g. Tulameen, Nixon et al., 1990; and see reviews by Johan, 2002; and Weiser, 2002).

Alaskan-type ultramafic-mafic intrusions are well-represented in the accreted terranes of the northern Cordillera (Fig. 1). In British Columbia, these intrusions are predominantly Late Triassic to Early Jurassic in age and restricted to the early Mesozoic arc terranes of Quesnellia/Stikinia and their late Paleozoic "basement" assemblages that were accreted to the North American continental margin in the Mesozoic (e.g. Nelson et al., 2013). Our current studies focus on three Alaskan-type bodies in British Columbia, the Turnagain, Tulameen and Polaris intrusions described below, that are variably endowed in magmatic Ni-Cu-PGE sulphide mineralization. The primary objective of this project is to establish the nature and timing of mineralization in the context of the temporal and magmatic evolution of their host intrusions, and subsequently to develop new mineral deposit models as a guide to exploration.

[1]British Columbia Geological Survey, 1810 Blanshard Street, Victoria, British Columbia V8W 9N3
[2]Pacific Centre for Isotopic and Geochemical Research (PCIGR), Department of Earth, Ocean and Atmospheric Sciences, 2020 – 2207 Main Mall, University of British Columbia, Vancouver, British Columbia V6T 1Z4

TURNAGAIN

The Turnagain ultramafic-mafic intrusion in north-central British Columbia (Fig. 1) is unusually enriched in magmatic sulphides when compared to typical Alaskan-type intrusions. The current resource of low-grade Ni-sulphide mineralization at Turnagain is estimated to contain 1842 Mt of 0.21 wt % Ni and 0.013 wt % Co (Mudd and Jowitt, 2014), ranking it among the top 10 largest such deposits in the world. The Turnagain intrusion has been the focus of early geological work tied to mineral exploration (Clark, 1975, 1978, 1980) and subsequent academic studies (Scheel, 2007; Scheel et al., 2009), including TGI-funded research on rocks that host Cu-PGE mineralization (Jackson-Brown, 2017), which is a current exploration target. In this report, recent U-Pb geochronological results are summarized and used to constrain the timing of Ni-Cu-PGE mineralization and multi-stage emplacement of the Turnagain intrusive suite in relation to regional tectonic events accompanying the accretion of outboard arc terranes to the North American continental margin.

On the basis of geological, geochemical and geochronological data, Erdmer et al. (2005) argued that the Turnagain Alaskan-type body intruded Paleozoic metasedimentary and metavolcanic rocks that belong to the miogeoclinal margin of North America, and that the Turnagain intrusion and its host rocks are therefore not part of an accreted terrane. Using regional geophysical data, Nixon et al. (2019) inferred the presence of a cryptic suture, the Turnagain fault, separating the Turnagain intrusion and its host rocks from strata of the North American miogeocline, and correlated the Turnagain host stratigraphy with elements of the accreted pericratonic Yukon-Tanana terrane (Fig. 2). Furthermore, restoration of post-mid-Cretaceous displacements along major strike-slip faults in northern British Columbia and south-central Yukon (Gabrielse, 1985; Nelson et al., 2006) reveals that Triassic-Jurassic Alaskan-type bodies in northern British Columbia originally formed a coherent belt of intrusions over 200 km in length and are confined to the accreted arc terranes of Quesnellia and Stikinia (Nixon et al., 2019). As shown below, the timing of accretion is intimately linked with emplacement, crystallization and Ni-Cu-PGE mineralization in the composite Turnagain intrusion.

The Turnagain ultramafic-mafic body has been described as a typical Alaskan-type intrusion zoned from a dunite-wehrlite core to a hornblende clinopyroxenite-hornblendite margin (Clark, 1975, 1980). However, recent investigations have shown that the lithological zoning is formed by four compositionally, spatially and temporally distinct sub-intrusions arranged eccentrically about a central dunite-wehrlite body (Fig. 2). From oldest to youngest, the four intrusive bodies (Stages 1-4) comprise: 1) interlayered wehrlite, clinopyroxenite and minor dunite that form a small intrusion at the northern margin of the complex; 2) dunite and wehrlite in the central intrusive phase with minor clinopyroxenite and hornblendite near the periphery; 3) diorite and minor feldspathic hornblendite in the core of the complex; and 4) hornblende/magnetite clinopyroxenite with minor wehrlite and clinopyroxenite at the western margin of the composite intrusion (Fig. 2). Contacts between the intrusive phases are sharp and locally marked by intrusive breccias and dykes. The main Ni-sulphide mineralization is hosted by Stage 2 wehrlite-dunite where it forms semi-massive, net-textured and disseminated zones. The youngest intrusive phase (Stage 4) contains thin localized zones of lensoid to blebby and disseminated magnetite and Cu-PGE sulphide mineralization. Further descriptions of the mineralogy and textures of the Ni-Cu-PGE mineralization and host rocks are given in Scheel (2007) and Jackson-Brown (2017).

GEOCHRONOLOGY

The staged emplacement and crystallization of the Turnagain intrusion has been calibrated using high-precision isotope dilution-thermal ionization mass spectrometry (ID-TIMS) U-Pb (zircon, titanite) and $^{40}Ar/^{39}Ar$ (hornblende, phlogopite) geochronology. All analyses were carried out at the Pacific Centre for Isotopic and Geochemical Research (PCIGR), University of British Columbia. Details of the samples, analytical techniques and interpretation of the geochronological results are given in Nixon et al. (2019).

Ultramafic and dioritic rocks from three of the four intrusive stages have been successfully dated. A hornblendite dyke, cutting a large inclusion of metasedimentary rocks at the northern margin of the Stage 2 intrusion, yields a weighted mean $^{206}Pb/^{238}U$ date of 190.3 ± 4.6 (2σ) Ma on titanite, and a statistically identical $^{40}Ar/^{39}Ar$ plateau date of 187.4 ± 1.5 (2σ) Ma on hornblende (Fig. 2). Phlogopite from a wehrlite at the southern margin of the Stage 2 intrusive phase yields a $^{40}Ar/^{39}Ar$ plateau date of 188.6 ± 1.2 Ma (Fig. 2). The U-Pb and $^{40}Ar/^{39}Ar$ dates are statistically concordant and are interpreted as the time of cooling through the nominal closure temperatures of titanite (670°C), hornblende (570°C) and phlogopite (~450°C) (Hodges, 2014). The $^{40}Ar/^{39}Ar$ phlogopite date is taken as a minimum crystallization age for the Stage 2 intrusion. For a Stage 3 melanocratic diorite, the weighted mean $^{206}Pb/^{238}U$ date of 188.11 ± 0.13 Ma on zircon is interpreted to represent the crystallization age of this dioritic intrusion.

Wehrlite and leucodiorite from Stage 4 give distinctly younger U-Pb results (Fig. 2). The wehrlite (Stage 4a) yields a bimodal distribution of zircon dates: a younger weighted mean $^{206}Pb/^{238}U$ date of 185.68 ± 0.19 Ma interpreted as the crystallization age; and a significantly older weighted mean $^{206}Pb/^{238}U$ date of 236.37 ± 0.23 Ma (Triassic) for zircon of xenocrystic origin. The leucodiorite (Stage 4b) yields a weighted mean $^{206}Pb/^{238}U$ zircon crystallization age of 185.30 ± 0.12 Ma, statistically younger than the wehrlite, indicating that emplacement and crystallization of the Stage 4 intrusion may have extended over several hundred thousand years. Xenocrystic zircon entrained in the wehrlite may have originated via assimilation of Triassic granitoid

intrusion(s) at depth. Detrital zircon grains from a volcanic wacke within a large metasedimentary inclusion of wall-rock at the northern edge of the Stage 2 intrusion yield a discordant array of results with Precambrian inheritance (ca. 2.1 Ga) and a concordant fraction ca. 301 Ma (uppermost Pennsylvanian) taken as the maximum depositional age of the wacke. Accordingly, the stratigraphic succession that hosts the Turnagain intrusion has a minimum age range of Mississippian to latest Pennsylvanian.

The U-Pb and $^{40}Ar/^{39}Ar$ geochronological results reported above are consistent with intrusive relationships observed in the field and support a multi-stage emplacement and crystallization of the Turnagain intrusion. The magmatic evolution of the composite intrusion evidently extended over at least four million years in the Early Jurassic (ca. 189-185 Ma). This span of intrusive activity is a minimum as the oldest Stage 1 component of the Turnagain complex has yet to be dated. The Ni-(Co) and Cu-PGE sulphide mineralization in the Stage 2 and Stage 4 intrusions, respectively, appears to have formed in independent magmatic systems emplaced in a syn-accretionary tectonic environment (discussed below).

ALLOCHTHONOUS TERRANE ACCRETION

The geochronological results for the Turnagain intrusive suite place rigorous constraints on Early Jurassic tectonic events. Regional contractional deformation has deformed the greenschist-facies rocks that host the intrusion into tight, upright to overturned, northeasterly vergent folds (Nixon et al., 1989; Erdmer et al., 2005). Magmatic layering in ultramafic rocks of the Stage 1 intrusion is deformed into a synformal structure concordant with folds in the host rocks, implying pre- to synkinematic intrusion of Stage 1. Structures within the ca. 301 Ma metasedimentary inclusion in Stage 2 are concordant with those in the host succession and absent within Stage 2 ultramafic rocks. Emplacement of Stage 2, therefore, post-dates this folding event which occurred prior to emplacement, crystallization and cooling of the Stage 2 intrusion at ca. 189 Ma. Information from drill core indicates that the Turnagain intrusion is underlain by a shallowly dipping basal fault, exposed along the eastern margin of the complex (Fig. 2), that is interpreted as a thrust from kinematic indicators at surface (Nixon et al., 2017). This thrust event postdates emplacement of the entire intrusion and is constrained to be younger than emplacement and crystallization of the youngest Stage 4 intrusive component at ca. 185 Ma. Structures produced during this contractional event can be traced into the miogeoclinal rocks of North America (Nixon et al., 1989, Erdmer et al., 2005).

The entwined evolution of magmatic and tectonic events at Turnagain calibrated by our geochronological results have implications for arc terrane accretion in the northern Cordillera. Since folding and thrusting occurred over a relatively short four million year period, it is probable that these events are part of the same contractional deformation episode. Early ductile deformation was underway by 189 Ma and generated tight to overturned northeast-vergent folds in late Paleozoic volcanic-sedimentary successions of Yukon-Tanana/Quesnellia and miogeoclinal strata of North America. Shortening continued through the ductile-brittle transition at ca. 185 Ma or later resulting in the thrust emplacement of late Paleozoic-Mesozoic allochthonous arc terranes onto the ancient North American continental margin. This Early Jurassic accretionary event appears widespread in the northern Cordillera. The timing of arc terrane accretion constrained by our geochronological results (>189 to <185 Ma) is compatible with terrane interactions documented further south at Polaris (discussed below) and accords well with currently proposed geodynamic models for terrane accretion in the Cordillera (Nelson et al., 2013, Colpron et al., 2015, Pană et al., 2019).

TULAMEEN

The Late Triassic Tulameen ultramafic-mafic intrusion (60 km^2) is the largest Alaskan-type body in British Columbia. It is a classically zoned Alaskan-type intrusion with a dunite core zoned outwards to olivine clinopyroxenite and clinopyroxenite with hornblende clinopyroxenite and hornblendite at the margin (Findlay, 1963, 1969) (Fig. 3). The main mass of gabbroic and dioritic rocks occurs in the southeastern part of the intrusion. Contacts with metavolcanic and metasedimentary host rocks of the Upper Triassic Nicola Group are generally represented by ductile (mylonitic) or brittle fault zones; rafts of Nicola Group rocks within the Tulameen intrusion establish its original intrusive nature. Ongoing U-Pb zircon geochronology, by both LA-ICP-MS and CA-TIMS, indicates that most zircon crystallization ages for the Tulameen ultramafic-mafic suite fall in the range 204-206 Ma (latest Triassic) (Moerhuis et al., 2018), coincident with the most prolific Cu-Au porphyry mineralization epoch in British Columbia (Logan and Mihalynuk, 2014).

CU-FE-PGE MINERALIZATION

Isolated occurrences of Cu±Ag±Au±PGE mineralization in the Tulameen intrusion are recorded in the BC MINFILE database (minfile.gov.bc.ca). These showings are predominantly hosted by relatively evolved ultramafic lithologies (clinopyroxenite, hornblendite) near the periphery of the intrusion with a few occurrences hosted by heavily saussuritized gabbroic rocks (Fig. 3). The mineralization is described as potentially magmatic or as vestiges of alkalic Cu-Au porphyry mineralization. We have examined several of these showings in the least-altered ultramafic rocks and the mineralization is demonstrably magmatic (see descriptions of the Champion zone below). Similar mineralization

in altered gabbroic rocks may represent remobilized magmatic sulphides.

The Champion zone is a newly investigated occurrence of magmatic Cu-Fe sulphides variably enriched in PGE and located near the western margin of the Tulameen intrusion (Fig. 3). A 700 m-long zone of intermittent Cu-sulphide mineralization is exposed along a spur road overlooking Champion Creek, for which the showing is named (see Nixon, 2018 for detailed geology and access roads). Weak malachite staining betrays the presence of sparse amounts of sulphides (trace to ~2 vol. %) hosted by magnetite-bearing biotite-hornblende clinopyroxenite and hornblendite with minor, thin discontinuous layers of magnetitite.

The primary sulphide minerals are chalcopyrite ($CuFeS_2$) and bornite (Cu_5FeS_4) with minor pyrrhotite ($Fe_{1-x}S$); pyrite (FeS2) is locally abundant as a hydrothermal overprint replacing magmatic sulphides. Four principal textural groupings of sulphide minerals are recognized: 1) sulphide inclusions (<60 μm) within primary silicates and oxides; 2) primary sulphides occurring interstitially within the cumulate framework; 3) recrystallized interstitial sulphides; and 4) hydrothermal sulphides.

1) Chalcopyrite, bornite, minor pyrite and rare pyrrhotite are the primary inclusions in silicates and oxides (Fig. 4). Chalcopyrite commonly forms inclusions in hornblende, clinopyroxene and magnetite; pyrrhotite is confined to inclusions in clinopyroxene where it coexists with chalcopyrite. Bornite, exhibiting chalcopyrite exsolution lamellae, occurs as inclusions in hornblende and magnetite, and is locally accompanied by separate grains of chalcopyrite but does not coexist with pyrrhotite. The Cu-Fe sulphides commonly display well-developed rims of covellite (CuS) ± digenite (Cu9S5).
2) Chalcopyrite, and less commonly bornite, occur as primary interstitial sulphides (Fig. 5a-b). Alteration rims of covellite ± digenite, Fe-oxide/hydroxide and malachite are locally well developed. Rare vermicular intergrowths of bornite in a chalcopyrite host may indicate co-precipitation (Fig. 5b).
3) Interstitial sulphides, predominantly chalcopyrite, are locally recrystallized and intergrown with actinolite/actinolitic hornblende, epidote, chlorite, and secondary titanite (Fig. 5c). Sulphide morphologies are typically angular due to control by secondary silicate grain boundaries. Locally, sulphides are remobilized along microfractures and cleavage planes of primary silicates.
4) Late-stage hydrothermal pyrite locally occupies fractures and veinlets, and may form zones of more pervasive replacement of primary interstitial sulphides (Fig. 5d). Rarely, the more pervasive hydrothermal assemblages involve pyrite, chalcopyrite and pyrrhotite.

The sulphide textures and compositions described above evidently track a complex evolutionary history. Primary Cu-Fe sulphides appear to reflect delayed sulphide saturation in fractionating silicate melts where sulphide melts segregated, crystallized and cooled over a significant temperature interval. Pyrrhotite-chalcopyrite inclusions in clinopyroxene are inferred to represent the high-temperature end of this spectrum, and chalcopyrite-bornite inclusions in hornblende their low-temperature Cu-rich counterparts. The lack of Ni-rich magmatic sulphides is attributed to early depletion of nickel by olivine fractionation prior to the onset of sulphide immiscibility. Primary sulphides were locally recrystallized during upper greenschist-lower amphibolite facies metamorphism which post-dates emplacement and crystallization of the Tulameen intrusion. Desulphurization textures such as Fe-oxide rims on interstitial sulphides likely also formed during metamorphism along with localized pervasive zones of hydrothermal pyrite. Alteration rims of hydroxide and secondary Cu-rich minerals on primary sulphides are the product of oxidation and weathering. The primary sulphides are currently being analyzed for S isotopes to evaluate the role of wallrock contamination in their origin.

Despite the low modal abundance of Cu-Fe sulphides in the Champion zone, preliminary assays of grab (whole rock) samples yield up to 1.9 g/t Pd+Pt with Pd/Pt>1. These are the second highest bulk rock PGE abundances in the Tulameen intrusion, exceeded only by platiniferous chromitites in the dunite core that yield values up to 9.3 g/t Pt with Pt/Pd ~127 (Nixon et al., 1997) (Fig. 3). The Cu-rich nature of the low-volume sulphides and anomalous abundance of PGE in the Champion zone resemble mineralization in some Cu-PGE reefs in layered intrusions. For example, the sub-economic Platinova Reef in the Skaergaard layered intrusion (east Greenland) has an estimated resource of 23 Mt at 2.3 g/t Au, 0.7 g/t Pd and 0.1 g/t Pt (contained metal 1.7 Moz Au, 0.5 Moz Pd and 0.04 Moz Pt) at a cut-off grade of 1.5 g/t Au equivalent (Holwell and Keays, 2014; Holwell et al., 2015). Current research is focused on characterizing the mineralogical and geochemical attributes of the Cu-Pd-Pt mineralization in the Champion zone, and the timing of mineralization within the magmatic and temporal evolution of the Tulameen intrusive suite.

POLARIS

The Early Jurassic Polaris ultramafic-mafic intrusion (45 km^2) is one of the largest and best exposed Alaskan-type intrusions in British Columbia. The Polaris intrusion is situated at the eastern edge of the Quesnellia arc terrane where it is juxtaposed with miogeoclinal strata of ancestral North America, a structural setting analogous to that of Turnagain described above (Fig. 1). Previous studies of Polaris include the pioneering work of Roots (1954); internal subdivision of the ultramafic-mafic rock units by Irvine (1974), who first recognized an Alaskan-type affinity; and subsequent mapping by Nixon et al. (1997).

The Polaris intrusion was emplaced into Upper Paleozoic (Mississippian to Permian) metasedimentary and metavolcanic strata of the Lay Range assemblage that forms the

"basement" to Mesozoic Quesnellia in this part of British Columbia and is equivalent to the Harper Ranch subterrane in the southern part of the province (Fig. 6). Nixon et al. (1997) reported a $^{206}Pb/^{238}U$ (air-abraded) zircon crystallization age of 186 ± 2 Ma (Pliensbachian, late Early Jurassic) from a feldspathic pegmatite segregation in dioritic rocks near the western contact of the intrusion. Zircons from the same separate were recently re-analyzed using high-precision, chemical abrasion ID-TIMS U-Pb geochronological techniques at PCIGR and yielded a significantly more precise $^{206}Pb/^{238}U$ zircon crystallization age of 186.26 ± 0.14 Ma. Emplacement and crystallization of the Polaris intrusion ca. 186 Ma appears to coincide with eastward-directed ductile thrusting of the intrusion and its host rocks onto the North American miogeocline (Nixon et al., 1997, 2019). As noted above, this Early Jurassic contractional event is well-documented at Turnagain and appears widespread in the northern Cordillera. It marks the accretion of outboard arc terranes (Quesnellia/Yukon-Tanana) to the ancient continental margin of North America (Nixon et al., 2019).

Recently initiated research at Polaris is investigating the timing of magmatic sulphide mineralization relative to accretionary events and assembly of the intrusion as a whole, and the mineralogy and composition of the sulphides. Unlike Tulameen, which exhibits classical concentric zoning of ultramafic lithologies, Polaris has a distinctly asymmetric zoning pattern. Olivine-rich lithologies (dunite and wehrlite) are prevalent in the east, whereas hornblende-bearing ultramafic rocks and gabbro/diorite are concentrated in the west-central part of the intrusion (Fig. 6). Known sulphide occurrences are hosted mainly by hornblende clinopyroxenite and gabbro/diorite with some mineralization occurring in wehrlite in the central part of the intrusion (Fig. 6). The principal sulphide minerals identified to date are pyrrhotite, chalcopyrite, pyrite and minor bornite. The sulphides generally occur in low modal proportions as fine disseminations. Preliminary microscopy reveals predominantly interstitial sulphides with some occurring as inclusions in clinopyroxene and hornblende. Assay results from grab samples reported from mineral claims on the Polaris intrusion show up to 0.77 wt.% Cu, 1.8 g/t Pd and 1.3 g/t Pt (Mowat 2015). Future investigations will more fully characterize the mineralogical and geochemical attributes of these sulphide occurrences.

FUTURE RESEARCH

U-Pb geochronology, petrography and geochemical analysis is continuing for samples collected from Cu-PGE sulphide mineralization in the Champion zone at Tulameen. James Nott is conducting TGI-funded MSc research and Dylan Spence a directed studies project, both on the Polaris Alaskan-type intrusion, at the University of British Columbia under the supervision of Dr. James Scoates. Fieldwork at Polaris this summer will involve targeted geological mapping and collection of samples for petrography, geochemistry and U-Pb geochronology.

ACKNOWLEDGMENTS

This report is a contribution to NRCan's Targeted Geoscience Initiative Program (TGI-5). Support for this ongoing study is provided by the Ni-Cu-PGE-Cr subprogram's 'Convergent margin Ni-Cu-PGE-Cr ore systems: temporal and magmatic evolution' project; the British Columbia Geological Survey; and NSERC Discovery Grant to James Scoates. Research activity at Turnagain was supported in part by Hard Creek Nickel Corporation (now Giga Metals Corporation) through the offices of Mark Jarvis, President. We gratefully acknowledge company geologists for facilitating access to drill core, proprietary data and fruitful discussions, in particular Tony Hitchins, Chris Baldys, Bruce Northcote and Greg Ross. We thank Ursula Mowat for providing a small suite of sulphide-bearing samples from her claims on Polaris. We thank Matt Manor, Tom Ver Hoeve, and Nichole Moerhuis for assisting in research efforts on the Tulameen intrusion. This report has benefited from a review by Neil Rogers.

REFERENCES

Clark, T.
1975: Geology of an ultramafic complex on the Turnagain River, northwestern British Columbia; Ph.D. thesis, Queen's University, Kingston, Ontario, 453 p.

Clark, T.
1978: Oxide minerals in the Turnagain ultramafic complex, northwestern British Columbia; Canadian Journal of Earth Sciences, v. 15, p. 1893–1903.

Clark, T.
1980: Petrology of the Turnagain ultramafic complex, northwestern British Columbia; Canadian Journal of Earth Sciences, v. 17, p. 744–757.

Colpron, M., Crowley, J.L., Gehrels, G., Long, D.G.F., Murphy, D.C., Beranek, L., and Bickerton, L.
2015: Birth of the northern Cordilleran orogen, as recorded by detrital zircons in Jurassic synorogenic strata and regional exhumation in Yukon; Lithosphere, v. 7, p. 541–562.

Colpron, M., and Nelson, J.L.
2011: A digital atlas of terranes for the Northern Cordillera; British Columbia Ministry of Energy and Mines, British Columbia Geological Survey Geofile, 2011–11.

Erdmer, P., Mihalynuk, M.G., Gabrielse, H., Heaman, L.M., and Creaser, R.A.
2005: Mississippian volcanic assemblage conformably overlying Cordilleran miogeoclinal strata, Turnagain River area, northern British Columbia, is not part of an accreted terrane; Canadian Journal of Earth Sciences, v. 42, p. 1449–1465.

Findlay, D.C.
1963: Petrology of the Tulameen ultramafic complex, Yale District, British Columbia; PhD thesis, Queen's University, Kingston, Ontario, 415 p.

Findlay, D.C.
1969: Origin of the Tulameen ultramafic-gabbro complex, southern British Columbia; Canadian Journal of Earth Sciences, v. 6, p. 399–425.

Gabrielse, H.
1985: Major dextral transcurrent displacements along the Northern Rocky Mountain Trench and related lineaments in north-central British Columbia; Geological Society of America Bulletin, v. 96, p. 1–14.

Himmelberg, G.R., and Loney, R.A.
1995: Characteristics and petrogenesis of Alaskan-type ultramafic-mafic intrusions, southeastern Alaska; U.S. Geological Survey Professional Paper, 1564, 47 p.

Hodges, K.V.
2014: Thermochronology in orogenic systems; in Treatise on Geochemistry (Second Edition), (ed.) H.D.H.K. Turekian, Elsevier, Oxford, p. 281–308.

Holwell, D.A., and Keays, R.R.
2014: The formation of low-volume, high-tenor magmatic PGE-Au sulfide mineralization in closed systems: evidence from precious and base metal geochemistry of the Platinova Reef, Skaergaard intrusion, East Greenland; Economic Geology, v. 109, p. 387–406.

Holwell, D.A., Keays, R.R., McDonald, I., and Williams, M.R.
2015: Extreme enrichment of Se, Te, PGE and Au in Cu sulfide microdroplets: evidence from LA-ICP-MS analysis of sulfides in the Skaergaard intrusion, East Greenland; Contributions to Mineralogy and Petrology, v. 170, 53, doi:10.1007/s00410-015-1203-y.

Irvine, T.N.
1974: Ultramafic and gabbroic rocks in the Aiken Lake and McConnell Creek map-areas, British Columbia; Geological Survey of Canada, Paper 74–1A, p. 149–152.

Jackson-Brown, S.
2017: Origin of the Cu-PGE-rich sulphide mineralization in the DJ/DB zone of the Turnagain Alaskan-type intrusion, British Columbia; MSc thesis, University of British Columbia, Vancouver, British Columbia, 290 p.

Johan, Z.
2002: Alaskan-type complexes and their platinum-group-element mineralization; in The Geology, Geochemistry, Mineralogy and Mineral Beneficiation of Platinum-Group Elements, (ed.) L.J. Cabri, Canadian Institute of Mining, Metallurgy and Petroleum, Special Volume 54, p. 669–719.

Li, C., Zhang, Z., Li, W., Wang, Y., Sun, T., and Ripley, E.M.
2015: Geochronology, petrology and Hf-S isotope geochemistry of the newly-discovered Xiarihamu magmatic Ni-Cu sulfide deposit in the Qinghai–Tibet plateau, western China; Lithos, v. 216–217, p. 224–240.

Logan, J.M. and Mihalynuk, M.G.
2014: Tectonic controls on Early Mesozoic paired alkaline porphyry belts (Cu-Au ±Ag-Pt-Pd-Mo) within the Canadian Cordillera; Economic Geology, v. 109, p. 827-858.

Manor, M.J., Scoates, J.S., Nixon, G.T., and Ames, D.E.
2016: The Giant Mascot Ni-Cu-PGE deposit, British Columbia: mineralized conduits in a convergent margin tectonic setting; Economic Geology, v. 111, p. 57–87.

Manor, M.J., Scoates, J.S., Wall, C.J., Nixon, G.T., Friedman, R.M., Amini, M., and Ames, D.E.
2017: Age of the Late Cretaceous ultramafic-hosted Giant Mascot Ni-Cu-PGE deposit, southern Canadian Cordillera: integrating CA-ID-TIMS and LA-ICP-MS U-Pb geochronology and trace element geochemistry of zircon; Economic Geology, v. 112, p. 1395–1418.

Moerhuis, N., Ver Hoeve, T.J., Scoates, J.S., Nixon, G.T., Friedman, R.M., and Manor, M.J.
2018: New perspectives on the timescales of emplacement and crystallization of ultramafic rocks from integrated CA-ID-TIMS and LA-ICP-MS U-Pb geochronology. Resources for Future Generation Meeting, Vancouver, BC, June 16-21, 2018 [abstract].

Mowat, U.
2015: Sampling on the Star 1, 3, 8, 10, 11 and 12 claims; British Columbia Assessment Report 35680, Victoria, British Columbia, 88 p.

Mudd, G.M., and Jowitt, S.M.
2014: A detailed assessment of global nickel resource trends and endowments; Economic Geology, v. 109, p. 1813–1841.

Naldrett, A.J.
2010: Secular variation of magmatic sulfide deposits and their source magmas; Economic Geology, v. 105, p. 669–688.

Nelson, J.L., Colpron, M., and Israel, S.
2013: The Cordillera of British Columbia, Yukon and Alaska: tectonics and metallogeny; in Tectonics, Metallogeny, and Discovery: The North American Cordillera and Similar Accretionary Settings; (Ed.) M. Colpron, T. Bissig, B.J. Rusk, and J.F.H. Thompson, Society of Economic Geologists Special Publication 17, p. 53–109.

Nelson, J.L., Colpron, M., Piercey, S.J., Dusel-Bacon, C., Murphy, D.C., and Roots, C.F.
2006: Paleozoic tectonic and metallogenetic evolution of pericratonic terranes in Yukon, northern British Columbia and eastern Alaska; in Paleozoic Evolution and Metallogeny of Pericratonic Terranes at the Ancient Pacific Margin of North America, Canadian and Alaskan Cordillera, (ed.) M. Colpron and J.L. Nelson, Geological Association of Canada Special Paper 45, p. 323–360.

Nixon, G.T., Ash, C.A., Connelly, J.N., and Case, G.
1989: Geology and noble metal geochemistry of the Turnagain ultramafic complex, northern British Columbia; British Columbia Ministry of Energy, Mines and Petroleum Resources, British Columbia Geological Survey Open File 1989-19, scale 1:16 000.

Nixon, G.T., Cabri, L.J., and Laflamme, J.H.G.
1990: Platinum-group-element mineralization in lode and placer deposits associated with the Tulameen Alaskan-type complex, British-Columbia; Canadian Mineralogist, v. 28, p. 503–535.

Nixon, G.T.,
2018: Geology of the Tulameen Alaskan-type ultramafic-mafic intrusion, British Columbia; British Columbia Ministry of Energy, Mines and Petroleum Resources, British Columbia Geological Survey Open File 2018-2, scale 1:20 000.

Nixon, G.T., Hammack, J.L., Ash, C.A., Cabri, L.J., Case, G., Connelly, J.N., Heaman, L.M., Laflamme, J.H.G., Nuttall, C., Paterson, W.P.E., and Wong, R.H.
1997: Geology and platinum-group-element mineralization of Alaskan-type ultramafic-mafic complexes in British Columbia; British Columbia Ministry of Employment and Investment, British Columbia Geological Survey Bulletin 93, 141.

Nixon, G.T., Manor, M.J., Jackson-Brown, S., Scoates, J.S., and Ames, D.E.
2015: Magmatic Ni-Cu-PGE sulphide deposits at convergent margins; in Targeted Geoscience Initiative -: Canadian Nickel-Copper-Platinum Group Elements-Chromium Ore Systems - Fertility, Pathfinders, New and Revised Models, (ed.) D.E. Ames and M.G. Houlé, Geological Survey of Canada, Open File 7856, p. 17–34.

Nixon, G.T., Manor, M.J., and Scoates, J.S.
2018: Cu-PGE sulphide mineralization in the Tulameen Alaskan-type intrusion: analogue for Cu-PGE reef mineralization in layered intrusions? British Columbia Ministry of Energy, Mines and Petroleum Resources, British Columbia Geological Survey Geofile 2018-2.

Nixon, G.T., Scheel, J.E., Friedman, R.M., Wall, C.J., Gabites, J., Miller, D., and Scoates, J.S.
2017: Geology and geochronology of the Turnagain ultramafic-mafic intrusion, British Columbia; British Columbia Ministry of Energy and Mines, British Columbia Geological Survey Geoscience Map 2017-1, scale 1:10 000.

Nixon, G.T., Scheel, J.E., Scoates, J.S., Friedman, R.M., Wall, C.J., Gabites, J., and Jackson-Brown, S.
2019: Syn-accretionary assembly of an Alaskan-type intrusion in the Canadian Cordillera: U-Pb and $^{40}Ar/^{39}Ar$ geochronology of the Early Jurassic Turnagain ultramafic-mafic intrusive complex, British Columbia; Canadian Journal of Earth Sciences (submitted).

Pană, D.I., Poulton, T.P., and DuFrane, S.A.
2019: U-Pb detrital zircon dating supports Early Jurassic initiation of the Cordilleran foreland basin in southwestern Canada; Geological Society of America Bulletin, v. 131, p. 318–334.

Piña, R.
2019: The Ni-Cu-(PGE) Aguablanca ore deposit (SW Spain). Springer International Publishing, 74 p., doi:10.1007/978-3-319-93154-8.

Roots, E.F.
1954: Geology and mineral deposits of Aiken Lake map-area, British Columbia; Geological Survey of Canada, Memoir 274, 246 p.

Scheel, J.E.
2007: Age and origin of the Turnagain Alaskan-type intrusion and associated Ni-sulphide mineralization, north-central British Columbia, Canada; M.Sc. thesis, University of British Columbia, Vancouver, British Columbia, 210 p.

Scheel, J.E., Scoates, J.S., and Nixon, G.T.
2009: Chromian spinel in the Turnagain Alaskan-type ultramafic intrusion, northern British Columbia, Canada; Canadian Mineralogist, v. 47, p. 63–80.

Song, X.-Y., Yi, J.-N., Chen, L.-M., She, Y.-W., Liu, C.-Z., Dang, X.-Y., Yang, Q.-A., and Wu, S.-K.
2016: The giant Xiarihamu Ni-Co sulfide deposit in the East Kunlun Orogenic Belt, northern Tibet Plateau, China; Economic Geology, v. 111, p. 29–55.

Weiser, T.W.
2002: Platinum-group minerals (PGM) in placer deposits; in The Geology, Geochemistry, Mineralogy and Mineral Beneficiation of Platinum-Group Elements, (ed.) L.J. Cabri, Canadian Institute of Mining, Metallurgy and Petroleum, Special Volume 54, p. 721–756.

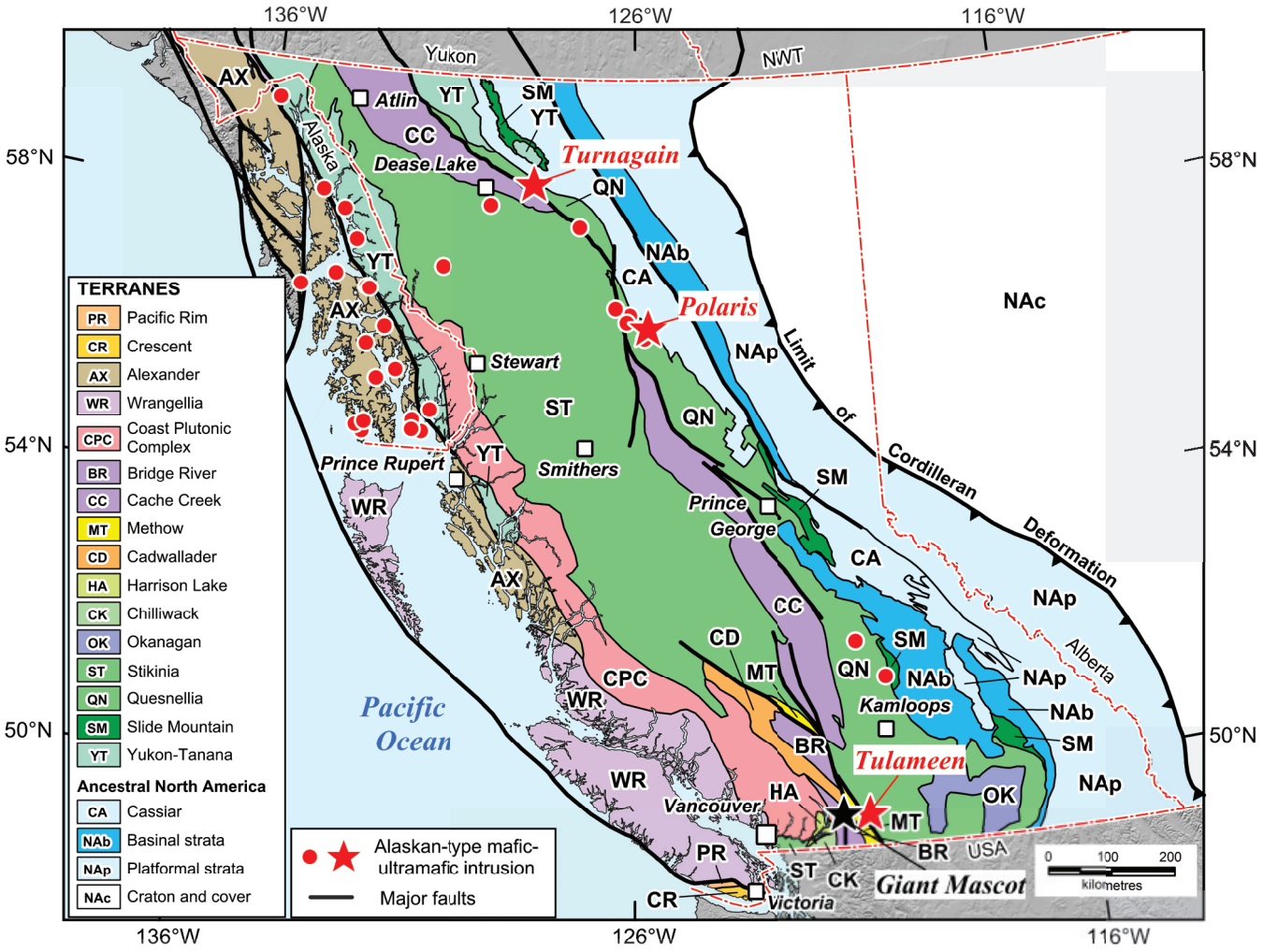

Figure 1. Terrane map of British Columbia and southeastern Alaska (after Colpron and Nelson, 2011) showing the distribution of Alaskan-type intrusions (after Himmelberg and Loney, 1995; Nixon et al., 1997). Current research on the Turnagain, Polaris, and Tulameen Alaskan-type intrusions is documented in this report. The Late Cretaceous Giant Mascot ultramafic-mafic intrusion and Ni-Cu-PGE deposit, the subject of previous TGI studies (Manor et al., 2016, 2017), is shown for reference.

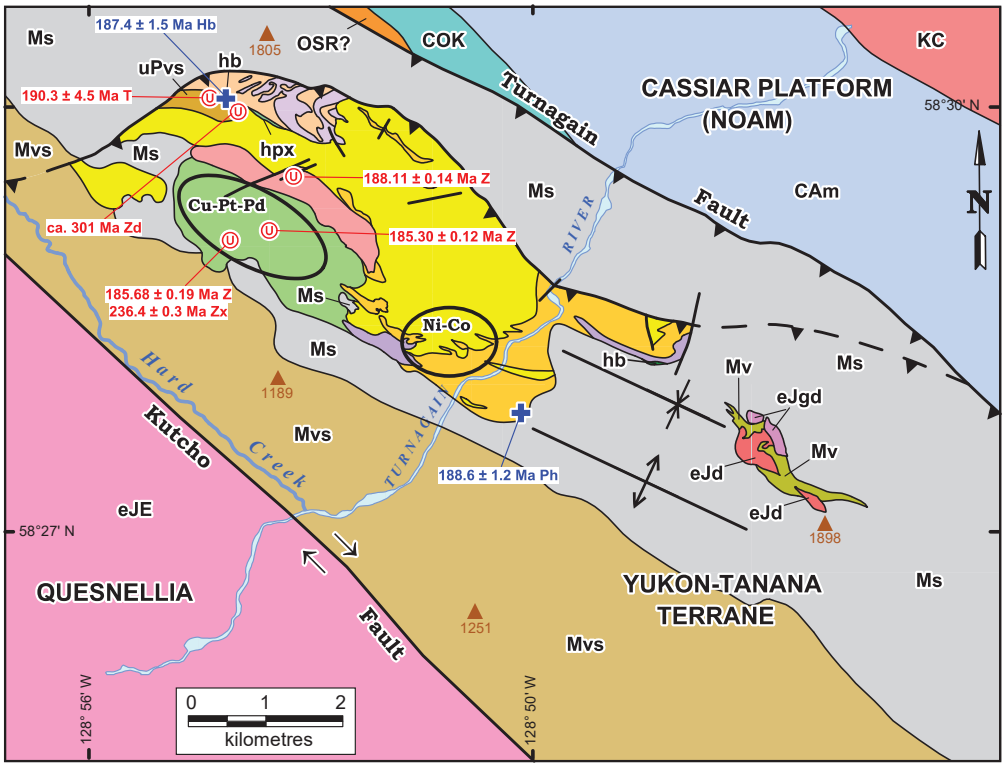

Quesnellia Terrane

Early Jurassic

eJE — Eaglehead Pluton: biotite-hornblende quartz monzonite, granodiorite and quartz diorite

Yukon-Tanana Terrane

Early Jurassic

Turnagain Ultramafic-Mafic Intrusion

Intrusive Stage 4

hornblende clinopyroxenite, magnetite±biotite clinopyroxenite, hornblendite, minor wehrlite

Intrusive Stage 3

hornblende diorite and minor feldspathic hornblendite, quartz diorite, granodiorite and tonalite

Intrusive Stage 2

hb — thin marginal hornblendite, locally pegmatitic

hpx — thin marginal hornblende clinopyroxenite and minor clinopyroxenite, locally pegmatitic

clinopyroxenite, locally pegmatitic

wehrlite, minor dunite, olivine clinopyroxenite, clinopyroxenite; clinopyroxenite dykes

dunite, minor chromitite, wehrlite, olivine clinopyroxenite, clinopyroxenite; clinopyroxenite dykes

Intrusive Stage 1

olivine clinopyroxenite, locally pegmatitic

wehrlite, minor dunite, olivine clinopyroxenite; clinopyroxenite dykes

Early Jurassic

eJgd — granodiorite

eJd — diorite

Geological contact

Fault, steeply dipping

CARBONIFEROUS

Upper Pennsylvanian (or younger?)

uPvs — volcanic wacke and phyllite

Mississippian (and younger?)

Mvs — mafic to felsic volcanic/volcaniclastic and sedimentary rocks, phyllite, argillite, chert, quartz-sericite schist and marble

Mississippian

Mv — tuff, tuffaceous phyllite, minor wacke, limestone and rare graphitic phyllite

Ms — graphitic/pyritic phyllite and slate, minor wacke and limestone

Cassiar Platform (NOAM)

Cretaceous

KC — Cassiar Batholith: biotite-hornblende granite, granodiorite and quartz monzonite

Lower Ordovician to Silurian

OSR? — Road River Formation(?): siltstone, pyritic and calcareous shale, slate and phyllite

Upper Cambrian to Lower Ordovician

COK — Kechika Formation: argillaceous limestone and calcareous shale

LOWER CAMBRIAN

CAm — Atan Group: micaceous quartzite, mica schist, siltstone and minor marble

Fault, strike-slip, dextral

Fault, contractional (teeth on upper plate)

Trace of anticline/syncline

185.30 ± 0.12 Ma — U-Pb date (± 2 sigma); Z zircon; T titanite; d detrital; x xenocrysts

188.6 ± 1.2 Ma — $^{40}Ar/^{39}Ar$ date (± 2 sigma); Hb hornblende; Ph phlogopite

Spot height (metres)

Figure 2. Generalized geology of the Turnagain ultramafic-mafic intrusion (after Nixon et al., 2017) showing the regional geology, intrusive stages, U-Pb and 40Ar/39Ar geochronological results (Nixon et al., 2019). Black ellipsoids indicate the area of the main Ni(-Co-PGE) resource (Horsetrail zone; Scheel, 2007) and Cu-PGE mineralization (DJ/DB zone; Jackson-Brown, 2017).

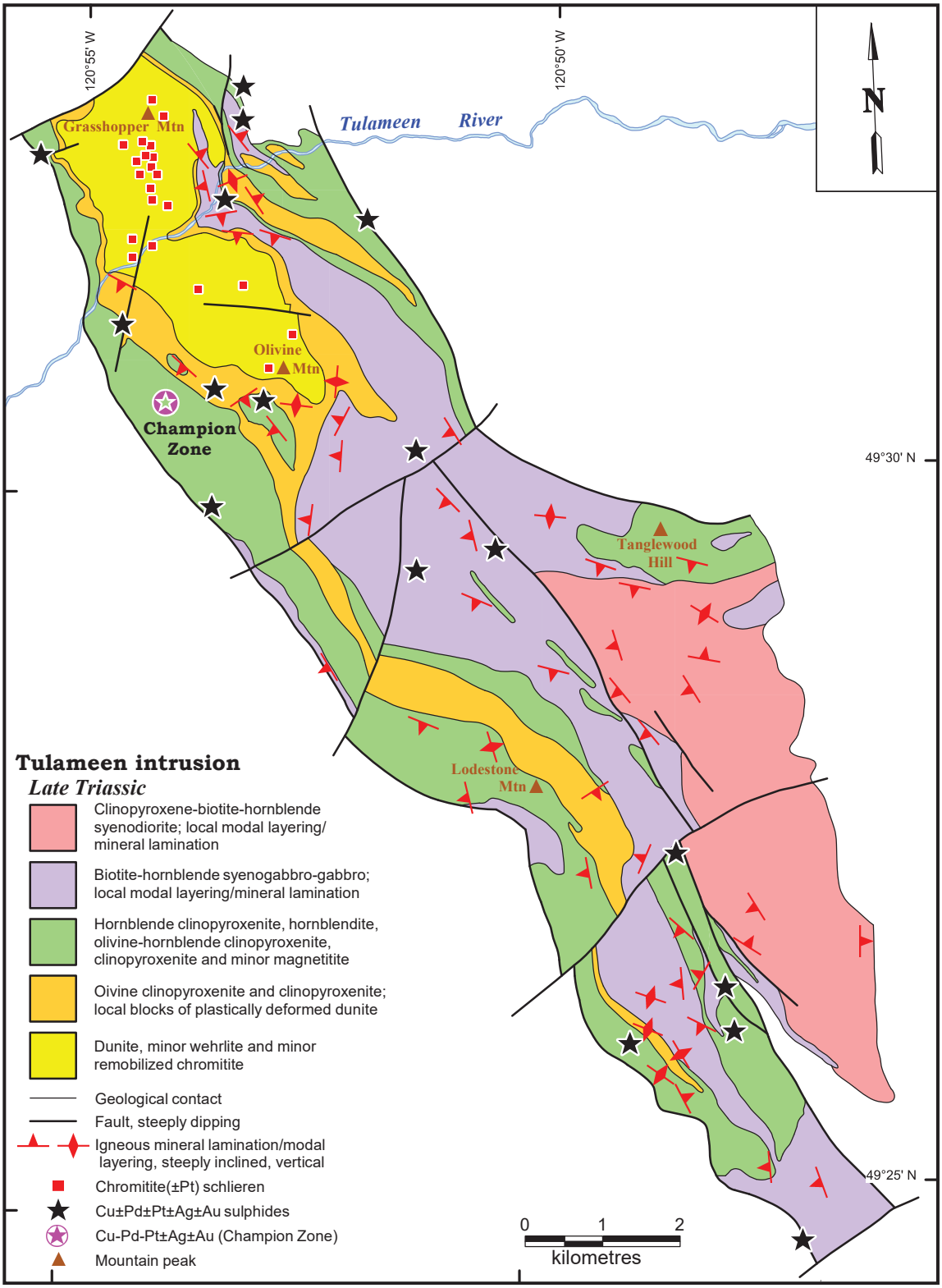

Figure 3. Generalized geology of the Tulameen Alaskan-type intrusion showing chromitite (±PGE) localities in the dunite core (Nixon et al., 1997; Nixon, 2018) and Cu±PGE±Ag±Au sulphide occurrences including the recently investigated Cu-Pd-Pt Champion zone (Nixon et al., 2018).

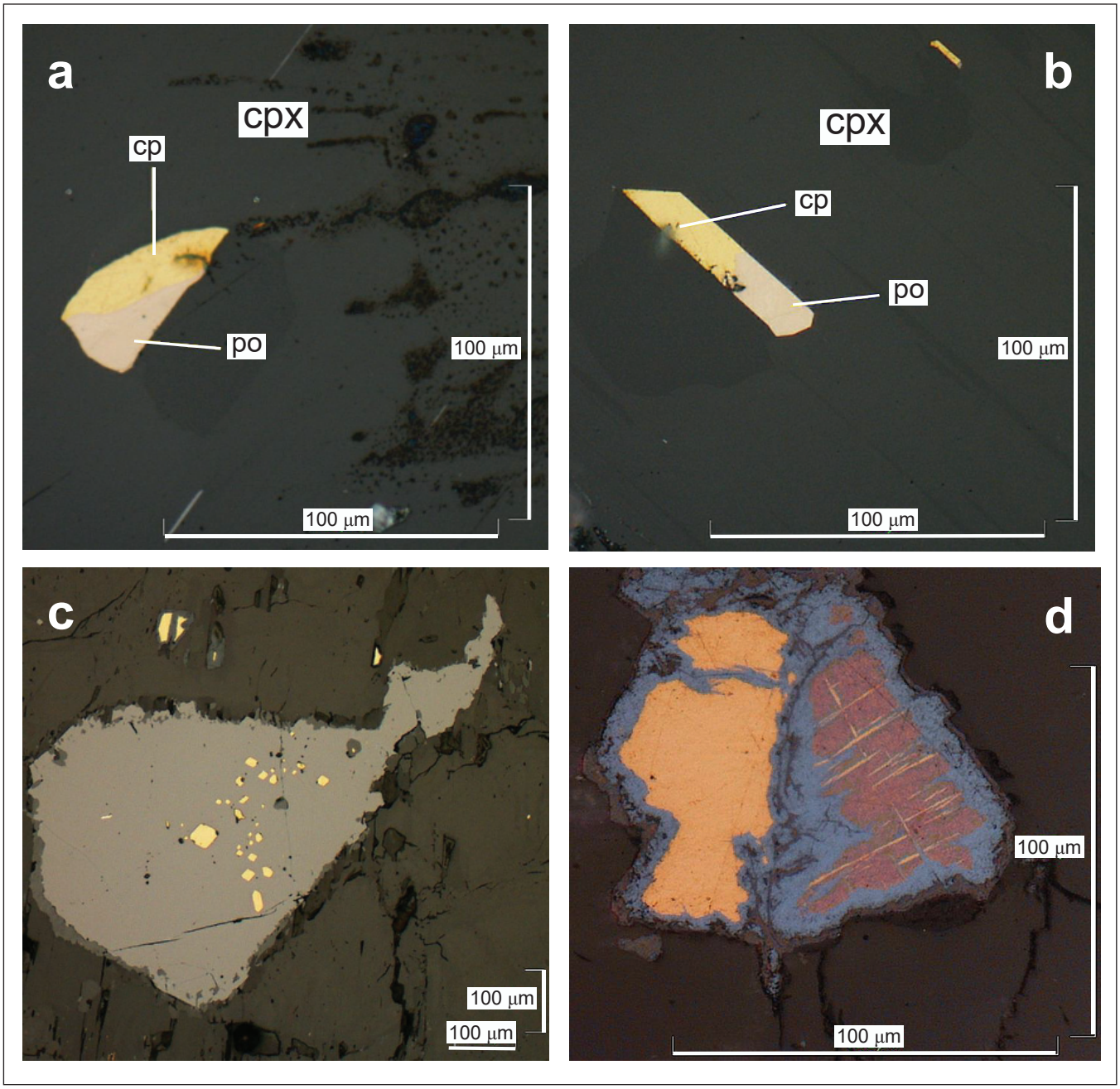

Figure 4. Photomicrographs showing sulphide inclusions in ultramafic rocks of the Champion zone: a) composite inclusion of chalcopyrite(cp)-pyrrhotite(po) in clinopyroxene (cpx) (hornblende-magnetite clinopyroxenite); b) faceted inclusion of chalcopyrite(cp)-pyrrhotite(po) in clinopyroxene (hornblende-magnetite clinopyroxenite); c) swarm of chalcopyrite inclusions in interstitial magnetite (magnetite-hornblende clinopyroxenite); d) composite inclusion of chalcopyrite-bornite in hornblende showing well-developed chalcopyrite exsolution lamellae in bornite and covellite rim (magnetite-hornblende clinopyroxenite). All photomicrographs in reflected light; scale bar is 100 µm.

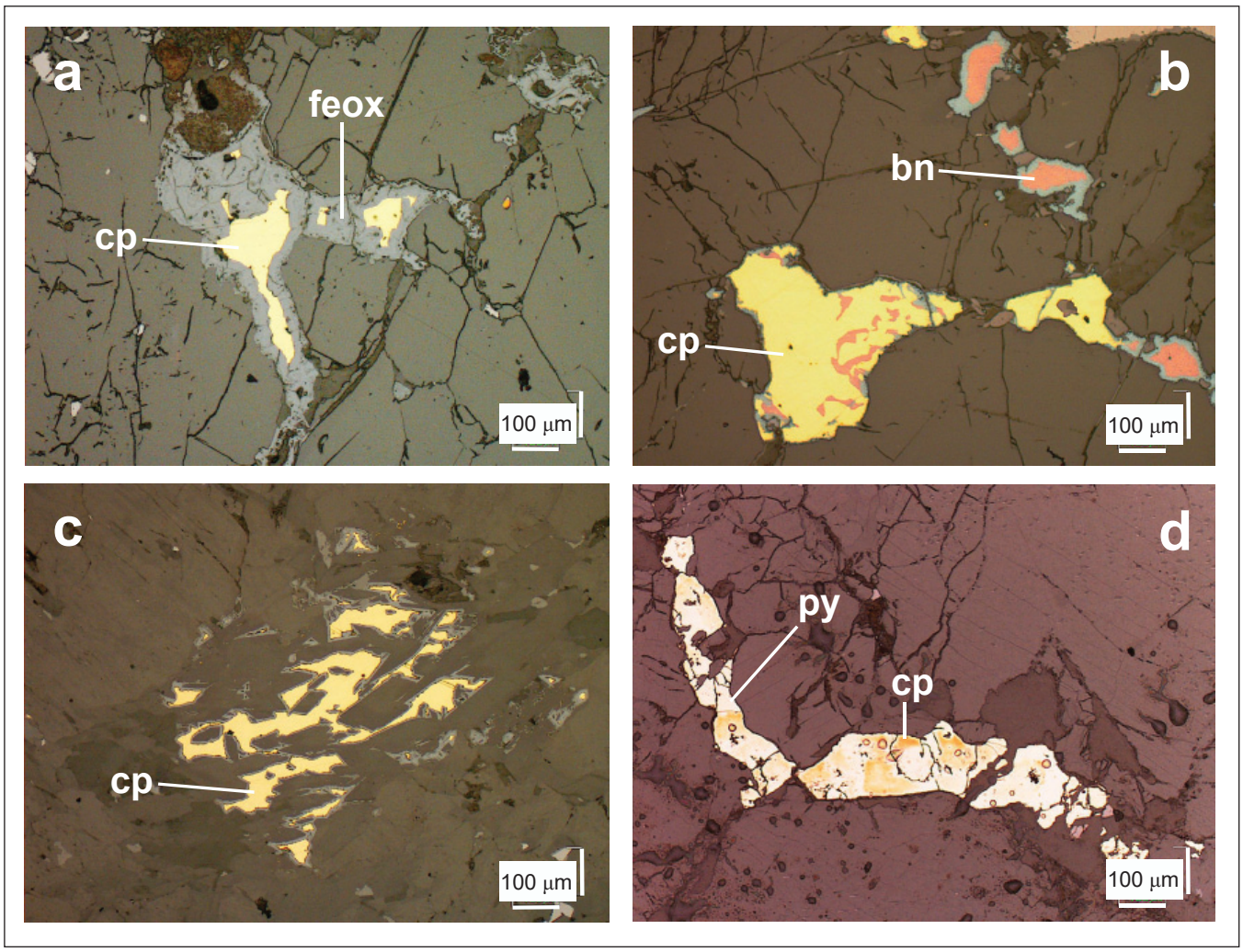

Figure 5. Photomicrographs showing interstitial sulphides in ultramafic rocks of the Champion zone: a) primary chalcopyrite(cp) with well-developed rim of magnetite-goethite(feox) (magnetite-hornblendite); b) interstitial bornite(bn) with well-developed covellite rim and myrmekitic bornite in chalcopyrite(cp) (magnetite hornblendite); c) recrystallized chalcopyrite(cp) partly replaced by/intergrown with actinolite/actinolitic hornblende (hornblende clinopyroxenite); d) interstitial hydrothermal pyrite(py) replacing chalcopyrite(cp) still visible as yellow relict grains (hornblende-magnetite clinopyroxenite). All photomicrographs in reflected light; scale bar is 100 μm.

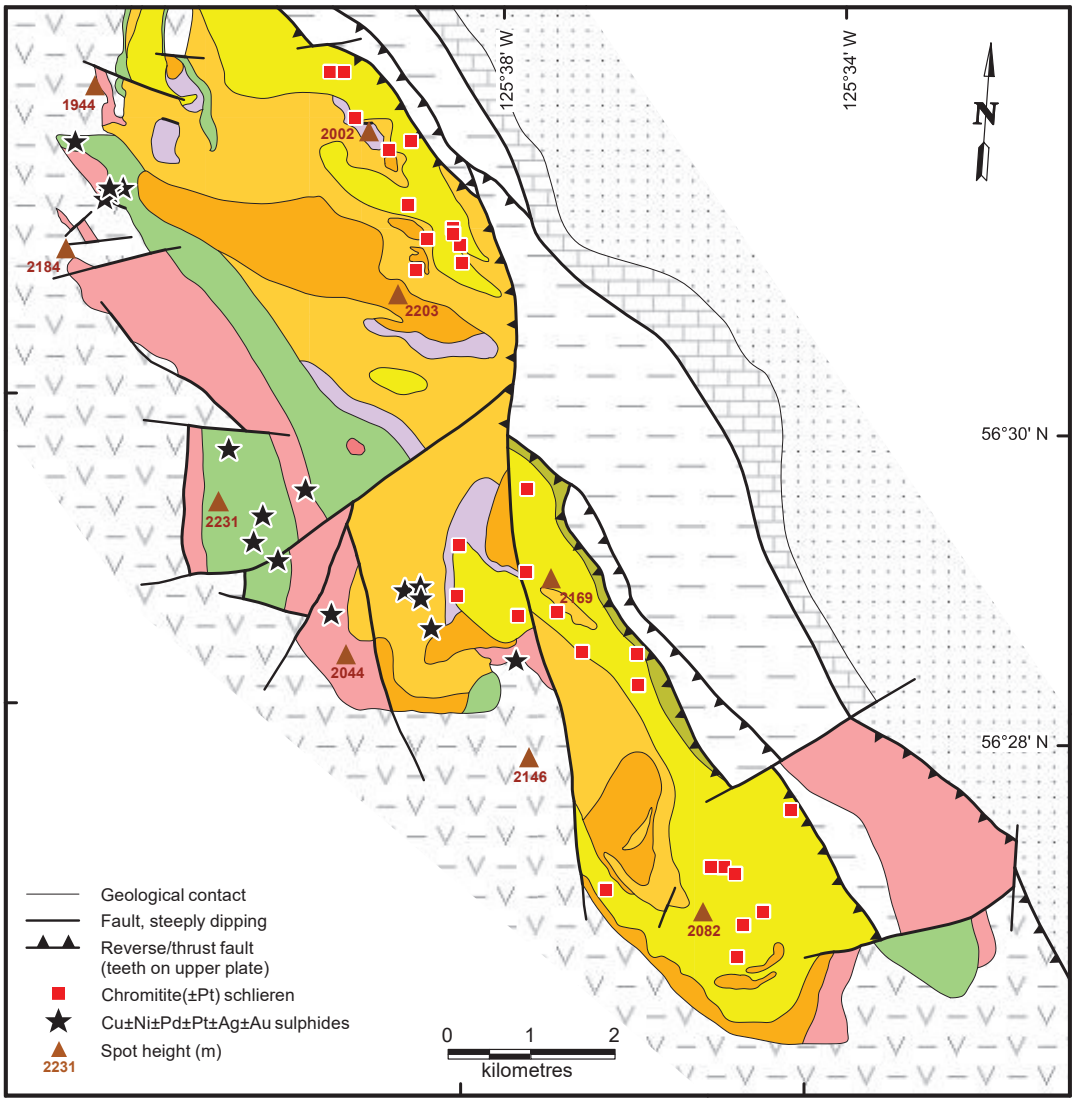

Late Triassic

Polaris intrusion

- Syenite-leucomonzonite minor intrusions and dykes, locally pegmatitic
- Hornblende diorite/gabbro and minor feldspathic hornblendite
- Hornblende clinopyroxenite and minor olivine-hornblende clinopyroxenite, hornblendite/feldspathic hornblendite
- Wehrlite zoned outward to olivine clinopyroxenite and hornblende clinopyroxenite/hornblendite
- Olivine clinopyroxenite and clinopyroxenite
- Wehrlite and minor olivine clinopyroxenite
- Ultramafic rocks, undifferentiated, chaotically mixed
- Dunite, minor wehrlite and remobilized chromitite

Paleozoic

Lay Range Assemblage

Mississippian to Permian

- Metasedimentary and metavolcanic rocks with subvolcanic intrusions; hornfelsed near Polaris contacts

Big Creek Group

Upper Devonian to Lower Mississippian

- Metasedimentary rocks and minor felsic tuff

Cambrian to Devonian

- Undifferentiated metasedimentary rocks of the Atan, Razor Back, Echo Lake and Otter Lakes Groups

Upper Proterozoic

Ingenika Group

- Metamorphosed sedimentary rocks

Figure 6. Generalized geology of the Polaris ultramafic-mafic Alaskan-type intrusion showing chromitite (±PGE) and known magmatic sulphide occurrences (modified from Nixon et al., 1997).

Genesis of Orogenic Gold in SE Yukon: linking metamorphic fluid generation with gold and trace element mobility at the pyrite-pyrrhotite transition

C.D.W. Padget[1], D.R.M. Pattison1, D.P. Moynihan[2]

INTRODUCTION

Orogenic gold deposits (Bohlke, 1982) are a group of gold-bearing quartz and quartz-carbonate vein-type deposits typically hosted in low-grade (greenschist facies) metamorphic rocks. These deposits are among the most common source of gold in Canada and account for a significant proportion of global historic gold production. Though a unified model for the genesis of these deposits has yet to be agreed upon, the most widely accepted model for the source of mineralizing fluids is metamorphic dehydration reactions (e.g., Cox et al., 1991; Goldfarb & Groves, 2015; Phillips & Powell, 2010; Tomkins, 2010, and many others). Likewise, the source of the metal in these systems is contested. A growing body of evidence, however, suggests pyrite may play a key role both as a significant metal host (Large et al., 2009, 2011) and as a source of sulfur to the fluid through the breakdown of pyrite to pyrrhotite (py-po) during prograde metamorphism (Toulmin and Barton, 1964; Zhong et al., 2015).

The suggested components of an ideal geologic setting for the genesis of orogenic gold deposits via the metamorphic devolitization model include: (1) a thick sequence of sedimentary or volcanic rocks with abundant intervals of carbonaceous shales, and (2) a compressional or transpressional tectonic environment leading to low pressure/high-temperature amphibolite facies metamorphism (<~5kbar,>~550°C). Carbonaceous shales commonly host diagenetic pyrite that typically contains trace quantities of gold, and it has been shown that such rocks contain greater concentrations of gold than other sedimentary or igneous rocks (Large et al., 2011; Tomkins, 2010, and references therein). This gold is then scavenged by metamorphic fluids following or concurrent with pyrite breakdown to pyrrhotite by the reaction:

$$FeS^2(\text{pyrite}) + H^2O = FeS(\text{pyrrhotite}) + H^2S(aq) + ½\ O^2(aq) \quad (1)$$

The release of sulphur accompanying this transition is important for gold dissolution and transport because gold is most commonly transported by HS- complexes in low-salinity, mixed H^2O-CO^2 metamorphic fluids (Phillips and Powell, 2010). Such fluids are generated most voluminously at the greenschist-amphibolite facies transition where chlorite reacts out of the rock to generate metamorphic porphyroblasts such as garnet and staurolite in metapelites, and hornblende in metabasites. This fluid release facilitates the operation of reaction (1), thereby promoting the generation of fluid with compositions best suited to scavenge and transport gold and other metals.

A compressional or transpressional tectonic setting is favourable for generating the requisite metamorphic conditions common to these deposits. These settings also promote extensive fluid circulation and the generation of large-scale fault systems, which act as pathways necessary for the efficient transport of metamorphic fluids laden with Au and other metals (Sibson et al., 1988; Tomkins, 2010). Some have argued these fluids may be episodically released and brought toward surface during seismic episodes (e.g., Cox et al., 1991). Rapid ascent takes the fluid out of equilibrium with its source rocks and is one potential mechanism for the precipitation of gold in these deposits (Tomkins, 2013). Another mechanism is chemical interaction with host rocks, and possibly fluids, of different composition to the source rocks (e.g., carbonates, iron formation), leading to precipitation (Goldfarb et al., 2005).

This TGI-5 project aims to investigate the source of metals and fluids associated with orogenic gold-type mineralization in the Hyland River region of southeastern Yukon. Two focus areas are the relative positions of (1) the pyrite to pyrrhotite transition and (2) the breakdown of hydrous minerals (e.g., clays, chlorite, micas) that result in fluid generation. The Hyland River region has been chosen as a natural laboratory for this investigation as it meets the geological conditions enumerated above and hosts numerous Au occurrences with features characteristic of orogenic gold-type mineralization.

REGIONAL SETTING

The Hyland River region is a geologically complex portion the Selwyn fold and thrust belt in the northern Canadian Cordillera (fig. 1). The area is underlain by variably

[1]Department of Earth Sciences, University of Calgary, 2500 University Drive NW, Calgary, Alberta T2N 1N4
[2]Yukon Geological Survey, 91807 Alaska Hwy, Whitehorse, Yukon Y1A 0R3

deformed and metamorphosed rocks of the Neoproterozoic to Paleozoic Hyland Group (Gordey and Anderson, 1993) which consists of a thick package of mixed-clastic and lesser carbonate rocks. It represents the upper portion of the Windermere Supergroup, a Neoproterozoic succession of predominantly deep marine sedimentary and volcanic rocks deposited along the western Laurentian margin in an extensional setting. To the east, the Hyland Group is overlain by shales, basinal limestones, sandstones, and grits representing the transitional slope-to-shelf environment at the eastern margin of Selwyn Basin (Gordey, 2013). Throughout the region there are abundant mid-Cretaceous (98-107 Ma; (Moynihan, 2017)), felsic to intermediate intrusions. Regionally, the deformation, metamorphism, and magmatism are interpreted to have formed as a result of Mesozoic convergence between autochthonous terranes of the Cordilleran Orogeny and the Laurentian continent (Hart et al., 2004; Rasmussen, 2013).

Regional metamorphic grade in the region extends from lower-greenschist (chlorite zone) through upper amphibolite (sillimanite + k-feldspar zone) facies at low pressure (<4 kbar), as indicated by the presence of the metamorphic mineral andalusite. U-Th-Pb monazite ages of 110-108 Ma (D. Moynihan, Pers. Comm., 2018) suggest metamorphism occurred just prior to the emplacement of the ca. 107 Ma Hyland intrusive suite, which cross-cuts regional metamorphic isograds (Moynihan, 2017; Padget, 2018). Contact metamorphism occurs surrounding many of the region's intrusive bodies and metamorphic mineral assemblages in these aureoles suggest emplacement depths of ~9-15 km (~2.5-4 kbar, Moynihan (2012)).

ACTIVITY HIGHLIGHTS/PRELIMINARY RESULTS

Field work completed in the summer of 2018 focused on mapping and sampling along transects aimed at constraining the greenschist-amphibolite facies boundary as well as the pyrite to pyrrhotite transition in the regionally metamorphosed rocks of the Hyland River region. Similar transects through metamorphic contact aureoles in the region were also completed to further constrain the respective positions of these major mineralogical boundaries. Polished thin sections have been prepared for 160 samples and preliminary sulfide mineral assemblage maps have been prepared based on these, complementing existing mapped isograds for traditional metamorphic silicate porphyroblasts (e.g., biotite, garnet, staurolite).

The first appearance of pyrrhotite is being investigated to establish whether a pattern exists between its growth, the breakdown of pyrite, and silicate mineral reactions, such as the fluid-producing breakdown of chlorite or the formation of biotite in metamorphosed pelitic and semi-pelitic rocks. Sulphide mineralization in the samples collected is dominated by pyrite and pyrrhotite, with minor amounts of chalcopyrite and marcasite. At the lowest metamorphic grade in the study area (greenschist facies – chlorite zone), pyrite generally occurs as isolated or clustered euhedral crystals (fig. 2a), occasionally with rounded, inclusion-rich diagenetic cores. With increasing grade, pyrite hosts fewer inclusions, becomes relatively coarser grained, and, where pyrrhotite is present in the sample, pyrite is characterized by more irregular grain boundaries (fig. 2b). Pyrrhotite occurs initially around pyrite grains and as small elongate foliation parallel blebs (fig. 2c). This foliation-parallel growth of pyrrhotite becomes the dominant morphology at metamorphic grades above the biotite isograd. Going upgrade form the biotite isograd, pyrrhotite coarsens considerably, forming up to 2 cm blebs commonly containing inclusions of biotite and quartz (fig. 2e, f, g). Locally, pyrrhotite is partially altered to marcasite along fractures and at the margins of the pyrrhotite grain (fig. 2c).

Preliminary mineral assemblage maps for each field location, such as that in figure 3, indicate that pyrrhotite generally appears downgrade of the biotite isograd. In many cases, where pyrrhotite occurs initially, pyrite is also present; the two minerals are observed to coexist over a narrow interval before pyrrhotite becomes the dominant or exclusive iron-sulphide phase. These patterns suggest that the reaction of pyrite to pyrrhotite is indeed controlled by increasing metamorphic grade and that the reaction interval occurs at lower grade than the first development of silicate porphyroblasts. In higher pressure metamorphic rocks, previous work by Carpenter (1974) found the pyrrhotite isograd occurs at or slightly below the first appearance of biotite in the Barrovian-type metapelitic rocks of the Blue Ridge mountains in southeastern United States.

NEXT STEPS

Ongoing petrographic work for samples collected during the 2018 field season is focused on detailed documentation of the various mineralogical, textural, and morphological changes observed for these rocks during prograde, lower-greenschist to amphibolite facies metamorphism. These data will be used to more accurately map the location of the py-po transition and further assess its relationship to major silicate reactions in the field area. A subset of the collected samples will also be selected for geochemical analysis, which will include whole-rock major and trace-element chemistry, major element mineral chemistry by EPMA, and pyrite-pyrrhotite trace element chemistry by LA-ICP-MS. Geochemical work is planned for samples from multiple transects and will investigate element mobility along prograde metamorphic paths from both contact and regional metamorphic settings. Additionally, thermodynamic modelling of these same samples will focus on the amounts and compositions of fluids generated during metamorphism, and their ability to complex and transport Au and other trace elements.

AC KNOWLEDGEMENTS

This report is a contribution to the NRCan Targeted Geoscience Initiative Phase 5 Program (TGI-5). Field and logistical support was generously supported by the Yukon Geological Survey. The authors would like to thank Patrick Sack and Murray Allan for discussions beneficial to this project. We thank Golden Predator Mining Corp. (3Aces Project: Jeff Cary and Mark Shutty) for logistical support and property access and Stratabound Minerals Corp. (Golden Culvert Project: Kim Tyler) for providing an excellent property tour and site access. Furthermore, the authors acknowledge ongoing analytical support at the University of Calgary from Rob Marr (EPMA), Chris Debuhr (FE-SEM), and Will Matthews (LA-ICP-MS). DEMs were created from DigitalGlobe, Inc. imagery (ArcticDEM – Polar Geospatial Center) funded under National Science Foundation awards 1043681, 1559691, and 1542736. This work is further supported through discovery grant # 037233 to Pattison.

REFERENCES

Bohlke, J. K.
1982: Orogenic (metamorphic-hosted) gold-quartz veins. *US Geological Survey Open-File Report,* 795, 70-76.

Carpenter, R. H.
1974: Pyrrhotite isograd in southeastern Tennessee and southwestern North Carolina. *Geological Society of America Bulletin*, 85(3), 451-456.

Cox, S. F., Etheridge, M. A., Cas, R. A. F., & Clifford, B. A.
1991: Deformational style of the Castlemaine area, Bendigo-Ballarat Zone: Implications for evolution of crustal structure in central Victoria. *Australian Journal of Earth Sciences*, 38(2), 151-170.

Goldfarb, R. J., & Groves, D. I.
2015: Orogenic gold: Common or evolving fluid and metal sources through time. *Lithos*, 233, 2-26.

Goldfarb, R., Baker, T., Dube, B., Groves, D. I., Hart, C. J., & Gosselin, P.
2005: Distribution, character and genesis of gold deposits in metamorphic terranes. Society of Economic Geologists.

Gordey, S. P.
1993: Evolution of the northern Cordilleran miogeocline, Nahanni map area (105I), Yukon and Northwest Territories. *Geol. Surv. Canada Mem.*, 428, 214.

Gordey, S. P., & Geological Survey of Canada.
2013: Evolution of the Selwyn basin region, Sheldon Lake and Tay River map areas, central Yukon. Natural Resources Canada.

Hart, C. J., Goldfarb, R. J., Lewis, L. L., & Mair, J. L.
2004: The Northern Cordilleran Mid-Cretaceous Plutonic Province: Ilmenite/Magnetite-series Granitoids and Intrusion-related Mineralisation. *Resource Geology*, 54(3), 253-280.

Large, R. R., Bull, S. W., & Maslennikov, V. V.
2011: A carbonaceous sedimentary source-rock model for Carlin-type and orogenic gold deposits. *Economic Geology*, 106(3), 331-358.

Large, R. R., Danyushevsky, L., Hollit, C., Maslennikov, V., Meffre, S., Gilbert, S., & Singh, B.
2009: Gold and trace element zonation in pyrite using a laser imaging technique: Implications for the timing of gold in orogenic and Carlin-style sediment-hosted deposits. *Economic Geology*, 104(5), 635-668.

Moynihan, D.,
2017: Progress report on geological mapping in the upper Hyland River region of southeastern Yukon (parts of NTS 105H / 08, 09, 10, 15, 16 and 105I / 02). Yukon Exploration and Geology, 163-180.

Moynihan, D.,
2012: A preliminary assessment of low pressure, amphibolite-facies metamorphism in the upper Hyland River area (NTS 105H), southeast Yukon. Yukon Exploration and Geology, 99-114.

Padget, C.,
2018: Bedrock geology and metamorphism of the Anderson Lake area, parts of NTS 105H07, 105H/10, and 105H/11, southeastern Yukon. Tech. rep., Yukon Geological Survey, Open File 2018-19.

Phillips, G. N., & Powell, R.
2010: Formation of gold deposits: a metamorphic devolatilization model. *Journal of Metamorphic Geology*, 28(6), 689-718.

Rasmussen, K.,
2013: The timing, composition, and petrogenesis of syn-to post-accretionary magmatism in the northern Cordilleran miogeocline, eastern Yukon and southwestern. Ph.D. thesis, University of British Columbia.

Tomkins, A. G.
2013: On the source of orogenic gold. *Geology*, 41(12), 1255-1256.

Tomkins, A. G.
2010: Windows of metamorphic sulfur liberation in the crust: Implications for gold deposit genesis. *Geochimica et Cosmochimica Acta*, 74(11), 3246-3259.

Toulmin III, P., & Barton Jr, P. B.
1964: A thermodynamic study of pyrite and pyrrhotite. *Geochimica et Cosmochimica Acta*, 28(5), 641-671.

Zhong, R., Brugger, J., Tomkins, A. G., Chen, Y., & Li, W.
2015: Fate of gold and base metals during metamorphic devolatilization of a pelite. *Geochimica et Cosmochimica Acta*, 171, 338-352.

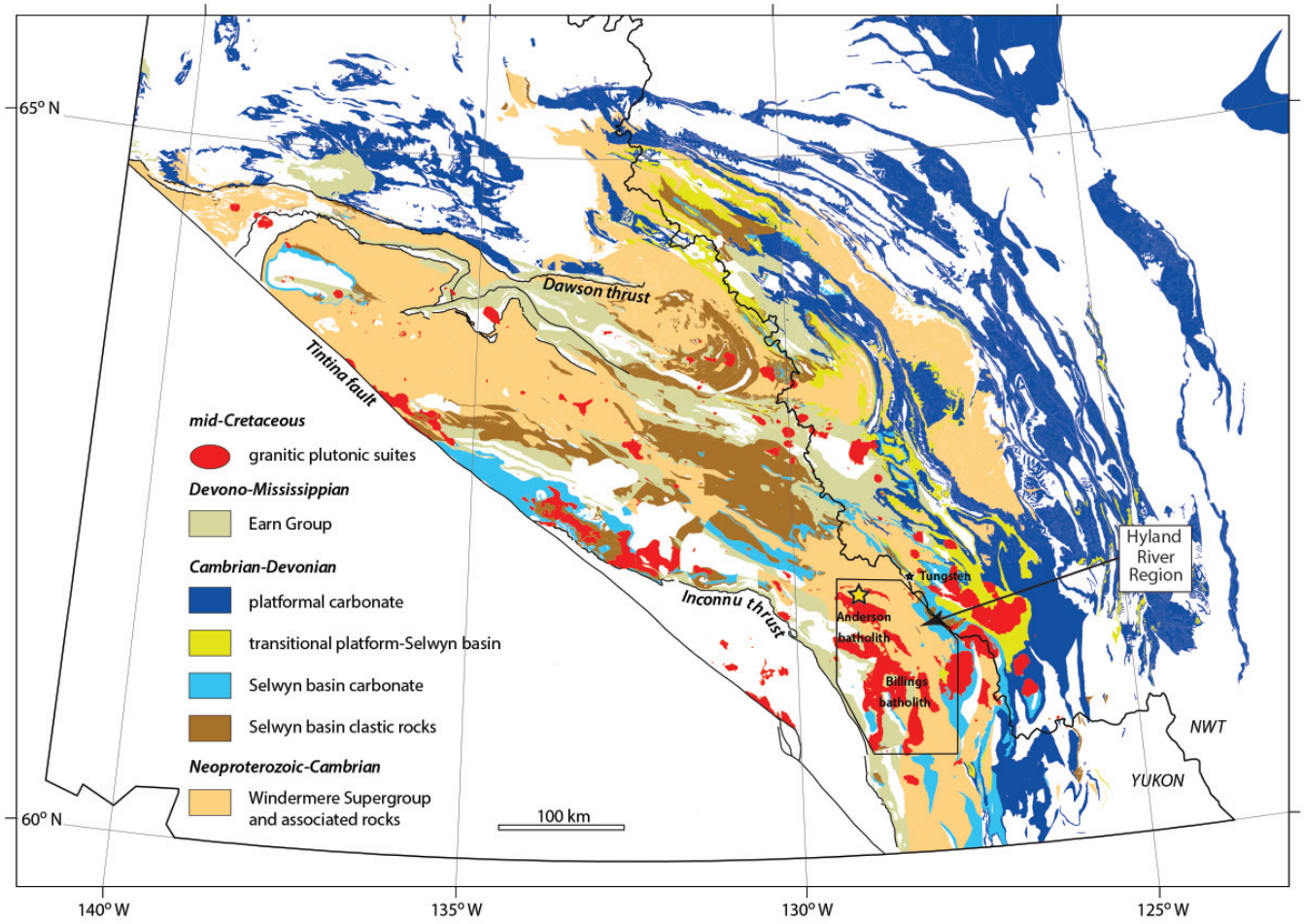

Figure 1. Geological map of the Selwyn fold-and-thrust belt east of the Tintina Fault. The Hyland River region sits within the mixed carbonate and clastic rocks of the Windermere Supergroup and associated strata. Mid-Cretaceous felsic to intermediate plutonism is found throughout the study area. Figure modified after Moynihan (2015).

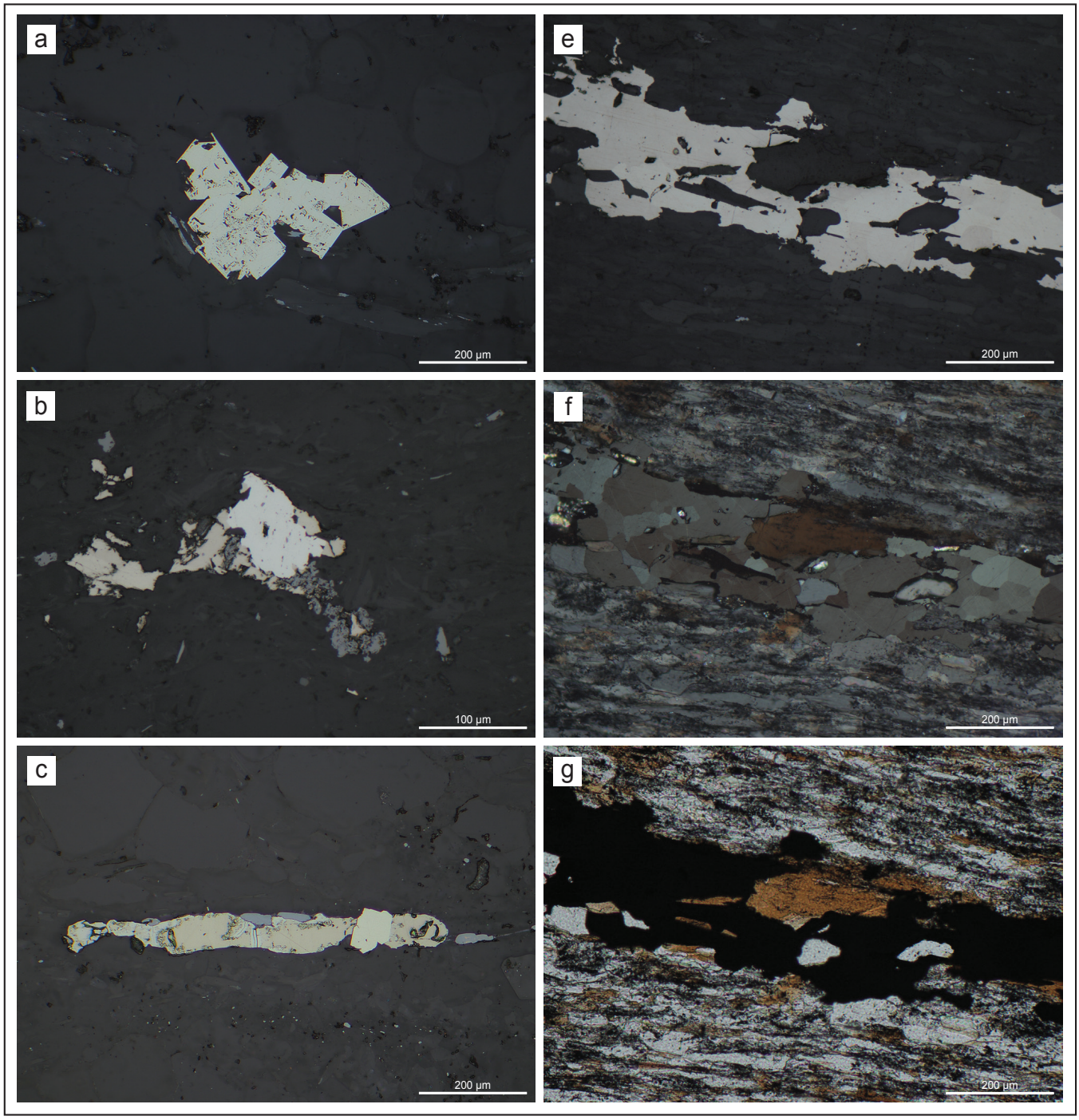

Figure 2. Reflected light photomicrographs of samples collected during 2018 field season showing common pyrite and pyrrhotite textures. a) Cluster of euhedral pyrite crystals from chlorite-zone phyllite. b) Pyrrhotite formed around pyrite with magnetite. c) Subhedral pyrite crystal and pyrrhotite which is shown growing parallel to the dominant foliation. Marcasite alteration along fractures and margins of pyrrhotite. e) Coarse pyrrhotite with inclusions of biotite and quartz. f) Same image as (e) under partially cross-polarized light showing characteristic anisotropy of pyrrhotite. g) Same image as (e,f) under transmitted plane-polarized light.

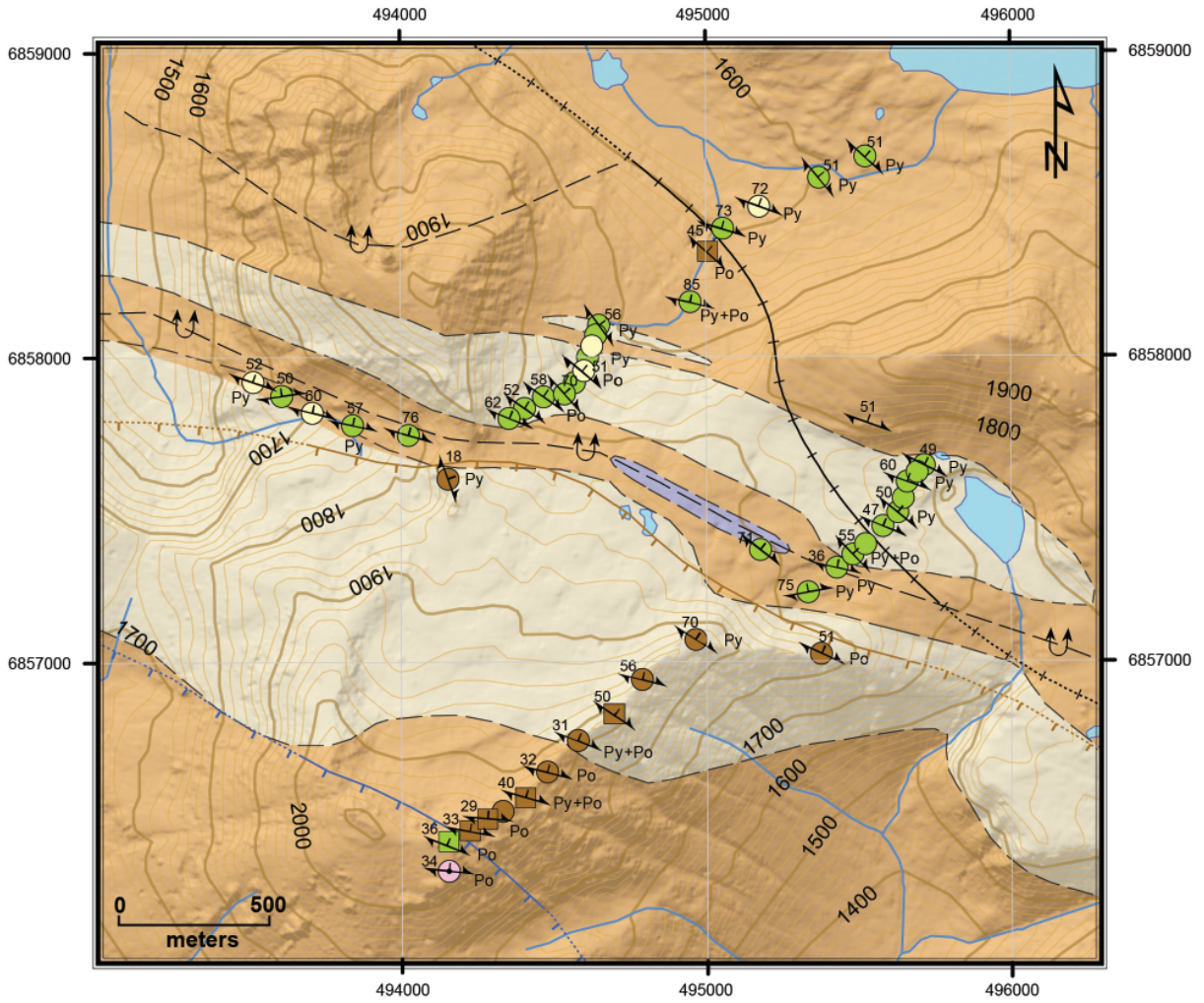

Figure 3. Geology and mineral assemblage map for one camp from the 2018 field season. Mineral isograds mark the first appearance of a mineral based on thin section and hand sample observation only. Metamorphic grade increases to the ~SW. Location of map marked as a yellow star on figure 1.

An experimental investigation of the solubility and speciation of uranium in hydrothermal ore fluids

K.U. Rempel[1], A.E. Williams-Jones[1], K. Fuller[1]

Abstract: Experimental data on the mobility of uranium in hydrothermal fluids are required to accurately model the formation of uranium ore deposits. This study aims to conduct experiments on the solubility and speciation of U(IV) and U(VI) in fluoride- and phosphate-bearing solutions, as well as flow-through, fluid-rock interaction experiments designed to assess the optimal P-T-X conditions for U precipitation, which will be integrated into a comprehensive genetic model. Early work has focused on method development for the solubility and flow-through experiments. Preliminary experiments on UO2 solubility in 0.01 M F- solutions at 200°C produced concentrations of 1.76 to 3.92 ppm U, demonstrating the surprisingly high mobility of U(IV) and the importance of U fluoride complexes for ore-forming systems.

INTRODUCTION

Canadian uranium resources such as the sediment-hosted, unconformity-type deposits of the Athabasca basin, Saskatchewan, and the magmatic-associated, iron-oxide copper gold (IOCG) deposits of the Great Bear Magmatic Zone, NWT, are of key interest as exploration targets. In genetic models for these deposits, uranium is considered to have been transported in hydrothermal fluids to the sites of deposition. For example, in the case of unconformity-related deposits, U(VI)-bearing, oxidised basinal brines are thought to have reacted with an on-site reductant such as graphite to precipitate U(IV) ore (e.g., Komninou and Sverjensky 1996; Fayek and Kyser 1997). However, experimental data on uranium mobility in hydrothermal fluids at elevated temperature and pressure are largely lacking, and existing models are dependent on highly inaccurate extrapolations of low-temperature data (Grandstaff 1976; Romberger 1984).

Previous experimental studies on the behaviour of uranium in aqueous solutions at ambient conditions, in combination with observations of natural uranium deposits, suggest that U is dissolved in solution as U(VI)-chloride, -fluoride, -phosphate or -carbonate complexes and precipitated as U(IV) minerals (Langmuir 1978; review by Bastrakov 2010). On the other hand, a study of uraninite solubility in alkaline solutions at temperatures up to 300°C by Tremaine et al. (1981) showed that U(IV) is relatively mobile as hydroxyl complexes. In chloride solutions at temperatures up to 350°C, Timofeev et al. (2018) found that both U(IV) and U(VI) may be transported as Cl- complexes, and that U(IV) solubility under reducing conditions is significantly higher than that of U(VI) under oxidising conditions at high chloride ion activity. These results have important implications for the existing uranium ore genesis models that assume transport of uranium as U(VI) and its immobility as U(IV). Despite these advances, considerable work remains to be done to understand the aqueous geochemistry of uranium at elevated temperature.

This study aims to redress the scarcity of experimental data on uranium speciation by conducting experiments at elevated temperature and pressure to determine the solubility and speciation of uranium in hydrothermal solutions and to evaluate the effects of fluid and host rock composition on uranium mineralisation. Solubility studies involving the systematic variation of fluid pH, oxidation state and ligand concentration are being used to evaluate the optimal conditions for uranium transport and determine the dominant uranium complexes in solution. Fluid-rock reaction experiments will be used to investigate the dependence of uranium ore precipitation on fluid and host rock composition. The thermodynamic data derived from these experiments will be integrated into a genetic model for uranium ore-forming systems for use in predictive exploration modelling.

KEY ACTIVITY HIGHLIGHTS

The initial stages of the research were focused on method development for solubility studies in fluoride-bearing fluids. Because of the corrosive effect of HF on metal or glass components, these experiments are being done in titanium autoclaves, but with all wetted parts made of Teflon (Fig. 1). Thus, method development included fabrication of gas-tight Teflon liners for the Ti autoclaves and Teflon holders for the solid phases (U oxides and oxygen fugacity buffers). Owing to the hazards of working with uranium, rather than using natural U oxide samples for these solubility experiments, we located a supply of depleted uranium (IBI labs, Inc.).

[1]Department of Earth and Planetary Sciences, McGill University, 3450 University Street, Montréal, Quebec H3A 0E8

The initial stages of the research were focused on method development for solubility studies in fluoride-bearing fluids. Because of the corrosive effect of HF on metal or glass components, these experiments are being done in titanium autoclaves, but with all wetted parts made of Teflon (Fig. 1). Thus, method development included fabrication of gas-tight Teflon liners for the Ti autoclaves and Teflon holders for the solid phases (U oxides and oxygen fugacity buffers). Owing to the hazards of working with uranium, rather than using natural U oxide samples for these solubility experiments, we located a supply of depleted uranium (IBI labs, Inc.).

The experimental setup for the flow-through, water-rock reaction experiments has also been developed. An externally-heated, Teflon-lined sampling vessel has been modified with an high-pressure liquid chromatography (HPLC) pump to allow a constant flow of U-bearing solution, which can be pumped into the vessel through an input line at the desired flow rate and fluid:rock ratio (Fig. 2). Temperature and pressure within the vessel are monitored with an internal thermocouple and pressure transducer, respectively, and gases to control oxygen fugacity will be input via an independent gas line. Throughout the experiment, in order to monitor reaction progress and changes in fluid composition, the solution will be extracted through an output line fitted with an inline back-pressure regulator for sampling and analysis.

The solubility experiments are underway, and initial results are available for a kinetic study of UO_2 solubility in 0.01 m F-, pH 2 solutions at 200°C and saturated vapour pressure (P_{sat}). Results of these experiments show that chemical equilibrium or steady-state is achieved within 3 days, and U(IV) concentrations in solutions of constant composition are relatively reproducible. They are high, ranging from 1.76 to 3.92 ppm (avg 2.68 ppm, n = 5; Fig. 3). The solutions were analysed using inductively coupled plasma mass spectrometry (ICP-MS) with a detection limit of 1 ppb. In comparison, previous experimental studies of UO2 solubility at similar temperatures produced ppb-level concentrations for ligand-free alkaline solutions at 200°C (8-30 ppb; Tremaine et al. 1981) and ppb- to ppm-level concentrations in chloride-bearing acidic solutions at 250°C (7 ppb-20 ppm; Timofeev et al. 2018). These findings suggest that, as is the case with chloride, fluoride complexation may be of major importance for uranium transport in hydrothermal fluids, and that U(IV) is highly mobile in fluoride-bearing solutions.

NEXT STEPS

Additional experiments on the solubility of UO_2 and UO_3 in fluoride-bearing solutions will be conducted at both acidic and alkaline pH, over a range of temperatures (150, 200 and 250°C) and P_{sat}. The fluoride concentration of individual runs will be varied to determine the stoichiometry of U-fluoride complexes. These data will be used to determine the solubility products and formation constants for the relevant reactions and species, which are needed for rigorous thermodynamic modelling of uranium behaviour in hydrothermal fluids at elevated temperature.

The experiments for U(IV) and U(VI) will be extended to phosphate-bearing solutions at acidic and alkaline pH, using variable ligand concentrations to assess the stoichiometry of U-phosphate complexes. As PO_4^{3-} solutions do not have the metal-corrosion effects of F- solutions, Teflon liners (used up to 250°C) will not be needed for the Ti autoclaves, so the temperature range will be extended to 350°C. As in the fluoride-bearing experiments, the solubility data from phosphate-bearing runs will be used to determine the dominant species in solution and to derive the thermodynamic data for those species.

In parallel with the solubility experiments, we will be conducting water-rock interaction experiments to simulate uranium mineralisation for several host rock and fluid compositions (oxidising and reducing fluids and rocks; acidic and alkaline fluids; temperatures from 150 to 250°C). Building on the results of the initial experiments, P-T-X parameters will be modified mid-experiment to promote mineralising conditions. Both the unreacted and reacted host rocks will be investigated with scanning electron microscopy (SEM) to determine the mineralogy of precipitated uranium ores and other mineralisation-related changes in mineralogy. These results will allow an assessment of the optimal fluid and rock compositions for uranium precipitation, as well as an evaluation of precipitation mechanisms.

Finally, the results will be integrated into a genetic model for the formation of uranium mineralisation by hydrothermal fluids, e.g., for unconformity- and IOCG-type ore deposits. The thermodynamic constants determined for relevant aqueous uranium species will be used to input the species into thermodynamic modelling software (HCh; Shvarov 1999). The model will incorporate the results of solubility and flow-through experiments to predict the precipitation of uranium minerals from hydrothermal solutions in contact with a variety of host rock types. It is our expectation that the resulting predictions will provide a comprehensive genetic model incorporating uranium transport and precipitation at P-T-X conditions appropriate to the uranium ore-forming systems of interest.

ACKNOWLEDGMENTS

This report is a contribution to NRCan's Targeted Geoscience Initiative Program (TGI). Support for this study was provided through the Phase 2 Uranium Ore Systems Project. We also extend thanks to Dr A. Migdisov for invaluable input into the method development.

REFERENCES

Bastrakov EN, Jaireth S, Mernagh T
2010: Solubility of uranium in hydrothermal fluids at 25° to 300°C. Geosci Aust Rec 2010/29.

Fayek M, Kyser TK
1997: Characterization of multiple fluid-flow events and rare-earth-element mobility associated with formation of unconformity-type uranium deposits in the Athabasca Basin, Saskatchewan. Can Miner 35: 627-658.

Grandstaff DE
1976: A kinetic study of the dissolution of uraninite. Econ Geol 71: 1493-1506.

Komninou A, Sverjensky DA
1996: Geochemical modeling of the formation of an unconformity-type uranium deposit. Econ Geol 91: 590-606.

Langmuir D
1978: Uranium solution-mineral equilibria at low temperatures with applications to sedimentary ore deposits. Geochim Cosmochim Acta 42: 547-569.

Romberger SB
1984: Transport and deposition of uranium in hydrothermal systems of temperatures up to 300°C: geological implications. In Uranium Geochemistry, Resources (ed) B de Vivo, F Ippolito, G Capaldi and PR Simpson, Inst Min Metall, London, p 12-17.

Shvarov YV
1999: Algorithmization of the numerical equilibrium modelling of dynamic geochemical processes. Geochem Int 37: 571-576.

Timofeev A, Migdisov AA, Williams-Jones AE, Roback R, Nelson AT, Xu H
2018: Uranium transport in acidic brines under reducing conditions. Nat Commun 9: 1469.

Tremaine PR, Chen JD, Wallace GJ, Boivin WA
1981: Solubility of uranium(IV) oxide in alkaline aqueous solutions to 300°C. J Solut Chem 10: 221-230.

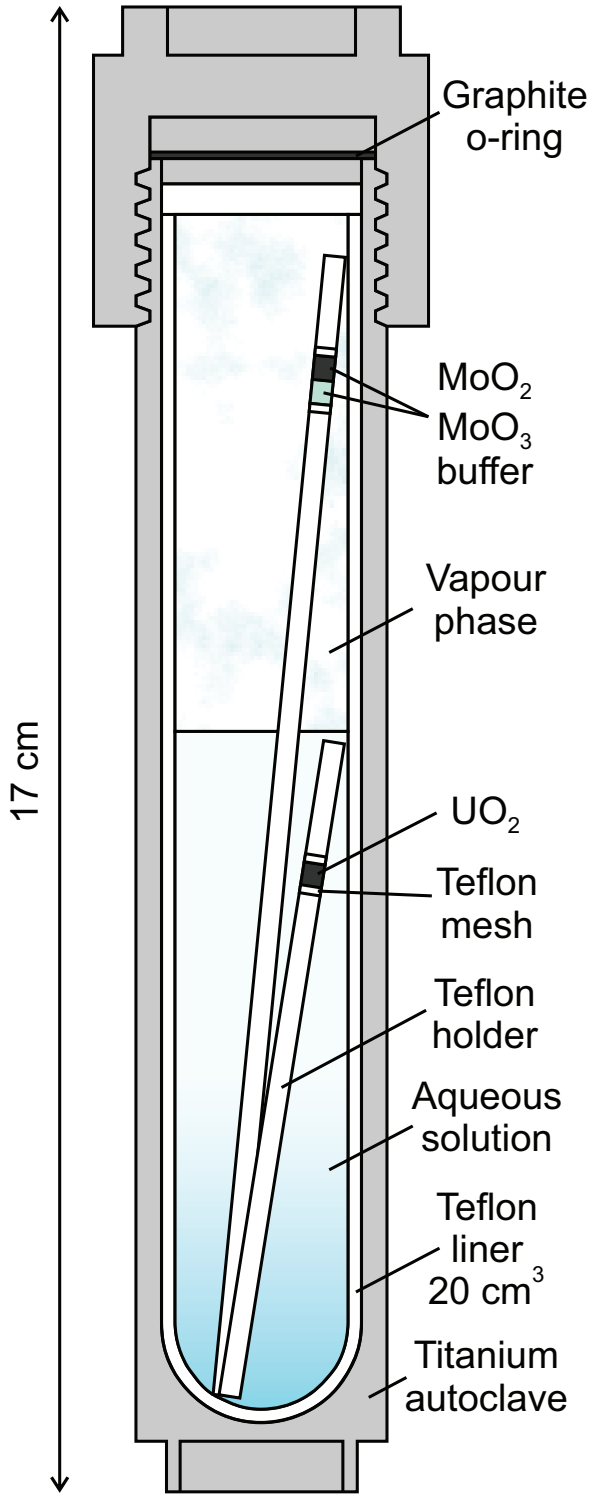

Figure 1. Schematic diagram of the Teflon-lined titanium autoclaves used for the solubility experiments at elevated temperature (200°C), illustrating the UO2 in contact with the solution and the MoO2-MoO3 oxygen fugacity buffer in contact with the vapour.

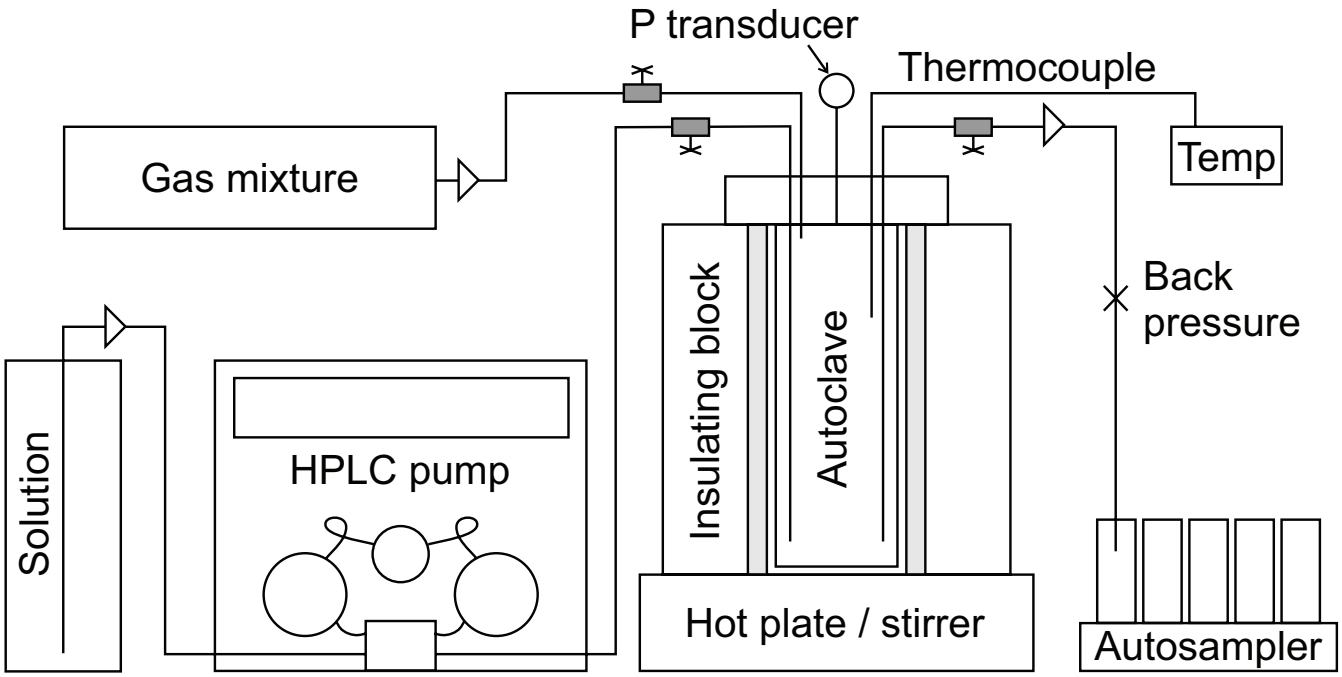

Figure 2. Schematic diagram of the flow-through system used for the water-rock reaction experiments, in which U-bearing solution and gas phases are pumped into the Teflon-lined autoclave to be reacted with rock fragments, then extracted through an output line to an autosampler.

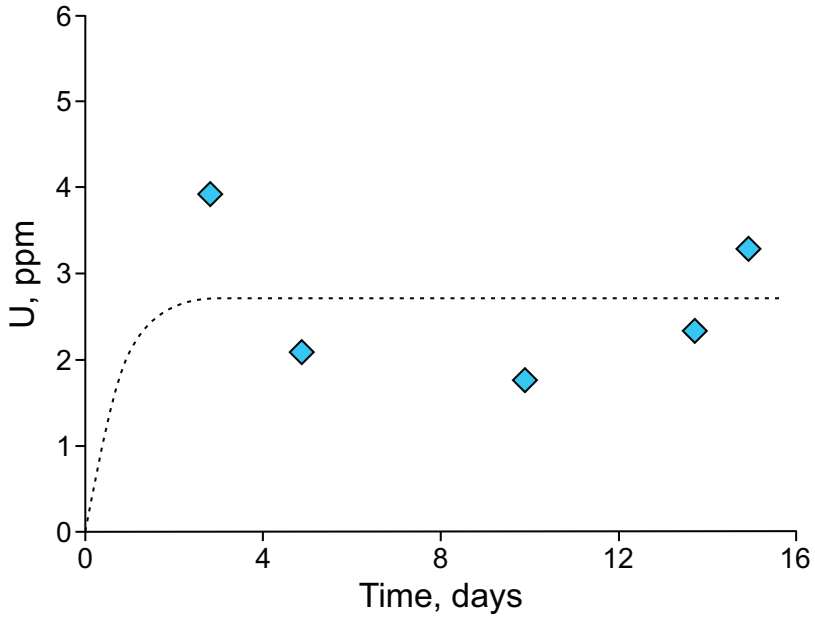

Figure 3. Preliminary results of a kinetic experiment evaluating the solubility of UO2 in solutions with 0.01 m NaF, 0.05 m NaClO4 and 0.01 m HClO4 (pH 2.00) at 200°C and 15.6 bar, showing U concentration in ppm vs the time of the experiment in days. The dotted line illustrates an idealised path to chemical equilibrium and the average U concentration of 2.68 ppm.

Controls on the ore fertility of arc magmas

Carter Grondahl[1], Alexandra Tsay[1] and Zoltan Zajacz[1]

Abstract: Continental arc magmas represent the parental igneous systems of porphyry Cu-Mo deposits. Studies exploring the fertility of these arcs are often based on global data sets or imperfect analogue settings such as oceanic basalts. We seek to refine our understanding of continental arc magmatism in an economic context by sampling a suite of volcanoes in the Andean Southern Volcanic Zone (SVZ). Our sample suite extends from thick crust and the presence of world-class porphyry Cu deposits in the north to a barren south with thin crust. The most primitive olivine-hosted silicate melt inclusions from these samples were analyzed by laser ablation inductively coupled plasma mass spectrometry for major and trace elements including S, Cu, Mo, and Ag. The quantitative analysis of S in silicate melt inclusions by Laser Ablation Inductively Coupled Plasma Mass Spectrometry (**LA-ICP-MS**) required extensive analytical method development, which constitutes a significant part of this study. The application of non-modal batch melting models demonstrates that the partial melting of a sulfide-bearing primitive or depleted mantle source is capable of generating the observed ore metal concentrations in the SVZ magmas and that there is no significant difference in the metal endowment of the barren and fertile segments of the arc. On the other hand, magmas in the fertile north exhibit significantly higher S concentrations.

INTRODUCTION

Porphyry-type magmatic-hydrothermal ore deposits are major contributors to the global production of Cu, Mo, Au, and Ag. Canada is well-endowed with these deposits, particularly in British Columbia (Sinclair, 2007), although significant exploration challenges are present due to rugged terrain and extensive burial of bedrock under quaternary cover. In these conditions, geologists employ generalised conceptual models of ore deposit genesis to guide exploration and on regional and deposit scales. Therefore, our understanding of the structural and geochemical conditions which favour ore formation is fundamental to successful exploration efforts. The intensity of activity surrounding near-surface deposit evaluation and extraction has resulted in the ore deposit itself being the most extensively studied component of the genetic model (Sinclair, 2007) whereas deep processes in the lower crust and mantle are less well constrained.

Compilations of global datasets have shown that arc lavas erupted on thick crust typically have lower Cu concentrations than those on thinner crust (Chiaradia, 2014). However, porphyry Cu deposits preferentially form via arc magmatism in mature and thick continental crust. One resolution to this paradox that has recently gained favour invokes lower crustal sulfide accumulation, wherein ore metals stripped from ascending magma may be mobilized during subsequent sulfide breakdown events to generate particularly ore metal-rich magma batches and increase the odds of ore formation in the upper crust (Chiaradia, 2014; Jenner, 2017). These interpretations are informed by whole rock analyses, which are subject to syn- and post-eruptive modification including degassing and alteration. Furthermore, much of our understanding of the ore metal budget in arc magmas is inferred from ocean floor samples from back arc settings (Jenner, 2017; Jenner et al., 2010). The first step of the porphyry deposit genetic model focusing on magmatic processes therefore requires additional attention.

We therefore endeavour to better constrain the budget of key elements including ore metals, S, and Cl in continental arc magmas. The co-availability of these elements in magmas is crucial for ore formation, because ore metals form complexes with S and Cl in the magmatic volatile phase which ascends to precipitate ore minerals (Zajacz et al., 2017).

Considering that volatile elements are degassed during decompression and crystallization of magmas, the only way to reconstruct their concentration in the silicate melt along the liquid line of descent of a magma is the analysis of silicate melt inclusions (**SMI**) in minerals. This is commonly done by using Electron Probe MicroAnalysis (**EPMA**) or Secondary Ion Mass Spectrometry (**SIMS**); and both of these techniques require glassy inclusions exposed by polishing. However, such inclusions are restricted to well-quenched volcanic rocks and even in those, they will typically contain a shrinkage bubble, which may concentrate a part of the volatile elements in the inclusion yielding artifically low concentrations in the glass. The rehomogenization of hydrous SMI by heating experiments is however likely to lead to leakage and volatile loss due to internal overpressure at high temperature. Therefore, the best approach to obtain volatile element concentrations is to sample the enitre heterogeneos inclusion without heating, which can only be accomplished by LA-ICP-MS.

Therefore, this study has also included analytical method developments to extend the applicability of LA-ICP-MS to the quantitative analysis of S and Cl concentrations in unheated silicate melt inclusions in minerals.

[1] Department of Earth Sciences, University of Toronto, 22 Russell Street, Toronto, Ontario M5S 3B1

STUDY AREA

The Andes provide a classic example of continental arc magmatism, and are particularly rich in magmatic-hydrothermal mineralization (Cooke et al., 2005). We focus on the Andean Southern Volcanic Zone (SVZ) between 33 and 40 °S as this region has considerable systematic variability in a number of key characteristics (Fig. 1). Structurally, the north has a greater depth to both the crust-mantle boundary (45-50 km) and surface of the subducting slab (105-120 km) than the south where these are located at 35-40 km and 75-90 km, respectively (Tassara and Echaurren, 2012). This increased crustal thickness arises from a decreasing slab dip angle due to subduction of the Juan Fernandez Ridge seamount chain. The resulting periodic crustal thickening and arc migration cycles correspond temporally to porphyry ore-forming events (Kay et al., 2005). Compositionally, the dominant degree of differentiation rises from basaltic-basaltic andesitic in the south to andesitic-dacitic in the north due to increased crustal residence times. However, it is the difference in economic potential that is perhaps the most striking.

The northern SVZ is spatially associated with some the world's largest porphyry Cu deposits (e.g. El Teniente and Rio Blanco – Los Bronces). Both systems are young (ca. 5 Ma; Deckart et al., 2005; Spencer et al., 2015), and at El Teniente the ~20 Myr magmatic compositional trends which culminated in ore formation are mirrored collectively by the compositions of the modern SVZ volcanoes (Kay et al., 2005). Therefore, the study of modern SVZ eruptive material can yield insight into the highly fertile nature of this arc segment. In sharp contrast to the north, the SVZ south of El Teniente is barren.

METHODOLOGY

To better understand the ore metal budget of SVZ magmas, we sampled eruptive material from seven volcanoes between 33 and 40 °S (Fig. 1). From this material we measure the composition of silicate melt inclusions, which form when droplets of silicate melt are trapped within growing phenocrysts. These SMI preserve the composition of the silicate melt at the time of trapping, prior to eruption and related compositional modification. The concentrations of major and trace elements were determined by LA-ICP-MS. Signals were quantified following the method of (Halter et al., 2002) using GSD-1g as an external standard (except Ag: NIST 610, and S: in-house glass standard). During quantification of Ag, contributions to the ^{107}Ag signal from polyatomic mass interferences (i.e. $^{91}Zr^{16}O$) were for corrected for using natural mineral and synthetic glass standards. The mixed SMI-olivine signals were deconvoluted by iterative subtraction of the host until the inclusions satisfied KD $Fe\text{-}Mg^{Olivine\text{-}melt} = 0.31$ (Ulmer, 1989).

We determined the ore metal and S budget of the most primitive material sampled at each volcano, as this represents the closest compositions to those which were present upon initial magma segregation following mantle melting. To this end, SMI are filtered for both low K_2O and high forsterite content of the olivine host. All SMI presented here have <60 wt % SiO_2.

To be able to determine S concentrations in silicate melt inclusions simultaneously with all other element concentrations by LA-ICP-MS, we have conducted extensive method developments in this direction. The main challenges hindering the analysis of S and Cl by LA-ICP-MS are: **1)** the 1st ionization potential of both S (10.36 eV) and Cl (12.97 eV) is high and close to that of plasma gas Argon (15.76 eV) which causes their relatively low sensitivities; **2)** high backgrounds resulting from polyatomic interderences (e.g. $^{16}O^{16}O$, $^{18}O^{16}O$, and ^{36}ArH molecules on ^{32}S, ^{34}S and ^{37}Cl, respectively), high gas blanks (real S in He and Ar gases) and ambient air; **3)** remobilization of previosly absorbed S and Cl in the sample introduction system during the ablation of solid materials creating an arifical signal; **4)** lack of appropriate standard reference materials.

The polyatomic interferences are primarily apparent for ^{32}S because of the following relationship in the natural abundance of O and S isotopes: $^{18}O/^{16}O << ^{34}S/^{32}S$. Consistent with the observation of Guillong et al. (2008), the comparison of the ^{32}S and ^{34}S blanks on our system suggests that only ^{32}S suffers from significant double oxygen interference, and most of the ^{34}S backround represents real S. To tackle this challenge we tested various gas purifiers; however, these only reduced ^{32}S blanks by removing oxygen. The only real improvement of ^{34}S backgrounds were yielded by the use of an in house built ablation cell. This ablation cell turned out to be the most effective mean to tackle challenge no. (3) as well, as was also proposed for S analysis in fluid inclusions by Seo et al. (2011).

The cell was built from materials that do not degas sulfur and are resistant to surface-absorption of S and halogens. Circular samples of up to 27 mm in diamter can be fitted inside. The flush-out time is about 5-6 s, and relative sensitivity factors for a full range of major and trace elements including sulfur are homogeneous within 3 relative% deviation throughout the cell area. The S and Cl blanks and artifical signals generated when ablating S- and Cl-free solids are much smaller using this cell than in the factory cell that came with the laser ablation system. There is no measurable artificial ^{32}S signal in the cell, whereas the artificial 34S signal is equivalent to 50 – 100 ppm S in the sample.

To tackle challenge no. (4), we synthetised a homogeneous andesite glass doped with 2890 ppm S, 5790 ppm Cl and all common major and trace elements at around 40 ppm concentration level, which can be used as a single external standard for SMI analysis (Fig. 2).

PRELIMINARY RESULTS AND INTERPRETATION

Sulfur concentration determination by LA-ICP-MS

Synthetic silicate glasses covering a wide range of S concentrations have been analyzed by LA-ICP-MS and EPMA to assess the acuracy and the precision of the S concentration determination by LA-ICP-MS.

In the case of ^{34}S, a systematic correction procedure was used to account for the effect of the artifical signal based on signals derived by the ablation of a S-free glass at the beginning and end of each analysisblock. While comparing data obtained by LA-ICP-MS and EPMA on the same glasess, it is apparent that most points fall within the 10% error band from the 1:1 line, and the mean absolute percentage error of the LA-ICP-MS data is 5% relative to the EPMA reference values (Fig. 3). While using 40 µm beam diameter, 10 Hz repetition rate and 6 J/cm^2 energy density on the sample surface, typical limits of detection for S in silicate glasses are 10-20 and 20-30 ppm, when using ^{32}S and ^{34}S, respectively. Similarly good match was obtained when analyzing glassy silicate melt inclusions from the same sample by LA-ICP-MS and EPMA (Fig. 4., 5).

Ore metals and volatiles in the Southern Volcanic Zone magmas

Among the most primitive SMI in the SVZ volcanics, key differences are apparent in the behaviour of Cu, Mo, Ag (Fig. 6). Copper concentrations are lower in the north than the south, as predicted by global whole rock trends (Chiaradia, 2014), although the SMI converge at ~65 ppm Cu. Molybdenum (0.5-1.5 ppm) is well-correlated with K2O, and both are positively correlated with latitude and therefore crustal thickness. This behaviour can be attributed to crustal contamination (e.g., Hildreth and Moorbath, 1988) because SVZ SMI have Mo/Rb > 0.025 (Audétat et al., 2011). Silver shows no geographic trends, and clusters between 30-80 ppb for all volcanoes.

Sulfur concentrations are higher in north (~2700 ppm) than the south (~1250 ppm), and are similar to the predicted solubility of S^{6+} and S^{2}-, respectively (Li and Ripley, 2009). This tendency of magmas to be sulfur-rich and relatively oxidized may be a key factor enabling porphyry ore formation in the north.

To evaluate the likelihood that simple mantle partial melting generated the observed SMI compositions, we calculate hypothetical melt compositions using a non-modal batch melting models. Mineral modes and melting proportions are from (Fram and Lesher, 1993), and the solubility of S^{2}- in equilibrium with sulfide phases at mantle conditions (~1300 ppm) is from (Li and Ripley, 2009). In this model, ore metal concentrations in the partial melt are governed by: 1) the ore metal concentrations in the bulk mantle; 2) the concentration of S in the mantle, and therefore the mass proportion of a sulfide phase; 3) the relative proportion of solid and molten sulfide, as the compatibility of chalcophile elements can vary considerably depending on the nature of the sulfide phase (e.g., Li and Audetat, 2015).

We find that the Cu, Mo, and Ag concentrations measured in SMI can be recreated by appropriate degrees of partial melting (6-12%; Turner, Langmuir et al. 2016) of a primitive mantle composition with 0.05 % sulfide (Fig. 7). However, because estimates of ore metal concentrations are similar in both primitive and depleted mantle sources (Palme and O'Neill, 2014; Salters and Stracke, 2004), their concentrations in the partial melt are primarily a function of the abundance of S in the mantle. The mantle melting model approaches the lower end of the observed range of Mo concentrations (0.5 ppm) indicating significant crustal contribution to the Mo budget of the magmas already during very early stages of differentiation. but underpredicts the observed Mo concentrations.

CONCLUSIONS AND FUTURE PERSPECTIVES

Silicate melt inclusion compositions demonstrate that ore metal abundances in near-primitive arc magmas in the Southern Volcanic Zone of the Andes do not exert primary control on ore fertility. The measured ore metal concentrations throughout the studied arc segment can be produced by the partial melting of a primitive or depleted mantle source at melt fractions common for arc magmatism. It is apparent that the initial metal endowment of magmas in the barren and fertile segments of the SVZ are similar, but the S-rich nature of northern SVZ magmas likely increases the likelihood of ore formation.

Future work will expand upon and refine this model by incorporating the concentrations of additional elements (e.g., Au, Pt and Cl) from SMI, and consider the effects of magma differentiation on ore fertility in the SVZ.

ACKNOWLEDGEMENTS

This report is a contribution to NRCan's Targeted Geoscience Initiative (TGI) program. Additional funding was received from the Society of Economic Geologists Canada Foundation Student Research Grant to Carter Grondahl and NSERC of Canada Discovery Grants to Zoltan Zajacz. Instruments were purchased with funding support from the Canada Foundation for Innovation.

REFERENCES

Audétat, A., Dolejš, D., Lowenstern, J.B.
2011: Molybdenite Saturation in Silicic Magmas: Occurrence and Petrological Implications. Journal of Petrology, 52(5): 891-904.

Chiaradia, M.
2014: Copper enrichment in arc magmas controlled by overriding plate thickness. Nature Geoscience, 7(1): 43-46.

Cooke, D.R., Hollings, P., Walshe, J.L.
2005: Giant Porphyry Deposits: Characteristics, Distribution, and Tectonic Controls. Economic Geology, 100(5): 801-818.

Deckart, K., Clark, A.H., Aguilar A., C., Vargas R., R., Bertens, A., Mortensen, J.K., Fannig, M.
2005: Magmatic and Hydrothermal Chronology of the Giant Río Blanco Porphyry Copper Deposit, Central Chile: Implications of an Integrated U-Pb and 40Ar/39Ar Database. Economic Geology, 100: 905-934.

Fram, M.S., Lesher, C.E.
1993: Geochemical constraints on mantle melting during creation of the North Atlantic basin. Nature, 363: 712-715.

Guillong, M., Latkoczy, C., Seo, J.H., Gunther, D., Heinrich, C.A.
2008: Determination of sulfur in fluid inclusions by laser ablation ICP-MS. Journal of Analytical Atomic Spectrometry, 23(12): 1581-1589.

Halter, W., Pettke, T., Heinrich, C.A., Rothen-Rutishauser, B.
2002: Major to trace element analysisof melt inclusionsby laser-ablation ICP-MS: methods of quantification. Chemical Geology, 183: 63-86.

Hildreth, W., Moorbath, S.
1988: Crustal contributions to arc magmatism in the Andes of Central Chile. Contributions to Mineralogy and Petrology, 98(4): 455-489.

Jenner, F.E.
2017: Cumulate causes for the low contents of sulfide-loving elements in the continental crust. Nature Geoscience, 10(7): 524-529.

Jenner, F.E., O'Neill, H.S.C., Arculus, R.J., Mavrogenes, J.A.
2010.: The Magnetite Crisis in the Evolution of Arc-related Magmas and the Initial Concentration of Au, Ag and Cu. Journal of Petrology, 51(12): 2445-2464.

Kay, S.M., Godoy, E., Kurtz, A.
2005: Episodic arc migration, crustal thickening, subduction erosion, and magmatism in the south-central Andes. Geological Society of America Bulletin, 117(1): 67-88.

Li, C., Ripley, E.M.
2009: Sulfur Contents at Sulfide-Liquid or Anhydrite Saturation in Silicate Melts: Empirical Equations and Example Applications. Economic Geology, 104: 405-412.

Li, Y., Audetat, A.
2015: Effects of temperature, silicate melt composition, and oxygen fugacity on the partitioning of V, Mn, Co, Ni, Cu, Zn, As, Mo, Ag, Sn, Sb, W, Au, Pb, and Bi between sulfide phases and silicate melt. Geochimica Et Cosmochimica Acta, 162: 25-45.

Liu, X., Xiong, X., Audetat, A., Li, Y., Song, M., Li, L., Sun, W., Ding, X.
2014: Partitioning of copper between olivine, orthopyroxene, clinopyroxene, spinel, garnet and silicate melts at upper mantle conditions. Geochimica Et Cosmochimica Acta, 125: 1-22.

Palme, H., O'Neill, H.S.C.
2014: Cosmochemical Estimates of Mantle Composition. In: Holland, H.D., Turekian, K.K. (Eds.), Treatise on Geochemistry (Second Edition). Elsevier, pp. 1-39.

Salters, V.J.M., Stracke, A.
2004: Composition of the depleted mantle. Geochemistry, Geophysics, Geosystems, 5(5): n/a-n/a.

Seo, J.H., Guillong, M., Aerts, M., Zajacz, Z., Heinrich, C.A.
2011: Microanalysis of S, Cl, and Br in fluid inclusions by LA-ICP-MS. Chemical Geology, 284(1-2): 35-44.

Sinclair, W.D. (Ed.)
2007: Porphyry Deposits. Mineral Deposits of Canada: A Synthesis of Major Deposit-Types, District Metallogeny, the Evolution of Geological Provinces, and Exploration Methods. Geological Association of Canada, Mineral Deposits Division, Special Publication No. 5, 223-243 pp.

Spencer, E.T., Wilkinson, J.J., Creaser, R.A., Seguel, J.
2015: The Distribution and Timing of Molybdenite Mineralization at the El Teniente Cu-Mo Porphyry Deposit, Chile. Economic Geology, 110: 387-421.

Tassara, A., Echaurren, A.
2012: Anatomy of the Andean subduction zone: three-dimensional density model upgraded and compared against global-scale models. Geophysical Journal International, 189(1): 161-168.

Ulmer, P.
1989: The dependence of the Fe2+-Mg cation-partitioning between olivine and basaltic liquid on pressure, temperature and composition. Contributions to Mineralogy and Petrology, 101: 261-273.

Zajacz, Z., Candela, P.A., Piccoli, P.M.
2017: The partitioning of Cu, Au and Mo between liquid and vapor at magmatic temperatures and its implications for the genesis of magmatic-hydrothermal ore deposits. Geochimica et Cosmochimica Acta, 207: 81-101.

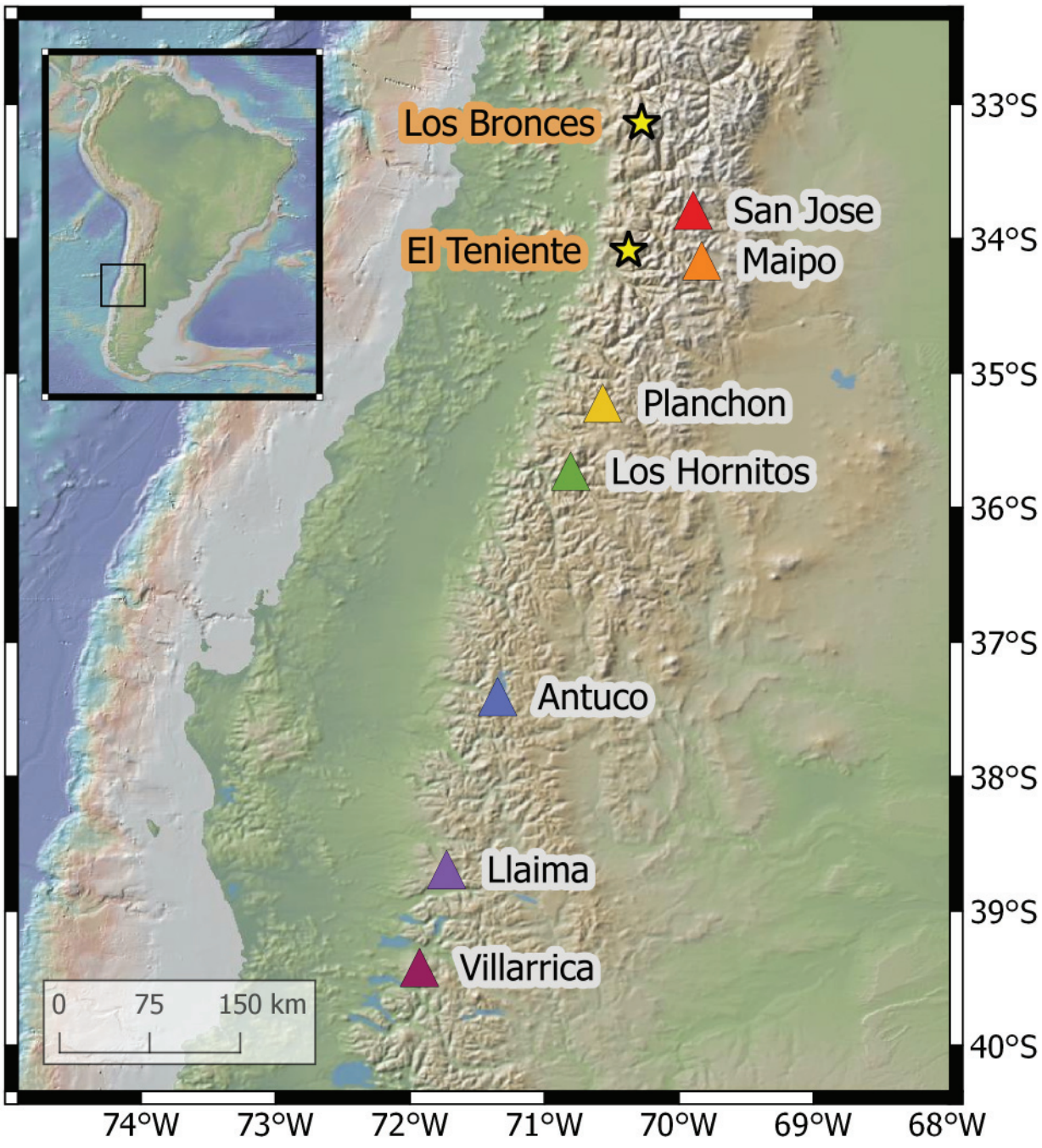

Figure 1. Location map of the sampled SVZ volcanoes. El Teniente and Los Bronces are giant porphyry Cu deposits which formed ca. 5 Ma, prior to the migration of the arc from to the current location defined by San Jose and Maipo.

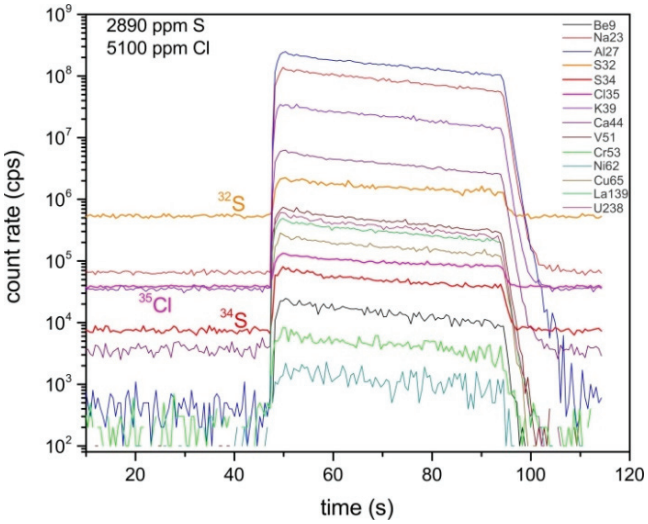

Figure 2. LA-ICP-MS signal obtained on the new in-house-synthetized reference glass.

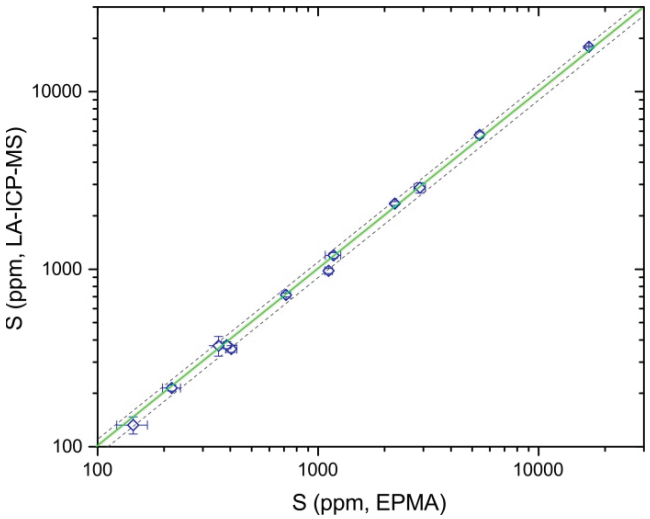

Figure 3. Comparison of S concentrtaions measured in the same silicate glasses by EPMA and LA-ICP-MS.

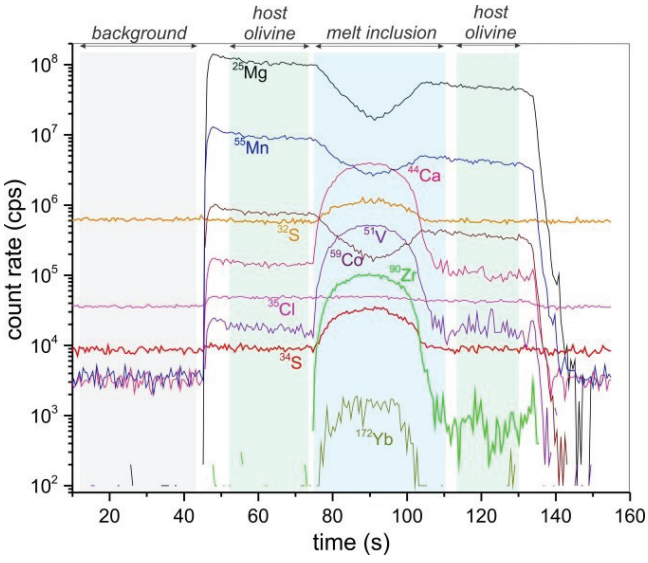

Figure 4. Transient LA-ICP-MS signal obtained during the analysis of a 40 µm-sized olivine-hosted silicate melt inclusion with 2300 ppm S.

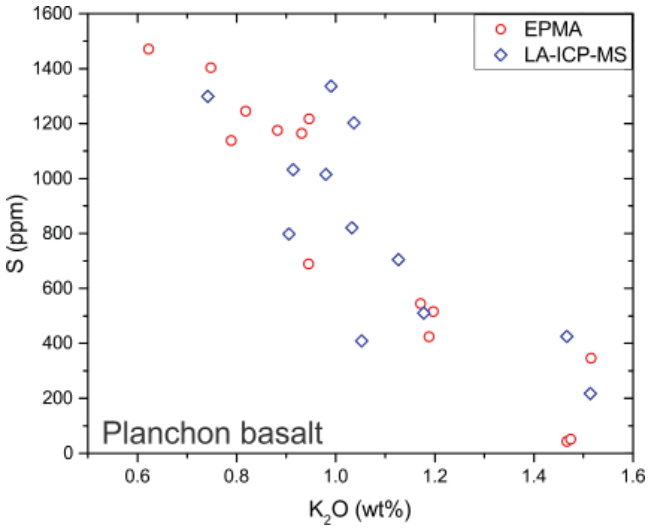

Figure 5. Comparison of S concentrations obtained by EPMA and LA-ICP-MS from olivine-hosted silicate melt inclusions in the same rock samples.

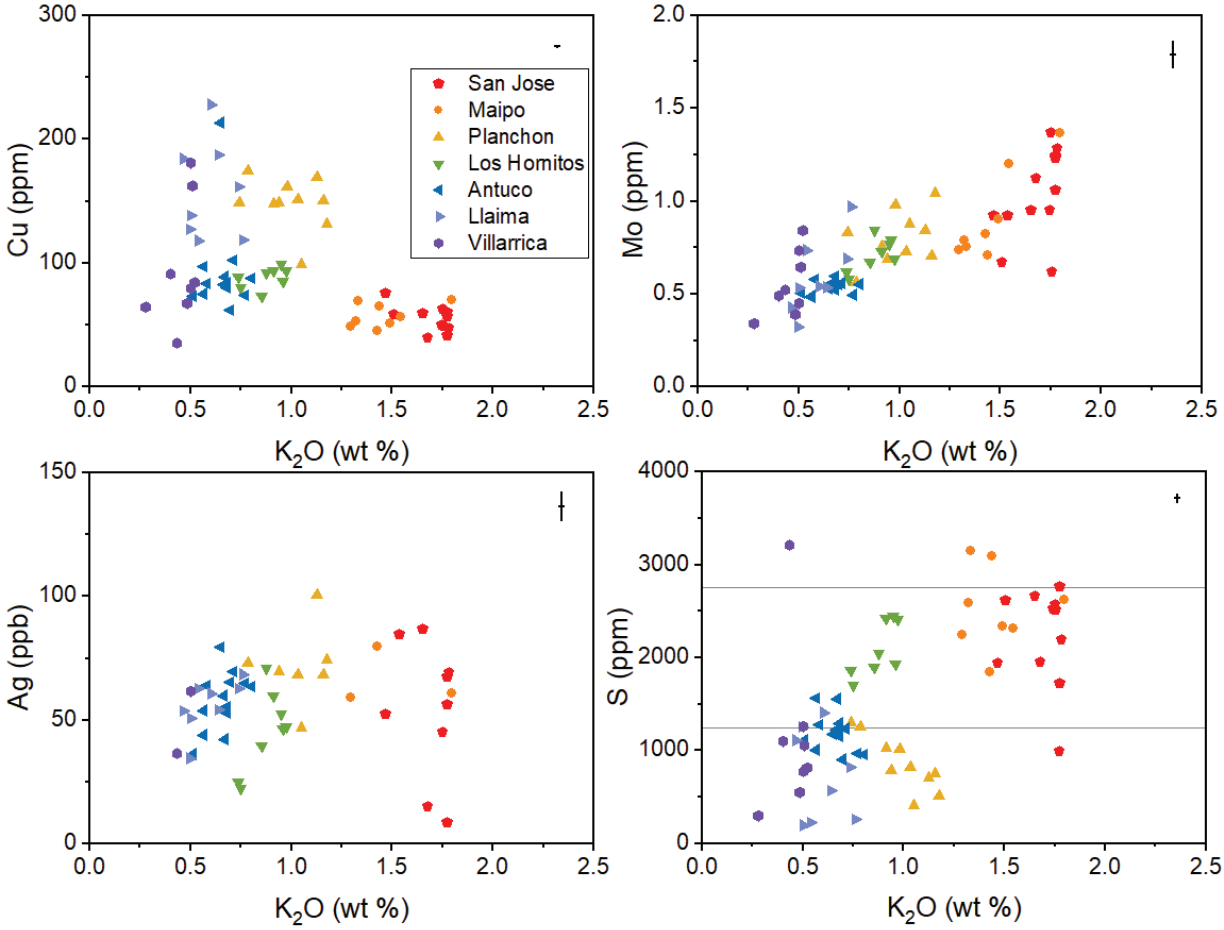

Figure 6. Ore metal concentrations from primitive olivine-hosted SMI plotted against K2O, which serves as an indicator of magma differentiation including crustal contamination. Representative one sigma errors are shown by crosses in the upper right of each plot. Copper concentrations are lower in the north as predicted by global whole rock trends correlated to crustal thickness, but can reach very high concentrations (200 ppm) in the southern volcanoes. Molybdenum is well-correlated with K2O, and this trend is at least partly driven by crustal contamination. Silver shows no discernable trend. Maximum S concentrations are systematically higher in the north (~2700 ppm) than the south (~1250 ppm).

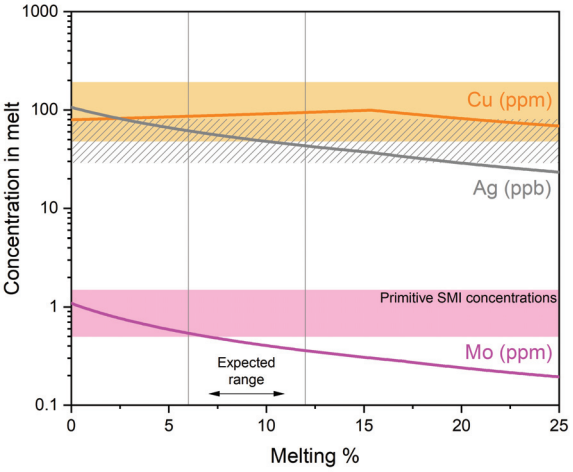

Figure 7. Results of non-modal batch partial melting of the primitive mantle with 0.05 % sulfide, a solid:molten sulfide ratio of 0.85:0.15, and a S solubility of 1300 ppm (Li and Ripley, 2009). Partition coefficients are from (Liu et al., 2014) and (Li and Audetat, 2015). Coloured curves are the modeled concentrations of ore metals in the silicate melt, and shaded fields show the range of concentrations measured in SMI. This model recreates Cu and Ag concentrations reasonably well, but underpredicts the observed Mo concentrations.